Vortex Induced Magnetoresistance Oscillations in Superconducting Nanowires

Benjamin D. G. Steele

University of Leeds

Department of Physics and Astronomy

Submitted in accordance with the
requirements for the degree of

Doctor of Philosophy

August 2019

Intellectual Property Statement

The PGR confirms that the work submitted is his/her/their own, except where work which has formed part of jointly authored publications has been included. The contribution of the PGR and the other authors to this work has been explicitly indicated below. The PGR confirms that appropriate credit has been given within the thesis where reference has been made to the work of others.

This copy has been supplied on the understanding that it is copyright material and that no quotation from the thesis may be published without proper acknowledgement.

The right of Benjamin David George Steele to be identified as Author of this work has been asserted by him in accordance with the Copyright, Designs and Patents Act 1988.

Work from the following jointly authored paper is in sections 2.4.4 and 5.1.2 of this thesis:
S. Atherton, **B. Steele** and S. Sasaki, 'Unexpected Au Alloying in Tailoring In-Doped SnTe Nanostructures with Gold Nanoparticles', *Crystals* **7**, 78(2017) (2015)

- **Work attributed to the candidate**: Performed gold nanoparticle preparation and synthesised samples, SEM imaging, assisting in EDX measurements, analysis of data, and wrote parts of the manuscript.

- **Work attributed to others**: S. Atherton: Performed gold nanoparticle preparation and synthesised samples. S. Sasaki: Conceived the project and performed EDX measurements, integrated difference pieces of the work, and wrote the manuscript. All EDX measurements were performed with guidance from A. Kulak, School of Chemistry, University of Leeds.

Acknowledgements

Firstly, I must thank Dr Satoshi Sasaki and Dr Gavin Burnell for their supervisory roles in this project. I would also like to thank the entire group of Condensed Matter academics for their continuous academic support throughout the project.

My superconductors wouldn't be much use without the great cryogenics team past and present: Luke Bone, Brain Gibbs, John Turton, David Chapman and Adam Foster. Both the Electronics and Mechanical Workshop have played a pivotal role in building and maintaining heaps of equipment, thank you to every one who has been involved in the journey. A special thank you to the late Brain Chesworth, the School of Physics is indebted to your service.

I am deeply grateful for the hard work and support of the Electronic Engineering cleanroom team, in particular Dr Mark Rosamond and Chris Day, who made even managed to make the cleanroom experience enjoyable.

A huge thank you to all who assisted directly with this work. Matthew Vaughan, Gunasheel Krishnaswarmy, Joshua Gretton, and Rory Hynes for assistance with source material synthesis and vapour transport growth characterisation. Connor Wade, Elliot Dransfield, and Sam Atherton for the work on gold nanoparticle catalyst studies. Dr Mannan Ali for continual experimental support and advice. Dr Gavin Burnell, Dr Mark Rosamond and Dr Joseph Batley for advice and assistance with electron beam lithography and device preparation. Finally, thank you to Dr Alexander Kulak for facilitating and performing EDX-SEM.

I would not have made it without the friends and colleagues who helped with everything, from running cryostats to staying sane. I am deeply indebted to Amy Westerman, who taught me as much about PhD survival as of the wonders of low temperature transport techniques. A massive thanks to Georgios Stephanou, Craig Knox and Joshua Gretton for being a great team in and out of the labs. I cannot begin to express my thanks to my mentor, guide, and espresso provider, the master of all things experimental, Dr Mannan Ali. My office mates Fatma Al'Ma Mari, Katharina Zeissler, Satam Alotibi and Emily Darwin, who all became good friends. Also, a huge thank you goes out to Jamie Massey, Kathryn Moran, Jack Adams, Rowan Temple, Philippa Shepley, Risalat Khan, Nicolas Peters, Sophie Morley, David Bacon, Matthew Rodgers, Kowsar Shahbazi, James Bucag, Rebecca Whittingham, Sam Atherton, Matthew Vaughan, Alistair Walton, Daniel Grout, Gregory Simon, and I am sure many more! Each one of you has at some point changed my PhD life for the better.

To my family, Sue, Dave, Katie, Jessica, Margaret, Barrie, Beverley and all the rest. There isn't a big enough thank you for the support and love they have given me. They have been a continuous source of strength to help me carry on.

Most importantly, I would like to thank my best friend, Ms (future Dr) Elinor Cosgrave. Together we have loved, supported, and near enough killed each other this past few years. Thank you for being the best you when I needed you to be. You are my everything.

And last but by no means least, Otto von Stockport Cosgrave-Steele, the fabulous rabbit. To whom draft copies of this thesis have made sub-optimal bedding.

Abstract

This thesis details work investigating the oscillatory magnetoresistance (OMR) effect observed in superconducting nanowires. The OMR effect is a repeated rise and fall of resistance, in the otherwise monotonic magnetic field induced superconducting transition. Two material systems are studied: Nb nanowires, grown by DC sputter deposition, are used as a typical, commonly used superconductor; In-SnTe nanowires, synthesised by vapour transport growth, are used as a candidate topological superconductor. In-SnTe nanowires were grown without Au nanoparticles as a catalyst because, unexpectedly, the Au was observed to contaminate the crystal growth. The topological surface states are investigated through the observation of weak anti-localisation. Fitting to a 2D weak anti-localisation effect yields a maximum of four surface conductance channels, which is expected for this topological crystalline insulator.

This thesis find that oscillatory magnetoresistance is a misnomer, the resistance modulation is not in the form of an oscillatory function. The OMR effect observed is closely described by a set of Gaussian distributions, centred at a series of magnetic fields. Several methods are used to probe the OMR effect, such as: alternating current, constant direct current and pulsed current-voltage. The relationship between the OMR effect is tested with relation to the temperature, applied current amplitude, frequency of the alternating current and the orientation of the applied magnetic field. Of the presently known candidates to describe an OMR effect, the most likely candidate is found to be periodic vortex motion. Vortex motion dissipates energy, causing a finite resistance. In this model, rates of vortex travel are modulated periodically with respect to an applied magnetic field. There are two main factors that contribute: the rearrangement of the vortex lattice at regular intervals in magnetic field; and the modulation of vortex entry and exit energy barriers. These two mechanisms combine to regularly inhibit vortex motion, reducing the resistance, and allow vortex motion, increasing the resistance. Pinning is found to dominate the characteristics of the OMR effect. This effect is more apparent in comparisons between the two types of nanowire grown. The mechanism behind the OMR effect appears to be due to the probabilistic motion of vortices. These motion events can be assisted by thermal energy or current flow. A new MHz frequency cut off in the OMR is observed, which can be attributed to the vortex dynamics.

CONTENTS

Abbreviations

AC   Alternating Current

ARPES   Angle Resolved Photoemission Spectroscopy

BCS   Bardeen, Cooper and Schrieffer

DC   Direct Current

EBL   Electron Beam Lithography

EDX   Electron Dispersive X-ray Microscopy

G-L   Ginzburg-Landau

GNP   Au Nanoparticle

HLN   Hikami-Larkin-Nagaoka

IV   Current-Voltage

JJ   Josephson Junction

LOR   Lift-Off Resist

MMA   Methyl Methacrylate

MR   Magnetoresistance

OMR   Oscillatory Magnetoresistance

PMMA   Polymethyl Methacrylate

SEM   Scanning Electron Microscopy

SQUID Superconducting Quantum Interference Device

TCI   Topological Crystalline Insulator

TI   Topological Insulator

TS   Topological Superconductor

VTG   Vapour Transport Growth

VTI   Variable Temperature Insert

WAL   Weak Anti-localisation

WL   Weak Localisation

CONTENTS

CHAPTER 1

Introduction

1. INTRODUCTION

In 1911, a transition to a zero resistance state in elementary superconductors was discovered by Onnes [1]. This discovery was made possible by advancements in the liquefaction of Helium, allowing measurements to be made in the temperature range of a few Kelvin above absolute zero. Further to this fascinating discovery, in 1933 the new state was observed to exhibit perfect diamagnetism by Meissner and Ochsenfeld [2]. Perfect diamagnetism is the complete expulsion of flux from the superconductor, regardless of the prior state. This is the property that distinguishes the superconducting state from a perfect conductor, which simply has zero resistance.

Several theories to describe the behaviour of the superconducting state were based on the phenomena observed, such as the zero resistance and the Meissner effect. The success of these theories first described by the London brothers, Pippard, and Ginzburg and Landau, comes from the ability to apply them to realistic situations in macroscopic systems. The microscopic theory of Bardeen, Cooper and Schrieffer (BCS) describes the fundamental interactions of electrons that result in the superconducting state. This microscopic theory can be used to provide justification for the use of the phenomenological theories, tying the two approaches together.

Many revolutionary technologies utilise the properties of superconductors: from large superconducting solenoids in magnetic resonance imaging machines, to levitating, frictionless train tracks. The development of nanoscale production techniques, such as lithography has allowed inventions to be reduced in size, making use of the quantum properties of superconductivity. Common examples being quantum bits and quantum interference magnetic flux sensors.

In order to make use of superconducting materials on the nanoscale, the properties must be understood to a degree where characteristics can be controlled. Superconducting vortices attract a large amount of research attention due to the relevance in technological applications. The understanding and control of vortex dynamics is key to a range of technologies. Superconducting solenoids, for instance, must be free of vortex motion in order to have a completely dissipationless loop.

Topological materials are a relatively young area of physics research. Topological superconductors are a small facet of this complex and varied field. They are postulated to be able to host exotic quasi-particles in the form of Majorana fermions, which, among other things, are their own antiparticle. Working towards the detection and manipulation of these exotic particles has been the focus of many works to date. The main focal points being material development and the attempts to observe signatures of topological superconductivity.

It is the aim of this work to characterise the oscillatory magnetoresistance (OMR) effect, which is observed in the magnetic field transition of nanoscale superconductors. Previous observations of OMR are varied and the origin is not well understood. Explanations span from quantum interference to a Coulomb blockade arrangement. This thesis discusses the likely origins of OMR, with a detailed discussion of the periodic motion of vortices, controlled by edge barriers and primarily modulated by an applied magnetic field.

Before commencing with the observations and discussions, the theories and concepts required to understand them are provided in Chapters 2. A brief overview of the superconducting theories is covered and then focussed towards vortex properties and vortex motion. This leads to a detailed description of the periodic motion of vortices that this study finds to be the most likely candidate for the OMR observed. A toy model description is

presented to help simplify the system and provide a straightforward method to generate periodic barriers to vortex motion.

Nb nanowires, grown by DC sputter deposition, are utilised as a standard superconducting nanowire in which to study the OMR effect. These nanowires were used as a controllable growth method using a standard elemental superconductor. Nb is an effective material in which to study the OMR effect, with few unknown parameters and the support of a wide literature base. Comparison is drawn with comparable experiments and theories. The results are presented in Chapter 4.

Chapter 5 discusses a range of observations for candidate topological superconductor In doped SnTe. The base material, SnTe is a topological crystalline insulator. By doping SnTe with In, the carrier density increases and the superconducting critical temperature rises dramatically into a range measurable using a Helium gas flow cryostat. While the material is not yet fully accepted as a topological superconductor, superconducting topological materials are strong candidates. Evidence for topological superconductivity has been demonstrated previously for In-SnTe, as reviewed in section 2.4.3.

Superconducting In-SnTe does not have a broad experimental foundation. As a result, in this thesis there is a strong focus on the fabrication and basic characterisation. It is accepted in the literature that to grow nanowires of this material, one should employ vapour transport growth with Au nanoparticles as a catalyst. For the growth arrangement used in this thesis the use of a catalysts did not result in a high yield of nanowires, and instead contaminated the growth. These findings have been published in the *Crystals* journal [3], by S. Atherton, the author of this thesis, and S. Sasaki. Avoiding potential contamination, this thesis presents for the first time In-SnTe nanowires grown by vapour transport growth without a catalyst. Several of these nanowires have a thickness of approximately 100 nm. Electrical contacts are made to these samples using an angled thermal evaporation procedure, which overcomes a self shadowing effect observed due to the sharp features of the crystal.

In addition to showing superconducting properties, the In-SnTe nanowires also exhibited an OMR effect. This has allowed further analysis of the mechanism that generates the effect. The differences between these samples and the Nb nanowire allows a greater understand of the OMR effect in general. These differences include the sample dimensions, pinning landscape and penetration depth. The character of the OMR effect exhibited in In-SnTe nanowires is discussed with relation to these differences.

A weak anti-localisation effect is observed in the nanowires, providing evidence that the topological surface states are not destroyed by the high In doping. This provides scope to explore topological superconductivity in In-SnTe nanowires.

1. INTRODUCTION

CHAPTER 2

Background Theory

This chapter introduces the theories and phenomena that are required to understand the work presented in the following chapters. Phenomenological models for superconductivity are discussed in detail, as these yield the most powerful descriptions of superconductivity in practical situations. An overview of the techniques used to describe vortices in superconductors is given followed by a discussion of previous approaches to describe vortex entry and exit barriers. A toy model is discussed which unpacks the basics of a vortex induced OMR and allows for some tentative predictions. Previous observations of OMR and the interference effects used to describe them are outlined, many of which are inappropriate descriptions for the systems studied. Finally, topological materials and Majorana fermions are discussed with relation to potential nanoscale devices and technologies.

2.1 Phenomenological Theories of Superconductivity

The following examinations of the formulations used to describe superconductivity were constructed with use of the text books by Annett and Tinkham [4, 5]. For further information on superconductivity fundamentals the reader is advised to access these resources. While the microscopic theory by Bardeen, Cooper and Schrieffer (BCS) provides a complete description from fundamental arguments, the most practical and useful description of superconductivity comes from phenomenological descriptions, where many of the definitions of superconducting parameters can be derived.

2.1.1 The London Theory

The London brothers theory is based on a two fluid model, like that used to describe superfluid ^4He. A fraction of the normal state conduction electrons act as a superfluid while the rest remain normal, this fraction is 0 at $T = T_c$ and $\sim \frac{1}{2}$ for $T << T_c$. The superfluid electrons provide the required zero resistivity shorting out any resistivity from the population of remaining normal electrons. While the model is simple, it provides some insight and predicts some of the observed behaviours, including the penetration of external flux over one of the characteristic lengths, the penetration depth.

The London brothers put forward two equations that govern the electrodynamics of superconducting charge carriers in the presence of local electric and magnetic fields, these are:

$$\mathbf{E} = \frac{\partial}{\partial t} \Lambda \mathbf{J_s} \tag{2.1}$$

$$\mathbf{h} = -\nabla \times (\Lambda \mathbf{J_s}), \tag{2.2}$$

with the definition of a phenomenological parameter Λ:

$$\Lambda = \frac{m}{n_s e^2}, \tag{2.3}$$

where $\mathbf{J_s}$ is the current flux of the superconducting electrons, m is the electron mass, e is the electron charge, and n_s is the number density of superconducting electrons. The first equation encompasses a continuous acceleration of the superfluid electrons, which results in perfect

conductivity. The second equation, when combined with the Maxwell equation $\nabla \times \mathbf{h} = \mathbf{J}$, results in the exponential screening of magnetic fields by solving:

$$\nabla^2 \mathbf{h} = \frac{\mathbf{h}}{\lambda^2},$$

(2.4)

where the characteristic length scale λ is the penetration depth of a magnetic field inside a superconductor, given at $T = 0$ by:

$$\lambda^2(0) = \frac{m}{\mu_0 n_s e^2}.$$

(2.5)

2.1.2 Pippard Non-local Electrodynamics

While the London theory went some way to describing the penetration depth of superconductors, in 1953 Pippard formulated an extension to the theory that accounts for the experimentally observed values of λ. These are larger than those calculated and have an increase in λ with impurity concentration [6]. The formulation includes a variation of the current at a point, $\mathbf{r}$, which depends on the electric field, $\mathbf{E}(\mathbf{r})$, over a volume. This volume of influence was assumed to have a radius of a new parameter, the coherence length, ξ_0. This radius can be estimated using the uncertainty principle. If the electrons that can fluctuate is restricted to those within $k_B T_c$ of the Fermi surface, the uncertainty in momentum becomes $\Delta p = k_B T_c / v_F$. Taking ξ_0 to be proportional to the uncertainty in space gives:

$$\xi_0 = a\Delta x = a\frac{\hbar v_F}{k_B T_c},$$

(2.6)

where a is a constant which is found experimentally to be 0.15 and in BCS theory is calculated as 0.18. Pippard demonstrated that the experimental data fitted well to this adjusted theory and provides justification for the use of a superconducting coherence length. The coherence length can be extended to include scattering using the normal state mean free path, l, as:

$$\frac{1}{\xi} = \frac{1}{\xi_0} + \frac{1}{l}.$$

(2.7)

The result of this is that for clean superconductors, with large l, the superconductor has $\xi = \xi_0$, while for dirty superconductors ξ is suppressed. This suppression agrees with the experimental evidence. Pippard's result is works well at T = 0 K although the relation can be used in approximation at finite temperatures.

2.1.3 The Ginzburg-Landau Theory

The 1950 Ginzburg-Landau (G-L) theory [7] is an extension of the Landau theory for second order phase transitions with a complex order parameter, $\Psi(r)$, named the G-L order parameter, where $|\Psi|^2$ is essentially the local density of superconducting electrons from the London equations. While this is a classical approach to a system more completely described by the BCS theory, G-L models can be more powerful when spatial fluctuations in the order parameter should be included. Furthermore, Gor'kov [8] demonstrated that $\Psi(r)$ is directly proportional to the BCS order parameter, Δ, and showed that the G-L theory is actually a

limiting case of BCS theory. After this proof, it became accepted as a crucial tool in understanding the macroscopic phenomena exhibited by the quantum state of superconductors.

If Ψ is small and varies slowly in space, the G-L free energy functional for the superconducting state is postulated as a series expansion which takes the form:

$$G_s = G_N + \alpha|\Psi|^2 + \frac{\beta}{2}|\Psi|^4 + \frac{1}{2m^*}|(-i\hbar\nabla - 2e^*\mathbf{A})\Psi|^2 + \frac{|\mathbf{h_m}|^2}{2\mu_0}, \tag{2.8}$$

where G_N is the Ginzburg-Landau free energy of the normal state, α and β are unknown parameters, m^* and e^* are the superconducting carrier mass and charge respectively, and $\mathbf{h}$ is the local magnetic field. The first term encompasses the free energy of the normal state, the next two terms give the free energy for a homogeneous superconducting state without fields. The penultimate term encompasses inhomogeneity and magnetic fields through the kinetic energy associated with changes in the pair potential. This term makes use of the quantum mechanical operator $(-i\hbar\nabla - q\mathbf{A})$, where $\mathbf{A}$ is the magnetic vector potential. The final term is the magnetic self-energy of the superconducting state.

In the case of a homogeneous superconductor with no external fields, the difference in energy of the superconducting and normal states becomes:

$$\Delta G = \alpha|\Psi|^2 + \frac{\beta}{2}|\Psi|^4, \tag{2.9}$$

which is a two term series expansion in $n_s = |\Psi^2|$. Retaining the first two terms in the expansion is valid for small perturbations, $T \sim T_c$. β must be positive in order to have constrained solutions, however α may take both positive and negative values. The sign of alpha defines whether the minimum has a non-zero value of $|\Psi|^2$. When $\alpha < 0$, the minimum occurs at $|\Psi|^2 = -\alpha/\beta$. From this the simplest approximation for the temperature dependence is $\alpha(T) = \alpha_0(T - T_c)$, giving non-zero solutions to ΔG for $T < T_c$ only. This is illustrated in Fig. 2.1 (a).

In order to deal with spatial changes, the order parameter is now taken in the more general form $\Psi(\mathbf{r}) = |\Psi(\mathbf{r})|e^{i\phi(\mathbf{r})}$. By including the terms that encompass inhomogeneity and external fields, and minimising ΔG w.r.t. Ψ and $\mathbf{A}$, one arrives at the two G-L differential equations:

$$\alpha\Psi + \beta|\Psi|^2|\Psi| + \frac{1}{2m^*}(-i\hbar\nabla - e^*\mathbf{A})^2\Psi = 0 \tag{2.10}$$

$$\mathbf{J_s} = -\frac{ie^*\hbar}{2m^*}(\Psi^*\nabla\Psi - \Psi\nabla\Psi^*) - \frac{e^{*2}}{m^*}|\Psi|^2\mathbf{A}. \tag{2.11}$$

The spatial distribution of the supercurrent and order parameter can be determined from these equations. Two important results from the G-L differential equations are the G-L coherence length and penetration depth, ξ_{GL} and λ_{GL}. Similarly to the Pippard coherence length, ξ_{GL} is defined as the typical length scale over which modulations in the order parameter are possible. Minimising the first G-L equation 2.10, at a normal metal-superconductor interface, in the absence of fields, and restricting to one dimension results in the differential equation:

$$\frac{\hbar^2}{2m^*}\frac{d^2\Psi}{dx^2} = (\alpha(T) + \beta|\Psi|^2)\Psi. \tag{2.12}$$
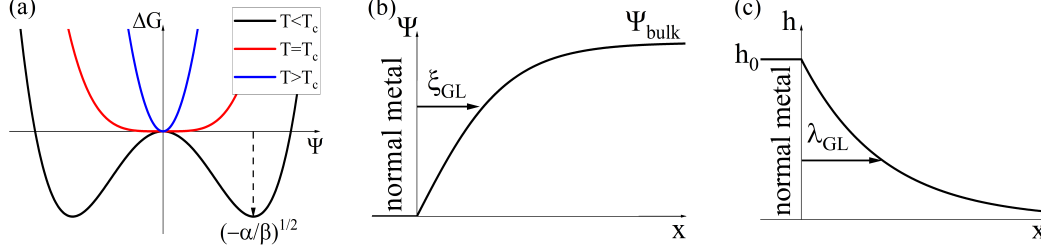
Figure 2.1: (a) The free energy, ΔG as a function of the G-L order parameter. For $T < T_c$ minima are observed at non-zero Ψ. (b) Spatial evolution of the G-L order parameter at a normal metal-superconductor interface. (c) Decay of the magnetic field at a normal metal-superconductor interface over the G-L penetration depth.

The solution to this equation, as illustrated in Fig. 2.1(b), must contain an exponential change from 0 to the bulk order parameter with the characteristic length:

$$\xi_{GL} = \sqrt{\frac{\hbar^2}{2m^* \alpha(T)}}. \tag{2.13}$$

The temperature dependence of the G-L coherence length is given as:

$$\xi_{GL}(T) = \xi_{GL}\left(1 - \frac{T}{T_c}\right)^{-1/2} \tag{2.14}$$

which matches the experimental observation that in pure elemental superconductors, when $T \ll T_c$, $\xi(T) = \xi_{GL}$.

The G-L penetration depth, which is also the decay length of magnetic fields into the superconductor, can be found by considering the second G-L equation 2.11 without gradients in Ψ:

$$\nabla \times \mathbf{J_s} = -\frac{e^{*2}}{m^*}|\Psi|^2 \nabla \times \mathbf{A}, \tag{2.15}$$

which can be rewritten using $\nabla \times \mathbf{h} = \mu_0 \mathbf{J}$,

$$\nabla \times \nabla \times \mathbf{h} = -\frac{1}{\lambda_{GL}^2}\mathbf{h}. \tag{2.16}$$

This is solved by an exponential decay, as illustrated in 2.1(c), over the scale of the G-L penetration depth, which is defined in the same way as the London penetration depth. The temperature dependence of λ_{GL} follows $(1 - \frac{T}{T_c})^{-1/2}$, and so we can define a dimensionless, temperature independent, constant parameter:

$$\kappa = \frac{\lambda(T)}{\xi(T)}. \tag{2.17}$$

κ is a key characteristic that defines the behaviour of the superconductor when exposed to external magnetic fields.

2.1.4 BCS Theory

While the G-L theory is incredibly powerful for describing realistic superconductor samples, in 1957 Bardeen, Cooper and Schrieffer [9, 10] proposed a fundamental mechanism to explain to origins of the superconducting state. Due to the unfortunate political climate during this period of history the G-L model and BCS theory were developed without collaboration across the cold war divide.

In the BCS theory, the transition to superconductivity occurs due to a phonon mediated electron-electron interaction which overcomes Coulomb repulsion and forms electron pairs, called Cooper pairs. The formation of Cooper pairs is critical to describing the superconducting state by a coherent wavefunction, which is also assumed to some degree in the macroscopic theories. From this point forward, the superconducting carriers will be taken as Cooper pairs with a mass and charge twice that of a single electron.

Evidence for a phonon mediated pairing mechanism is provided by measurements of the isotope effect, where the atomic mass of the superconductor is correlated to its critical temperature [11, 12]. The phonon that mediates the attraction results from an electron perturbing the crystal lattice, which immediately interacts with another electron to reduce its energy, this process repeats continuously bringing the system into a lower energy state. By considering the population of phonons in the system, we can approximate the interaction to find the energy of the paired states. The maximum energy of the phonons is the Debye energy, $\hbar\omega_D$, and thus the electron pairing energy, $\hbar\omega_c$, can be expected to be approximately the same. Cooper approximated the interaction potential to a constant, $V_{kk'} = -V$, for states within $\hbar\omega_c$ of the Fermi energy, E_F, and zero, $V_{kk'} = 0$, for all other states. For small potentials, such that $N(0)V \ll 1$, where $N(0)$ is the density of states at the Fermi energy, the solution can be written as:

$$E \approx 2E_F - 2\hbar\omega_c e^{-2/N(0)V}, \qquad (2.18)$$

where the factor 2 is from the fact that 2 electrons are paired.

This shows that the bound state has a lower energy than the Fermi energy, with a greater kinetic energy. The introduced attractive potential reduces the total energy by a greater amount than the kinetic energy increase, giving a superconducting ground state energy.

The simplest and most common instance of Cooper pair formation is between electrons with opposite momentum vectors and anti-parallel spin states. The wavefunction of the two electrons must be antisymmetric, as they are Fermions. To satisfy this the combination of the spatial spin part of the wavefunction must result in an antisymmetric wavefunction. In some exotic cases a frequency part of the wavefunction is also included, although that discussion is not necessary here. The simplest spatial wavefunction for an attractive potential is spatially symmetric, which is satisfied by an s-wave state. This symmetry requires an antisymmetric spin singlet. The total spin of each pair is an integer number of spins, and so the paired Fermionic particles follow Boson-like statistics. Cooper pairs are all at the same low energy level in the superconducting condensate. This correlated many-particle quantum ground state can be described by a macroscopic wavefunction.

The typical energy scale relevant to superconductivity comes from BCS theory in the form of the band gap energy, Δ. This energy scale determines many of the properties of superconductors as it is the energy required to add an electron or hole to the BCS ground

state. For the many superconductors that follow BCS theory the band gap is directly proportional to the superconducting critical temperature. The gap appears as Cooper pairs are formed out of electron states within the range $E_F \pm \Delta$. Although it would appear that half of these energies are in fact higher than E_F, it is the nature of the Bosonic condensate that causes all the states have the same lower energy. As with all systems described by an energy gap, for a high enough driving frequency the linear response no longer applies. When the driving frequency nears $\hbar \omega_c = 2\Delta$ the normal state conduction electrons begin to dominate the transport, resulting in a finite resistance, even at $T \ll T_C$.

2.2 Magnetic Vortices in Superconductors

2.2.1 Type I and Type II superconductivity

The distinguishing factor between Type I and Type II superconductivity is the surface energy associated with penetrating flux and is the difference between the diamagnetic energy from the magnetic field and the condensation energy of the superconducting state. In the construct of the G-L model, κ conveniently contains all of the information required to separate the two types, as it is the ratio between the flux penetration and superconducting coherence lengths. For type I, when $\kappa < 1/\sqrt{2}$, the boundary surface energy is positive, the domains of normal and superconducting material separate to form large domains. For type II, when $\kappa > 1/\sqrt{2}$, the boundary surface energy is negative and results in a maximisation of the boundary surface area by separating the flux into as small sections as possible, the smallest division being the flux quantum: $\Phi_0 = h/2e$. Superconducting flux quanta penetrations are called vortices as they have an associated screening current, which wraps around a central flux core, separating the normal and superconducting regions.

The flux free Meissner state can only persist up to a certain value of field. For bulk Type I superconductors, there is a first order transition to the normal state at the thermodynamic critical field:

$$\mu_0 H_c = \frac{\Phi_0}{2\pi\sqrt{2}\xi\lambda}.$$

(2.19)

For bulk Type II superconductors, vortices can stabilise at much smaller fields than H_c. The energy associated with the first vortices entering depends upon the ratio κ. This ratio dictates when vortices begin to stabilise at the lower critical field, given by:

$$H_{c1} = \frac{H_c}{\sqrt{2}\kappa} \ln(\kappa) = \frac{\Phi_0}{4\pi\lambda^2} \ln(\kappa).$$

(2.20)

As H is increased beyond H_{c1} vortices increase in density, destroying the superconducting condensate until some upper critical field, H_{c2}, where the superconducting volume smoothly goes to zero. H_{c2} is calculated by finding the field required to cover the superconductor in vortices, at which point the entire volume will be normal. The surface area over which the vortex flux penetrates is $2\pi\xi^2$, therefore the upper critical field is expressed as:

$$\mu_0 H_{c2} = \frac{\Phi_0}{2\pi\xi^2}.$$

(2.21)

11

2.2.2 Flux Quantisation in Type II Superconductors

The quantisation of magnetic flux into isolated vortices can be derived by considering the second G-L equation 2.11, taking $\mathbf{J_s}$ as the current around a loop and $\mathbf{A}$ as the magnetic vector potential for the field through it:

$$\mathbf{J_s} = \frac{e\hbar}{m}|\Psi|^2\nabla\phi - \frac{2e^2}{m}|\Psi|^2\mathbf{A}, \tag{2.22}$$

where the $\nabla\phi$ term results from $\nabla\Psi = i(\nabla\phi)\Psi$. Integrating over the whole loop gives:

$$\oint \mathbf{J_s}.\mathbf{dl} = \frac{e|\Psi|^2}{m} \oint \left(\hbar\nabla\phi - 2e\mathbf{A}\right).\mathbf{dl}. \tag{2.23}$$

The flux can be identified using Stokes theorem $\oint \mathbf{A}.\mathbf{dl} = \int \nabla \times \mathbf{A}.\mathbf{dS} = \int \mathbf{h}.\mathbf{dS} = \Phi$. This leads to:

$$\frac{m}{e|\Psi|^2} \oint \mathbf{J_s}.\mathbf{dl} + 2e\Phi = \oint \hbar\nabla\phi.\mathbf{dl}. \tag{2.24}$$

$\mathbf{J_s}$ is zero deep in the superconductor. Taking the loop integral far away from the magnetic flux, the first term in Eq. 2.24 becomes zero. The order parameter is single valued, therefore the phase must change by integer multiples of 2π. This results in the flux:

$$\Phi = \frac{2\pi n\hbar}{2e} = n\Phi_0, \tag{2.25}$$

with the definition of the flux quantum, $\Phi_0 = h/2e$.

2.2.3 The Magnetic Profile of an Isolated Vortex

Minimisation of the surface energy requires that the normal core of a magnetic vortex has a radius of the order of ξ, where the order parameter is zero. Accordingly the penetrating field is maximum at the centre and decays away over the scale of λ due to screening currents as illustrated in the vortex cross section Fig. 2.2. For $H_{c1} < H \ll H_{c2}$, the vortex density is low enough that there is negligible overlap in the magnetic profiles, and so vortices can be treated as independent objects. In the high κ limit, which will be the case in all of the experimental chapters, Ψ may be treated as approximately constant, except for in the core radius ξ. Due to this simplification, the London equations can be applied far from the vortex core. When including a single flux quantum, located at position r and aligned to the z axis, the second London equation 2.2 becomes:

$$\nabla \times (\lambda^2\mathbf{J_s}) + \mathbf{h} = \hat{\mathbf{z}}\Psi_0\delta(\mathbf{r}). \tag{2.26}$$

Once again using the Maxwell equation $\nabla \times \mathbf{h} = \mathbf{J}$ we arrive at the partial differential equation:

$$\lambda^2\nabla^2\mathbf{h} + \mathbf{h} = \hat{\mathbf{z}}\Psi_0\delta(\mathbf{r}). \tag{2.27}$$

The exact solution to this equation makes use of the zero-order Bessel function, K_0:
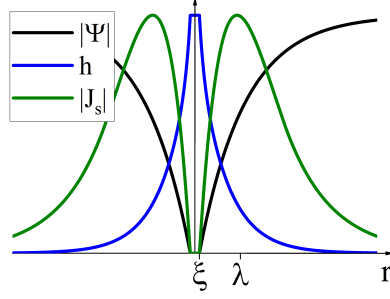
Figure 2.2: A normalised and idealised vortex core profile showing: the magnitude of the wavefunction, $|\Psi|$, the field penetration, h, and the absolute value of the current, $|J_s|$. The wavefunction is depleted in the centre and exponentially increases to the bulk value. The field is constant at the core and decays to zero in the bulk. The screening current has a maximum at some radius near the core. The current circulates around the core, the sign of the current is opposite on either side of the vortex.

$$\mu_0 h(r) = \frac{\Phi_0}{2\pi\lambda^2} K_0\left(\frac{r}{\lambda}\right),\tag{2.28}$$

where for large values of r, $K_0(r/\lambda) \sim e^{-r/\lambda}$ and for small values of r, $K_0(r/\lambda) \sim \ln(\lambda/r)$. In reality, the central vortex core has a relatively constant magnetic field. The vortex circulating current can be found from, $dh(r)/dr$ which results in the first order Bessel function, K_1, which can also be easily understood in two limiting scenarios. For small r, $J_s \sim \frac{\Phi_0}{2\pi\mu_0\lambda^2}\frac{1}{r}$, while for large r, $J_s \sim \frac{\Phi_0}{2\pi\mu_0\lambda^2}e^{-r/\lambda}$. The resulting picture is illustrated in Fig. 2.2.

An approximation to the vortex core energy can be made by considering the kinetic energy per unit volume, $e_k = \frac{1}{2}mv^2 n_s$ with an effective supercurrent velocity defined by $\mathbf{J_s} = -en_s\mathbf{v}$. The energy per unit length is of the order of:

$$\epsilon_l = \left(\frac{\Phi_0^2}{4\pi\mu_0\lambda^2}\right)\ln\left(\frac{\lambda}{\xi}\right).\tag{2.29}$$

2.2.4 Inter-vortex forces

Still considering the case of high κ, the energy and forces associated with two vortices can be estimated by taking a superposition of the field of two vortices, at positions $\mathbf{r_1}$ and $\mathbf{r_2}$:

$$\mathbf{h}(\mathbf{r}) = \mathbf{h_1}(\mathbf{r}) + \mathbf{h_2}(\mathbf{r}) = [h(|\mathbf{r}-\mathbf{r_1}|) + h(|\mathbf{r}-\mathbf{r_2}|)]\hat{\mathbf{z}},\tag{2.30}$$

where $h(|\mathbf{r}-\mathbf{r_i}|)$ is the vortex magnetic profile from Eq. 2.28. Following the formulation of Tinkham [5], the energy of the interacting vortices becomes:

$$E = \left(\frac{\Phi_0}{2\mu_0}\right)[h_1(\mathbf{r_1}) + h_1(\mathbf{r_2}) + h_2(\mathbf{r_1}) + h_2(\mathbf{r_2})]\tag{2.31}$$

$$= \left(\frac{\Phi_0}{\mu_0}\right)h_1(\mathbf{r_1}) + \left(\frac{\Phi_0}{\mu_0}\right)h_1(\mathbf{r_2}),\tag{2.32}$$

by symmetry. The first term is the energy of the two separate vortices, and the second term is the interaction energy. Using the known field distribution we come to the inter-vortex energy:

$$E_i = \left(\frac{\Phi_0^2}{2\pi\mu_0\lambda^2}\right) K_0\left(\frac{r_{12}}{\lambda}\right), \tag{2.33}$$

where r_{12} is the vortex separation.

The energy between two vortices with the same flux direction (i.e. not anti-vortices) is always positive and repulsive. The force between the two vortices is the derivative of E_i w.r.t. space, which simplifies to:

$$\mathbf{f_{2v}} = \mathbf{J_s(r_2)} \times (\hat{\mathbf{z}}\Phi_0), \tag{2.34}$$

and can be generalised to the force on a single vortex due to many vortices as:

$$\mathbf{f} = \mathbf{J_s} \times (\hat{\mathbf{z}}\Phi_0), \tag{2.35}$$

where now $\mathbf{J_s}$ is equal to the sum of the supercurrent due to all other vortices at the location of the vortex in question. This tells us the driving force on vortices is a Lorentz force. While the influence of vortices is reasonably short range, the implication is that an unresolved supercurrent will cause an acceleration of the vortex, increasing the kinetic energy. To obtain a steady state, a regular vortex lattice is required that balances the forces on each vortex. This is best accomplished by a triangular lattice. However, even if the vortices manage to find a perfect stable equilibrium, the addition of a transport current immediately causes vortex motion, unless there are additional forces, as will be discussed later. Vortex motion dissipates energy as it requires material to switch to and from the normal state as each vortex progresses. This dissipation of energy results in resistance to current, unless there is a section of superconductor that is capable of short circuiting the resistive section. In the absence of resistive forces to vortex motion, superconductors could only be most useful when fields are below H_{c1}. For most materials used in application vortices penetrate at very small fields and so pinning is necessary to achieve stable superconductivity.

Using a perfectly triangular lattice as a model system, the nearest neighbour distance of a typical vortex lattice can be estimated as:

$$a_\triangle = \frac{2}{\sqrt{3}} \frac{\Phi_0}{\mu_0 H}, \tag{2.36}$$

this shows that the effective radius of the vortex lattice will decrease as the vortex and flux density increases.

2.2.5 Vortices in Thin Films

When the dimensions of the superconducting sample are comparable to the characteristic length scales ξ and λ, the spatial limitations have a profound effect. When λ is greater than one or more of the sample dimensions, the current J_s can no longer be said to be zero throughout the material. This has consequences for the quantisation of the vortices as the line integral over J_s in Eq. 2.24 can no longer be removed. This has the effect of adding an unknown amount to the flux quantum, such that the effective flux quantisation is $\Phi_{eff} \gtrsim \Phi_0$. Despite this fact, very

thin superconductors do exhibit zero electrical resistivity, and type II behaviour and therefore must have quantised vortices.

As it is unclear to what extent the vortex quantisation will be modified by the inability to clearly define Φ_{eff}, it is assumed for all nanowires in this study that the vortices can be treated as Abrikosov vortices with flux Φ_0.

Pearl [13] was the first to study the effect when a magnetic field is applied at a normal to a superconducting sample where the thickness, d, is of the order of the bulk penetration depth. It was found that the penetration depth is enhanced by the proportion λ/d to:

$$\lambda_\perp \approx \lambda^2/d, \tag{2.37}$$

which can be very large for typical thin films.

2.2.6 Vortex Motion

In most applications vortex motion is undesirable as it causes dissipation at fields much smaller than H_{c2}. As we have shown, in the absence of other forces, the transport current should accelerate the vortices indefinitely leading to resistance and heating. In reality this is not seen, except near T_c or H_c, and so there must be some general stabilising forces that inhibit vortex motion. The simplest case is that of a uniformly distributed, material dependent viscous drag force which is given per unit length as $\mathbf{f_{drag}} = -\eta\mathbf{v}$. In a steady state this should balance the current driven force:

$$J_s\Phi_0 + \eta v = 0, \tag{2.38}$$

which induces an electric field from $\mathbf{E} = \mu_0\mathbf{H} \times \mathbf{v}$, such that the resistivity becomes:

$$\rho_v = \frac{E}{J} = \frac{\mu_0 H \Phi_0}{\eta}. \tag{2.39}$$

In general there are two other forces which affect the vortex motion, the force provided by pinning sites and the Magnus force. The Magnus force is a general property of vortices, and superconducting vortices are no exception [14]. The force is caused by circulating currents, which provide a small transverse force to a travelling, spinning object. Magnus forces are generally considered small relative to other forces on vortices.

Vortex motion, and therefore the superconducting properties are highly dependent on the pinning present in the superconductor. Local defects can cause a suppression in the local superconducting pair density, enabling the preferential stabilisation of a vortex at a particular site. Due to this stabilisation dissipationless superconductivity can exist at higher fields than H_{c1} until the Lorentz force exceeds the pinning force. Vortices in this picture can be expected to move in local bundles jumping between pinning sites.

2.2.6.1 Flux Creep

The occurrence of resistive flux motion in a steady state must be due to thermal fluctuations. These provide energy to allow bundles of vortices to overcome the local pinning potential and are then trapped at another pinning site after dissipating some amount of energy. Many such events collectively provide a steady resistance. There will be some average vortex velocity, which is less than that of an unpinned vortex. The rate of the bundle jumping can be described by a rate equation which depends upon the temperature. The Anderson-Kim flux creep theory assumes a rate of the form:

$$R = \omega_0 e^{-F_0/k_B T}, \qquad (2.40)$$

where there is a characteristic frequency for the bundles, ω_0 and a free energy barrier to overcome, F_0.

The addition of a transport current to this rate based creep motion provides a dominant direction of motion by effectively tipping the pinning potential landscape, preferentially moving vortices to one direction.

2.2.7 Vortex Barriers and Periodic Modulation

The interaction between vortices and the surface of the host superconductor was calculated by Bean and Livingston in 1964 [15]. The basic formulation includes an image force which results from the interaction with an "image" vortex of opposite rotation. The "image" is analogous to a mirror image, where the superconductor surface is the mirror. The "image" vortex provides an outward force, while the bulk Meissner screening of the external magnetic flux provides a force inward to the sample centre. The competing forces have different length scales and so the resulting vortex energy profile is that of a barrier at the superconducting surface. The barrier gives an adjustment to the field at which a vortex may enter or exit a superconductor. This is a good starting point to understand the discussions of this section. However, further details are required to generate a periodic barrier to vortex motion which could result in a periodic resistance.

Early theoretical work on vortex lattice configurations in the plane of a thin film by Carneiro [16] show that vortices form in rows, at the addition of each row the lattice goes through a period of instability and stability. This has been experimentally verified using near in plane magnetometry to probe the rearrangement fields, which are accompanied by maxima in the magnetic flux measured out of plane [17]. Studies of this phenomena show that it has a non-monotonic dependence on applied magnetic field, i.e. the step between stable configurations is larger at larger fields.

Several studies have discussed vortex motion to explain an OMR effect. Wang *et al.* observe a resistance peak with re-entrant superconductivity in the magnetoresistance (MR) of a $Mo_{0.79}Ge_{0.21}$ nanostrip with the magnetic field parallel to the current [18]. The effect is not observed in any other orientation and so it is claimed that this is because it is a special case for this sample. They explain the re-entrant behaviour through simulation of a superconductor with a differing density of pinning sites. These pinning sites create a twisted and strained vortex lattice, in order to overcome the strain created by an increase in field, vortices bend and move creating a voltage. This process increases the resistance until the field strength can

straighten out the vortices and the voltage decreases or is removed. At higher magnetic fields, such as $\mu_0 H_{c2}$ the resistance must go to the normal state resistance. In this study, the magnetic field is parallel to the current, and so only bent vortices with a component of flux perpendicular to the current, can be moved by a Lorentz force. The model could be extended to include several periods of twisting and bending followed by periods of straightening, giving an OMR effect. This periodicity would rely on the introduction of more vortex rows to add new stages of vortex bending. This model requires the current and field to be parallel, which does not apply to our observations and many others. In our case the OMR cannot be described by twisting of vortices only.

A practically applicable approach to vortex edge barriers is proposed by Berdiyorov *et al*. [19], wherein it is proposed that the interplay between the Meissner, transport and vortex screening currents can be used to describe vortex barriers and explain periodic resistance events. This can be understood by considering the density of the screening current, as illustrated in Fig. 2.3. Three stages of vortex entry are shown. Initially a potential vortex exists outside the superconductor. Upon attempted entry, the magnetic flux at the point of entry increases, which in turn results in an enhancement of the screening current density at that point. The high current density acts to expel the addition flux if the vortex does not have enough energy to overcome this barrier. In the case that the vortex core can enter the screening current associated with this flux wraps around the core and now reduces the surface screening. The vortex is now formed and will drift to the centre of the superconductor. With the addition of a transport current, the vortex will have a preferential direction of motion.

The explanation by Berdiyorov *et al*. [19] is a similar approach to Bean and Livingston. By noting that a local high current density is energetically unfavourable and unstable, we can see that there are points in the passing of a vortex that would cause a high current density and thus an unstable state. Vortex entry/ exit deforms the otherwise uniform screening current creating higher density current areas.

The situation so far has a barrier to vortex entry and exit, manifested in the deformation of the surface screening, however this is not sufficient to have periodic barriers. The key is to consider the arrangement of vortices, if we impose some periodicity into the rate of the increase in the vortex density we can create magnetic field periodic screening currents, and thus periodic barriers. The rate of increase in vortex density is observed to be periodic by Brongersma *et al*. [17]. Peaks in out of plane magnetic flux are calculated to occur at applied magnetic field values at which the vortex lattice is expected to reorganise. The implication being that the uncompensated flux and frustration builds before a vortex lattice rearrangement, which itself modulates the out of plane flux. Due to the presence of edge barriers, vortices are most stable when in uniform rows. As the field is initially increased beyond the first flux penetration, vortices form a single row, which will become tightly packed until a new row must form. This process continues until the lattice fills the area of the superconductor. This evidence shows that vortices do not simply fill the superconductor in an orderly fashion but frustration can lead to oscillations in the rate of change of vortex density.

The local current density at any point in the superconductor is a summation of contributions from the transport, bulk Meissner screening and vortex screening current densities. The following is a simplified toy model, based on the current density arguments of Berdiyorov *et al*. [19]. It is pertinent to unpack the model in order to gain insight into how the model creates a periodic MR using edge barriers defined using local current densities.
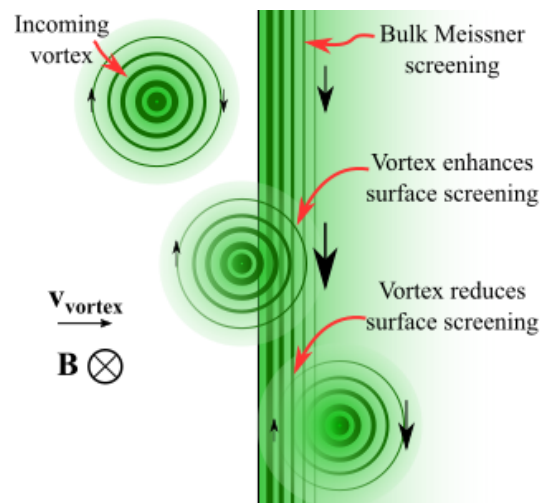
Figure 2.3: An illustration of the three main stages of vortex entry, considering the screening current interference. The current density is signified by the density of lines and the intensity of colour. At the top, a vortex is incoming - this is an imaginary object which deforms the bulk screening as it nears the surface. In the middle, the deformation of the screening current by the vortex is shown. This is a higher energy state than when the vortex is outside or deep inside the bulk. An enhancement of the screening current at the crest of the vortex acts against the entering vortex. At the bottom, the vortex has entered. The bulk Meissner screening current and the vortex screening current interfere destructively, this acts to stabilise the vortex.

For a small nanowire, the transport current can be taken as approximately constant across the wire. The bulk Meissner screening current is described by an exponential decay from the surface, over the characteristic length scale λ. The vortex screening current is fully described by the first order Bessel function, K_1. Here the profile of a Pearl vortex is used, which is a good approximation to the Bessel function at small r, which is appropriate for this study. The resulting total current density for a 1D line across a superconducting wire, with a single vortex at position x_v is:

$$j_{tot} = \frac{I_{app}}{2x_0 t} + \frac{\mu_0 H_{app}}{\mu_0 \lambda} \left(exp\left(\frac{-(x+x_0)}{\lambda}\right) - exp\left(\frac{x-x_0}{\lambda}\right) \right) + f(x), \tag{2.41}$$

with:

$$f(x) = \begin{cases} \frac{\phi_0}{2\pi\mu_0\lambda^2}\frac{1}{r}, & |r - x_v| - \xi_0 > 0 \\ 0, & |r - x_v| - \xi_0 < 0, \end{cases} \tag{2.42}$$

where x is the dimension across the width of the superconductor centred at the middle, x_0 is half the width and r is the distance from the center of the vortex. $f(x)$ is the current density for a Pearl vortex with core radius ξ_0.

Fig. 2.4 (a) shows this equation for a line across the width of a superconducting strip. With no vortex the transport current and Meissner screening result in an approximately linear current profile. When a vortex approaches from the left (negative x) the screening current is enhanced (black, $x_v = -1.5x_0$). If the vortex has enough energy to nucleate, the core of radius ξ forms, as soon as the current fully wraps around the core, the current density at the surface is reduced stabilising the vortex and pushing it into the superconductor (blue, $x_v = -0.75x_0$). At the centre of the wire, the vortex screening current balances the Meissner screening current at each surface equally (pink, $x_v = 0$), stabilising this position. On exit, the screening current at the exit edge is first enhanced by the vortex and then reduced, mirroring the entry process ($x_v > 0$). The total current at the entry and exit surfaces is given in Fig. 2.4 (b) as a function of the position of a singular vortex, by tracking the position of a vortex it is clear that there is a barrier at both entry and exit. The addition of further vortices modifies the barriers, as long as the width of the wire is small enough that the vortex screening current is non-negligible at the edges. These vortices, which we will add at the centre of the superconductor for simplicity, act against the entry and exit barriers as the screening currents are in the reverse direction. This effect is illustrated in Fig. 2.5 where a large density of vortices is shown schematically to reduce the total screening current at the surface.

Here it would be possible to add a vortex to locally negate the Meissner screening. However, this is an unreasonable approach, as the flux begins to enter the vortices in the wire will move away from the entry point and stabilise near the centre. Vortices of the same helicity are repulsive, and anti-vortices are not expected to play a large role in systems when a magnetic field is applied. However, we do know that the vortices will arrange near the centre of the wire in rows, and the formation of new rows is associated with frustration. The simplest picture to provide a periodic vortex entry and exit, is that due to vortex packing and the subsequent rearrangement, the system goes through periods where the total trapped vortex number does not increase and periods where the lattice rearranges to allow the number of trapped vortices to increase. In reality the modulation would be much smoother and far less

uniform. The finer details of vortex lattice formation are not important to this toy model interpretation of OMR. The number of vortices trapped in in the toy model sample, n_{Model}, is:

$$n_{Model} = \begin{cases} n - \mod(n, n_{stable}), & \mod(n, n_{stable}) < n_{stable}/2 \\ n + \mod(n, n_{stable}) - n_{stable}, & \mod(n, n_{stable}) > n_{stable}/2, \end{cases} \tag{2.43}$$

where n is the integer number of vortices centred at the middle of the wire that will successfully compensate the Meissner screening. n_{stable} is the number of vortices that fill each row, before frustration causes the rate of change of vortex density to decrease - or in this model completely stop. The first part of the Eq. 2.43 is the frustrated section, where vortices cannot enter and $dn_{Model}/d\mu_0 H = 0$. The second part is the rearrangement section where the vortex number increases rapidly. The number of vortices is included in the inset of Fig. 2.4 (c), showing a step like increase.

n_{stable} can be altered to account for a longer sample, and is directly proportional to the calculated period. The number of stable vortices that we include in this model for a typical Nb sample is 10. This is found through modelling for a sample with very similar parameters to those in this study in the work by Berdiyorov *et al.* [19]. Due to the formulation of n_{Model}, the period is inversely proportional to the width of the wire as shown in the inset of Fig. 2.4 (d). If it can be assumed that large local current density modulations correspond to a large OMR effect, the OMR magnitude should be larger for small widths. This could, however, be an artefact from the assumption that the vortices are situated in the centre of the sample, and as such the influence of the vortex screening current is smaller at higher centre to edge separation.

The toy model can be applied to the materials and samples used in order to give estimates of the OMR period, Fig. 2.4 (e) shows the model applied to Nb and In-SnTe for typical values with a period estimate of 0.83 T for Nb and 0.33 T for In-SnTe. These values are comparable to those observed in our experiments. The assumption that the vortices are all trapped in the centre of the wire leads to a large n_{stable} value required to reverse the effect of the Meissner screening for the In-SnTe sample. The assumption that the vortices are in the centre means that the effect of each vortex is much smaller at the edges, this is especially so for the In-SnTe samples which are larger in size. In reality the vortices would arrange in such a way that there would be a greater contribution to the current density at the surface. Extending the model to include a realistic vortex distribution would yield more realistic values for n_{stable}, however, that is beyond the scope of this model. While far from a complete simulation and requiring a specific form for the number of vortices, this toy model uses a simple idea to replicate the modulation of the edge current density in a superconducting nanowire, and therefore the entry and exit barriers for vortices. This gives a path to understand vortex motion as a cause for OMR using the theory proposed by Berdiyorov *et al.* [19].

The simulation by Berdiyorov *et al.* [19] includes the effect of disorder, current density, length, and width although only the effect of disorder is discussed with respect to the period of oscillations. Edge defects reduce the critical field for vortex entry and exit, this results in a general reduction of the onset field for resistive events. The non-uniformity of defects may also provide a broadening of the field width for each event. Defects alter the resistance to vortex flow, for instance an isolated defect can pin a vortex, as it creates a lower energy position. Conversely, a chain of defects across the sample provide a path for vortices to hop between
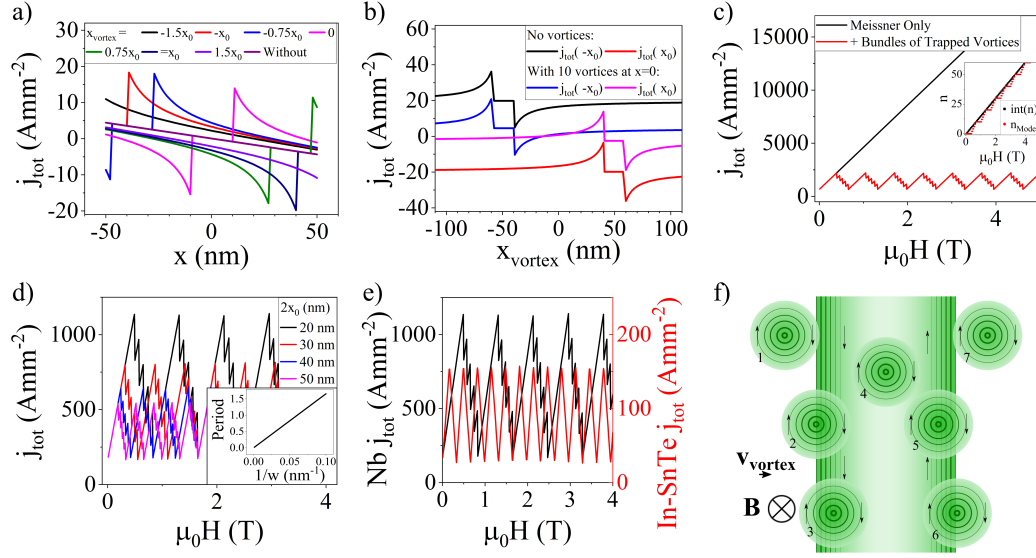
Figure 2.4: A toy model of the local current density in the vortex motion induced OMR model, inspired by the detailed simulation by Berdiyorov *et al*. [19]. The local current density, j_{tot}, is calculated using Eq. 2.41. The vortex core is taken to have a radius equal to the $\xi = 10$ nm. a) The profile of the current density across a nanowire of thickness 100 nm, without a vortex and with a vortex at various positions. The vortex positions are shown in panel (f). b) The current density at the edges of the nanowire vs vortex position, x_{vortex}, for two scenarios: without vortices trapped in the wire and with ten vortices trapped in the wire. c) A comparison of the screening current due the Meissner effect and with the additional effect of trapped vortices. The inset shows the number of trapped vortices, n_{model}, required to generate the periodic modulation in j_{tot}, and the integer int(n) used in Eq. 2.43 to generate n_{model}. d) The width dependence of this toy model. The inset shows the dependency of the toy model OMR period on the nanowire width. e) The toy model applied to typical Nb and In-SnTe parameters. For Nb, $x_0 = 10$ nm, thickness = $2x_0 = 20$ nm, $\lambda = 400$ nm, and $n_{stable} = 10$. For In-SnTe, $x_0 = 200$ nm, thickness = $2x_0 = 400$ nm, $\lambda = 1000$ nm, and $n_{stable} = 200$. f) A diagram of the vortex positions from panel (a), labels 1 to 7 indicate positions $x_{vortex} = $ -1.5x_0, -x_0, -0.75x_0, 0, 0.75x_0, x_0 and 1.5x_0.
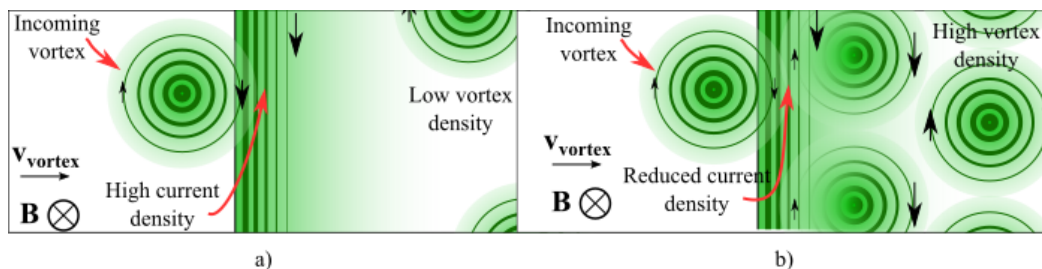
Figure 2.5: Modulation of the vortex entry barrier by proximity to a high density of vortices. a) A low density of vortices has no effect on the surface current density and entry of a new vortex. b) A high vortex denisty acts to lower the surface current density and so lowers the energy barrier for further vortex entry. This allows periods where vortices can enter more freely. This image is also applicable to the exit barrier in reverse.

points of low energy, and travel more readily. This causes the OMR effect to be semi-periodic, rather than the ideal case which is exactly periodic. The resistance peaks will also be generally broadened by the competing pinning effects, resulting in overlapping events. Overlapping events can create a background resistance in MR measurements, which makes the isolation of the OMR effect from other background resistance effects problematic.

Mills *et al*. observe an OMR effect in a candidate 2D superconductor, $NbSe_2$, which they attribute to the vortices crossing the superconducting strip [20]. They also attempt to show the influence of pinning by surface adsorbates, by measuring the same effect at two pressures. However, as we will show, the effect is strongly dependent on sample temperature which cannot be the same at the two different pressures as the sample pressure is determined by the exchange gas in the cryostat. An OMR effect is convincingly reported in a proximitised single crystal Au nanowire, where the vortex travel distance is similar to that in our study [21]. In proximitised Au nanowires the OMR was observed to be exactly periodic with sharp peaks, which is expected by Berdiyorov *et al*. [19] when defects are negligible, as they are in the case of Au nanowires.

2.3 Other Periodic Magnetoresistance Effects in Nanoscale Superconductors

In the previous section, a periodic modulation of vortex entry and exit barriers provided a mechanism with which to generate periodic resistive events, however one must understand the main other periodic resistive effects that superconductors may exhibit before concluding that vortex motion is responsible.

The macroscopic wavefunction that describes superconductors leads to interference effects. The study and use of these effects has become more important as nanoscale lithography of superconductors becomes more accessible. In this chapter a cross section of the many celebrated interference effects are discussed. Examples of experimental observations are given, when appropriate.

2.3.1 Weber Blockade

Related to the principle of periodic entry and exit boundaries, is the idea that superconducting nanowires can act as the exact dual of a Coulomb blockade. The theory, formulated by Pekker *et al.* [22], uses many of the same arguments as Berdiyorov *et al.* [19], regarding vortex motion being modulated using electronic currents and magnetic fields. The difference being that the experiment is at a sample size limit, where a single vortex entry/exit dominates the transport. It is possible that this is a different formulation of the same idea, yielding distinctly different results. While others have tentatively suggested this as the cause of an OMR effect [23], convincing evidence is presented in Al nanowires in the form of critical current measurements which follow the zig-zag trends expected for a true Weber blockade [24]. There does not appear to be any clear feature of the Weber blockade experiment that separates it from the OMR observations. It is possible that this is simply a systematic, controlled motion, single vortex limit of the OMR observed in other wires where the probe is capable of revealing the associated Weber blockade signature. As alluded to, the Weber blockade observation experiment is similar to the OMR experiments: Al nanowires with thickness = 25 nm, width = 50 - 100 nm, and length = 1.5 - 4.5 μm with a magnetic field applied out of plane. The coherence length is 15 - 30 nm, similar to out experiment. From similar experiments, including our own, this should show an OMR effect, leading to the idea that these samples, measured using their methods are probing a special limit of the general OMR.

2.3.2 Little-Parks

Following the observation that superconducting cylinders trap quantised flux [25, 26], in 1962 Little and Parks investigated the effect on the critical temperature [27]. As expected, they observed a periodic shift in the T_c of a hollow cylinder, as a function of the magnetic field applied along the cylinder axis. As the field is increased the number of flux quanta inside the loop adjust to maintain a minimum system energy, stabilising the superconducting state. As the external field increases, T_c will decrease due to the screening currents generated. However, the compensation by the introduction of flux quanta rectifies this current generation and restores the critical temperature. The two competing effects result in an oscillation in the critical temperature with magnetic field which can also be observed as a periodic oscillation in the resistance during a magnetic field induced superconducting transition. Minima in T_c or resistance as a function of magnetic field are observed when the flux inside the cylinder is exactly half of one flux quantum. Maxima are observed when the trapped flux is exactly compensated.

The key requirements for the Little-Parks effect are to have a magnetic field to be parallel to the axis of a hollow cylindrical superconductor as illustrated in Fig. 2.6 (a). For an applied magnetic field that is not aligned to the cylinder, only the component along the cylindrical axis would contribute to the Little-Parks effect. The effect is exactly periodic in flux, and so when the flux is perpendicular to the axis the period should tend to infinity. The flux through the cylinder is, $\Phi = \mu_0 H / A$, where A is the area of the inner circle face of the hollow cylinder. For a solid superconductor sample with patches of poorly superconducting material, there may be potential that cylinders of normal material may form and give a Little-Parks effect. The area of these normal cylinders would be strongly influenced by the environment. For example,
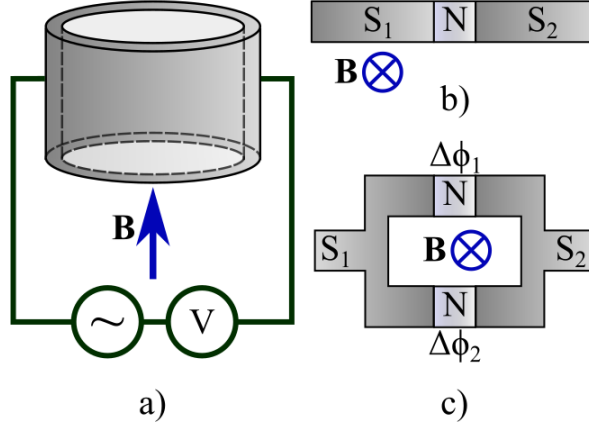
Figure 2.6: Little-Parks, Josephson junction, and a superconducting quantum interference device. a) The superconducting loop and measurement configuration required to detect the Little-Parks effect. b) A weak link, in this case a normal metal section (N), between two superconducting reservoirs (S_1 and S_2) of a Josephson junction. c) Two parallel Josephson junctions, forming a SQUID.

closer to T_c the cylinders should increase in size as the normal cylinders expand, resulting in a decreasing period as the flux through the loop is higher for the sample applied field.

2.3.3 Josephson effect

An insulating barrier between two superconductors creates a Josephson junction (JJ). This device has a zero voltage supercurrent:

$$I = I_c \sin(\Delta\phi), \tag{2.44}$$

where $\Delta\phi$ is the difference in phase between the two superconductors and I_c is the critical current of the junction. A typical geometry is illustrated in Fig. 2.6 (b). The phenomena was first postulated by Josephson in 1962 [28] and further expanded by Josephson in 1965 to include derivations which also include several incredible consequences of the discovery [29]. A detailed examination of the Josephson effect is not pertinent to this study, but it is worth noting that the effect arises due to the tunnelling of the superconducting wavefunction through the insulating barrier. The tunnelling probability in the two directions is proportional to $exp(\pm i\Delta\phi)$ and thus the sum is proportional to $\sin(\Delta\phi)$.

Below the junction critical current, I_c, there is no voltage across the junction, but above this value there is a voltage drop. A time oscillating current is generated by a JJ when there is a fixed voltage drop, V, across the junction. The junction phase difference is continuously modulated as:

$$\Delta\phi = \frac{2eV}{\hbar}t, \tag{2.45}$$

and thus results in the junction current:

$$I = I_c \sin\left(\phi(0) + \frac{2eV}{\hbar}t\right), \tag{2.46}$$

where $\phi(0)$ is the phase across the junction without a voltage applied.

While here the discussion has been brief and only covered a few aspects of JJ, there are many effects associated with it including the superconducting quantum interference device (SQUID) effect.

2.3.4 Superconducting Quantum Interference Devices

Following from the Josephson effect, quantum interference is observed when two JJs are connected in parallel. These devices are called superconducting quantum interference devices, affectionately known as SQUIDs. A typical geometry is illustrated in Fig. 2.6 (c). In a perfectly balanced junction, the current can be expressed as a doubling of the JJ equation. Here we can set the critical current across the junctions to be equal, but the phase difference across each junction is treated independently such that:

$$I = I_c(\sin(\Delta\phi_1) + \sin(\Delta\phi_2)), \tag{2.47}$$

where the subscripts 1 and 2 correspond to the two junctions. When an external current is applied, the phase across both junctions will shift by the same amount, $\Delta\phi_1 = \Delta\phi_2 = \Delta\phi$. However when magnetic flux, Φ, passes between the junctions, through the SQUID loop, there is generates a difference between the two initial phase differences,

$$\Delta\phi_1 - \Delta\phi_2 = \frac{2\pi\Phi}{\Phi_0}. \tag{2.48}$$

Thus the critical current of the junction becomes:

$$I = I_c\left(\sin\left(\Delta\phi + \frac{\pi\Phi}{\Phi_0}\right) + \sin\left(\Delta\phi - \frac{\pi\Phi}{\Phi_0}\right)\right), \tag{2.49}$$

where $\Delta\phi$ is the initial phase independent of the magnetic flux through the loop. This simplifies to become:

$$I_c = I_0\left|\cos\left(\frac{\pi\Phi}{\Phi_0}\right)\right|. \tag{2.50}$$

This critical current oscillates with a fixed period defined by the number of flux quanta penetrating the loop and is commonly used to provide a highly accurate method of measuring a magnetic field. Naturally, as the flux through the SQUID loop controls the period, only the component of magnetic field along the axis of the loop contributes. This results in similar magnetic field orientation properties as the Little-Parks effect.

Some of the early studies of OMR in superconducting nanowires claim that grains and weak points in the wire could form SQUID-like junctions [30–32]. However these studies neglect to fully explain how this forms a collective resistance oscillation for a macroscopic wire with many grains. They also do not discuss how these junctions would evolve as the temperature or magnetic field is increased. As the normal, weak points expand due to a higher temperature or magnetic field, the SQUID area would increase and accordingly decrease the period. In fact the period of most OMR observations is measured to be approximately constant during a magnetic field sweep and over the measured temperature ranges [21, 30–34].

2.3.5 Quantum Phase Slip Junctions

An exact dual to the Josephson effect is found through the duality of the superconductor quantum variables charge and phase. While a JJ is the tunnelling of charge from one superconducting well to another through a tunnel barrier, a quantum phase slip junction is the tunnelling of quantum flux along a superconducting nanowire. To generate this effect the superconducting wire must be narrower than the coherence length to allow quantum fluctuations to destroy sections of the superconducting state in the nanowire. The coherence lengths of the materials used in this study have been measured and are comparable to previous studies. Bulk Nb has a coherence length of 39 nm [35], and is suppressed when grown in thin films. Our measurements yield an average value of (11 ± 1) nm, which is very reasonable. Previous measurements find a value for $Sn_{1-x}In_xTe$ as 14.2 nm [36] and (14.4 ± 0.2) nm [37]. In our study we observe similar values with an average of (14 ± 2) nm. In quantum phase slip junctions, tunnelling of the quantum flux is associated with phase slippage of the superconducting condensate, which is quantised. The rate of phase slippage generates a voltage which can be controlled through microwave irradiation. The resulting effect is that of quantised current steps, the exact inverse of the Shapiro steps that are observed in JJs. A voltage standard is already defined using Shapiro steps, and it is hoped that quantum phase slip junctions could be used for a current standard [38]. Due to the requirement that the nanowire diameter must be smaller than the coherence length of the material, it is highly unlikely that we would be able to observed this effect with the smallest dimensions of Nb and $Sn_{1-x}In_xTe$ being 20 nm and 40 nm, respectively.

2.3.6 Unexplained Observations

Despite the wealth of possibilities to explain an oscillatory MR effect in superconducting nanostructures, there are some studies that struggle to match their observations without resorting to complex and unlikely explanations. Kunchur *et al*. being a good example where the overwhelming evidence they observe shows some unusual correlations that are not easily explained [34]. Johansson *et al*. simply ignore the quite clear oscillations in their data, subtracting it as a background to focus on some small oscillations that they claim are from the formation of SQUID loops [31]. Wang *et al*. observe an OMR effect in Pb bridges, which they tentatively suggest may be from SQUID-like interference. However, given the more recent developments by Berdiyorov *et al*. [19] a re-evaluation may show that these oscillations are due to vortex motion, which was not considered at the time.

2.4 Topological Materials

Over the following section we will introduce and explain non-trivial topology through key theoretical and experimental observations. Relevant advances in the area that provided inspiration for the inclusion of a candidate topological superconductor (TS) in this work with then be discussed.

2.4.1 Topological Insulators

Since the discovery of the quantum Hall state in 1980 [39] , the concept of topologically invariant states has been of major interest. It is understood that quantum Hall was the first example of a 2D topological effect with an insulating electronic band gap in the bulk and quantised gapless edge states. The state occurs in 2D semiconductor systems at low temperatures and large out of plane magnetic fields. This results in the localising of electron motion into quantised orbitals, and the formation of discrete Landau energy levels. The quantum Hall conductance is identified by Chern numbers, which are topologically invariant and so cannot be changed continuously by small deformations to the Hamiltonian of the system. For more information about the origin of the quantisation refer to Ref. [40]. Bernevig *et al.* [41] predicted the existence of the quantum spin Hall state, which has an inverted insulting bulk due to strong spin-orbit coupling, and results in spin-momentum locked edge states. The quantum spin Hall state is similar to the quantum Hall state, but with opposite spin states propagating in opposite directions. Counter-propagating spin states result in a pure spin current around the sample edge. Backscattering is also forbidden for these edge states, unless a scattering event can flip the spin, such as magnetic scattering events from impurities. This protection is simply due to the unavailability of states with the same spin in the reversed momentum direction. Counter-propagating spin edge states are called helical edge states, due to the spin-momentum correlation. The existence of the quantum spin Hall state was experimentally verified by Konig *et al.* [42] in a HgTe quantum well structure. The quantum spin Hall state is now recognised as a 2D topological insulator (TI), part of the topological materials class, with time-reversal symmetric surface states.

The inverted conduction and valence bands in 2D TIs is responsible for the surface states. In the bulk of a material the inversion does not affect the insulating properties. However, at any interface with a non-inverted medium, there must be a smooth connection between the conduction and valence band across the interface. The result of this connection is a pair of surface states that cross the Fermi energy, as shown in Fig. 2.7. Naturally, this band crossing at the edge produces metallic gapless edge states, which have a linear, Dirac-like dispersion at the Fermi energy. More generally, topological materials are defined by having non-trivial textures in the bulk electronic states. The non-triviality is quantified using a topological order parameter. The values this number can take depend upon the symmetries of the system in question and the origin of the topological non-triviality. TIs, such as the quantum spin Hall state, have a $\mathbb{Z}_2$ topological invariant. For topologically trivial insulators $\mathbb{Z}_2 = 0$; for topologically non-trivial systems such as TIs $\mathbb{Z}_2 \neq 0$. There are various sub definitions that define further the nature of specific TIs [43].

The TI state naturally generalises to 3D [44–46], where the bulk states are insulating and the surface has gapless topologically protected metallic states. The surface states are robust against local perturbations through the same arguments as in 2D. The first experimental confirmation of a 3D TI was $Bi_{1-x}Sb_x$ [47], using incident photon energy modulated angle resolved photo-emission spectroscopy (ARPES). ARPES is useful tool to measure electronic band structure. It is the study of the energy and angular distribution of photo-emitted electrons from an illuminated sample. The energy and momentum of the electronic band structure can be mapped using the detected emission [48]. $Bi_{1-x}Sb_x$ was observed to have Dirac-like dispersion of the surface states, as expected for a 3D TI. In conjunction with transport measurements, this provided enough evidence to confirm the existence of the 3D TI state. For
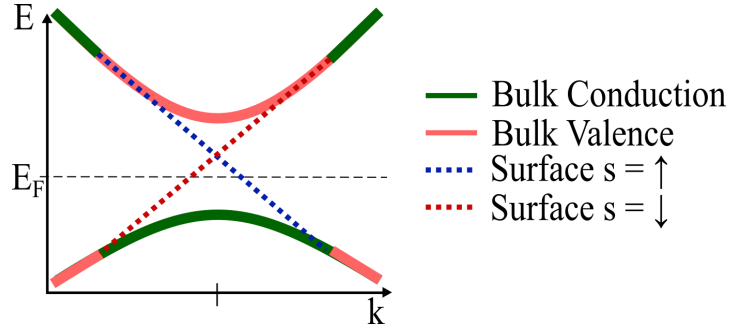
Figure 2.7: A schematic diagram of a section of a 2D TI showing gapped bulk electron bands, with a gapless helical edge state superimposed. The bulk valence and conduction band are inverted, as shown in green and orange. Blue and red dashed lines represent the counter-propagating edge states. 3D TIs have 2D surface states for which the band inversion manifests as a Dirac Cone.

more information on TIs, interested readers should access the review by Hasan and Kane [49]. The confirmation of the existence of TIs opened up the relatively young field of topological materials. As both insulators and superconductors have band gaps, with the potential for inversion, it was only natural to investigate the potential for a TS state.

2.4.2 Transport in Topological Insultors

Evidence of TI surface states can be observed through quantum oscillations. TIs Bi_2Se_3, Bi_2Te_3 and Sb_2Te_3 have been studied by fabricating nanowires, nanotubes, and nanoribbons through various growth methods [50–54] and recently, through the shaping of flakes of material using focussed ion beam milling [55]. Safdar *et al*. observed evidence for the topological surface states of SnTe nanowires through transport measurements where Shubnikov-de Haas and Aharonov-Bohm oscillations were observed [56]. Aharonov-Bohm oscillations are expected in a TI when a magnetic field is applied along the length of a nanowire and causes the metallic surface states to propagate coherently around the wire in closed loops. A voltage measured parallel to the wire oscillates with a period of one flux quantum or $\Delta\mu_0 H = \Phi_0 / A$ where A is the nanowire cross-sectional area. Shubnikov-de Haas oscillations can be observed in 3D TIs. These oscillations occur in the MR of a 2D electron gas, which is effectively the case for TI surfaces. Each surface can be treated as a 2D quantum spin Hall surface. As a magnetic field is increased, the Landau levels shift in energy. As the Landau levels pass through the Fermi energy, the electron scattering rate and so resistance changes. When the Fermi energy is at a maximum in the density of states, there is a maximum in the resistance. From Shubnikov-de Hass oscillations it is possible to calculate the surface state carrier density. The phase factor of the oscillations can be extracted which reveals whether the surface states are electron-like or 2D Dirac fermions. Furthermore, estimates can be made for the surface state cyclotron mass, Fermi wavevector, Fermi velocity, mean free path, mobility and Fermi energy.

Weak localisation (WL) and weak anti-localisation (WAL) are quantum interference effects. WL was originally formulated to describe the low temperature peak in resistance at

zero magnetic field observed in Si-MOSFETs (metal-oxide-semiconductor field effect transistors) immersed in an out of plane field [57–59]. Si-MOSFETs exhibit this phenomena as the conduction channels are disordered and confined spatially. This confinement leads to electron transport being described by a high density of scattering events. Weak localisation and weak anti-localisation are caused by quantum interference of electron paths. WL increases resistivity and WAL decreases resistivity. WL is caused by the constructive interference of two charge carrier paths that loop back to the start point. The result being that the electron is more likely to not travel forward and conduct electricity. Both paths scatter at the same sites, but travel in opposite directions. The application of a small magnetic field at normal to the loop rapidly destroys the constructive interference, reducing the resistivity. WAL, however, includes a spin-orbit coupling term. The spin-orbit coupling acts oppositely on the two rotation directions, rotating the carrier spins in the opposite sense. This gives a destructive interference, resulting in a higher probability of the electron travelling in a positive direction and contributing to the current flow. In a similar fashion to WL, a magnetic field destroys the interference and causes an increase in resistivity.

In a TI, the WAL does not occur simply due a spin-orbit coupling induced phase. In fact, the surface states are anti-localised due to a Berry phase picked up on a closed loop path, prohibiting the backscattering and localising of the surface states [60]. An applied magnetic field or magnetic impurities produce spin dependent energy changes which break time-reversal symmetry and disrupt the Berry phase. WAL and WL are commonly observed in systems with some spatial confinement, such as thin films. To generalise the effects to 3D TI, one can consider the surfaces each as as a thin conducting surface. At low bulk sizes there may be interactions between opposite surfaces and the bulk topology may also play a role. The 2D theory by Hikami, Larkin, and Nagaoka [57] can be adapted to all of these situations. There are two key parameters in the theory α and l_ϕ. α describes the nature of the surface states contributing to the WAL. In the presence of magnetic scattering $\alpha = 0$, when there is no magnetic scattering $\alpha = 1$, and when there is no magnetic scattering and spin-orbit coupling is strong $\alpha = \frac{1}{2}$ [57]. TIs for example, are expected to have $\alpha = \frac{1}{2}$ per single surface conducting channel.

Several examples of WAL studies in 3D TIs exist, however the methods and results vary. From the beginning, the definition of the measured conductance G varies. Some studies, define the conductance for the 3D samples as $G = \frac{1}{R}$, which is correct. Due to the fact that surfaces are the conducting channels other studies attempt to use a conductivity like definition, $G = \frac{1}{R}(L/W)$ [61]. This is in fact the conductivity for a 2D object and is in fact meaningless in the case of 3D objects. While generally inappropriate for 3D samples, it may be useful to approximate the conducting surfaces to match with the 2D HLN model. Many studies do not quote directly which method they used, potentially because of the accepted use of $G = \frac{1}{R}$. An additional issue encountered in 3D TIs is that the WAL should not influence the MR beyond $\sim 0.1T$, as this should be sufficient to break the time-reversal symmetry. However, this study and other works observe WAL up to 0.4 - 1 T [53, 61, 62]. The Zeeman energy of an electron with an applied magnetic field of 1 T is of the order of 1 meV. For this energy scale to be the cause of the WAL observed, the chemical potential must be distorted locally across the sample, otherwise the field and energy scale should be 0.1 T and 0.1 meV. Dislocations or non-magnetic impurities could cause a local chemical potential variation allowing for this range of magnetic field to be appropriate for the WAL observation. The TI in this study is in fact a topological crystalline

insulator (TCI), which does not rely on time-reversal symmetry. Further complicating the story with TCIs, is that there can be multiple surface states, leading to multiples of $\alpha = \frac{1}{2}$. The (100) surface projection of the SnTe bandstructure has four Dirac cones, while the (110) and (111) surfaces have two Dirac cones. This results in a maximum of $\alpha = 4 \times \frac{1}{2} = 2$ [63].

Fitting of data values of α are often in poor agreement with theory. For instance, a study of MBE grown TCI SnTe films report α values that vary between sample, depend on temperature and tend towards values that have no physical meaning, between 0.2 and 12 [61]. Another MBE film study of TCI, $Pb_xSn_{1-x}Te$, yielded $\alpha \sim 0.4$ [64]. When a reasonable value of α is found in a 3D TI [62], the method of extraction appears to be to remove 3D effects that do not depend upon the magnetic field angle. This is possible for thin films where 2D effects only dominate the signal for an out of plane magnetic field. There also appears to be some confusion in the literature as to how close to the half-integer values α should reasonably be. While the observation of WAL is a useful indicator that a sample may be a 3D TI, it is not concrete evidence, with issues of WAL signal extraction and justification for the observed values of α.

Superconducting TIs have high bulk carrier densities. This increases bulk effects, furthering the need to increase the surface to volume ratio. For superconducting nanowires, studies of the MR may be useful above the superconducting transition to elucidate the topological crystalline insulator surface states through such techniques as WAL analysis. Below the transition however the situation is not so simple.

2.4.3 Superconducting Topological Crystalline Insulator In-SnTe

The topological nature of TCIs arises due to crystal symmetries, as opposed to the time-reversal symmetry in TIs [65]. Narrow band gap semiconductor SnTe has strong spin orbit coupling and band inversion at the Brillouin zone L points. The L points in the Fermi surface are even in number and so SnTe cannot be defined as a TI. The L-points are also not at k=0, and so the surface states cross the Fermi energy at momentum $k = k_L \pm \Delta$. This means that the two opposite bands of the dispersion relation do not have equal or opposite momenta. Only when the symmetries of the rock-salt crystal structure, and the subsequent Brillouin zone symmetries are considered can the momenta be seen to be invariant under reflection. In essence, two Dirac cones centred at $+k_L$ and $-k_L$ share two sets of counter-propagating states. One pair with momentum $\pm k_L \pm \Delta$ and one pair with momentum $\pm k_L \mp \Delta$. This is illustrated in Fig. 2.8.

In the presence of mirror symmetry, a mirror Chern number can be defined. If non-zero, this topological invariant defines a TCI [66]. PbTe is a similar material to SnTe, however it is not a TCI. The distinction arises from the fact that the conduction and valence bands in SnTe are inverted at the L points, while in PbTe the bands are not inverted. This alters the mirror Chern number in SnTe by 2. As the bulk band structure of SnTe is topologically non trivial, there must exist topologically protected gapless surface states. Experimental evidence, using ARPES, observed a Dirac like dispersion of the projection of the L point onto the surface band [67]. TCI surface states have been proven to exist on all facets of SnTe crystals [68].

The doped TCIs $Sn_{1-x}In_xTe$ and $(Pb_{0.5}Sn_{0.5})_{1-x}In_xTe$ are seen as a promising candidates to host the TS state as they are superconducting TCIs. Both the undoped and doped materials can be grown into homogeneous single crystals with the rock-salt crystal structure. This structure
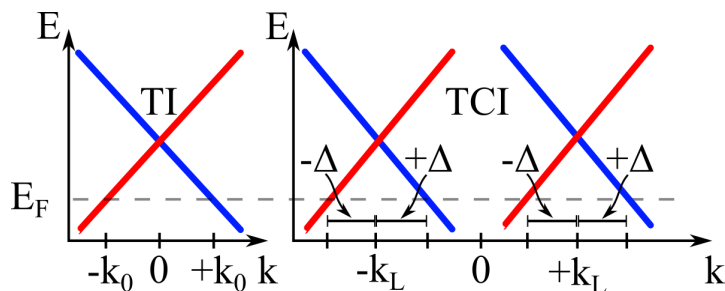
Figure 2.8: Cross section through the surface states of a TI and TCI. Colours blue and red signify opposite spins. TI surface states have opposite momentum vectors. The Dirac cones of the TCI surface states must be considered across the mirror symmetry to construct the required counter-propagating spin states.

is key to ensuring the mirror Chern number is non-zero. The materials both have strong spin-orbit coupling, low carrier density, a narrow bandgap, crystalline symmetry, and have Fermi surfaces centred on time-reversal invariant momenta.

SnTe itself is known to show superconductivity below 0.2 K, this arises from hole doping due to natural Sn vacancies and Te antisites. As these can depend on growth conditions, critical temperatures vary between samples [69]. Increasing the hole doping by substitution of Sn or $(Pb_{0.5}Sn_{0.5})$ for In has been shown to raise T_c to 4.5 K [37] and 4.7 K [70, 71], respectively. Despite a large doping concentration, of up to around $x \approx 0.4$, it has been shown that $Sn_{1-x}In_x Te$ is likely to retain the TCI surface states [72]. The question posed now is whether the superconducting TCIs become TSs.

Soft point contact spectroscopy of $Sn_{1-x}In_x Te$ [73] has provided some hope of topological superconductivity in this system. The spectroscopy probes the density of states of the material and revealed that there is a large population of Andreev bound states at the middle of the superconducting gap. This shows that the superconductivity is not s-wave, symmetric pairing, but odd-parity pairing. In this material system, the odd-parity pairing must be topological in nature. Contrasting evidence used Knight shift nuclear magnetic resonance measurements. This has the power to elucidate the pairing of the superconducting phase. The results suggest a topologically trivial singlet pairing [74]. The evidence in favour of a TS phase used single crystals, with a dopant level of x = 0.045. The evidence against a TS phase used polycrystalline samples with a dopant level of x = 0.04. At x $\lesssim$ 0.04, $Sn_{1-x}In_x Te$ undergoes a structural phase transition at temperatures below 100 K from cubic to rhombohedral [75]. The transition to a rhombohedral crystal structure may well break the mirror symmetry required to host topological surface states. This would also gap the edge states [66]. At x = 0.045 the structure remains cubic at all temperatures, and so mirror symmetry, and the mirror Chern number should be preserved. Following this argument the notion that polycrystalline $Sn_{0.96}In_{0.04}Te$ is a singlet superconductor, while single crystal $Sn_{0.955}In_{0.045}Te$ is a TS is not inconceivable. We require further evidence to fully identify the nature of the superconductivity in $Sn_{1-x}In_x Te$. In this study we explore $Sn_{1-x}In_x Te$ as a candidate TS, with the aim to provide paths to further study. For more information on topological crystalline insulators as candidate TSs, please see the review by Ando and Fu [76].

2.4.4   Growth of In-SnTe Nanostructures

In order to better study the electronic states of TSs it is important to maximise the surface to volume ratio, this will enhance the observable surface state contribution [77]. In addition, small dimensions can introduce a multitude of interesting effects. Crystal orientations must be well defined to fully characterise topological crystalline superconductors, as the orientation can greatly effect the transport. For instance, if one crystal surface is relatively large it will dominate electron transport. Single crystal nanostuctures can be grown by using vapour transport crystal growth in order to investigate these ideas.

Vapour transport growth (VTG) is a relatively simple method of growing nanoobjects of materials that nucleate in predictable crystal orientations. VTG is explained in Chapter 3. SnTe nanoplates with lateral dimensions of microns and thicknesses of a hundred nanometres were first grown by Shen et $al.$ [78]. Successful VTG of SnTe nanowires has since been shown by Li et $al.$ [79]. These growths of SnTe are relevant as we expect $Sn_{1-x}In_xTe$ to grow in a similar way. Growths of SnTe nanowires [56, 79, 80] use Au nanoparticles (GNPs) to catalyse a vapour-liquid-solid nucleation of crystals.

The use of GNPs to control and enhance the growth of nanowires is a well studied phenomena [81, 82]. However, some doubt remains over the physical nature of the growth. Studies disagree whether nanowires are grown by the vapour-liquid-solid mechanism or a vapour-solid-solid mechanism, where the nanoparticle does not melt. Dick et $al.$ have shown that the GNP assisted growth of InAs nanowires does not occur due to the vapour-liquid-solid transport process, as it does not occur when the Au is in a liquid phase [83]. In a vapour-liquid-solid mechanism the Au alloys with the growth material, which has the potential to introduce impurities. In addition, the GNP deposition method is often from solution, which has the potential to deposit organic contaminants on the surface. The growth of superconducting $Sn_{1-x}In_xTe$ nanoplates by Sasaki et $al.$ used no catalysts, risking no contamination [84]. It is generally considered that growths without GNPs yield nanoplates, while growths with GNPs yield nanowires.

A nanowire can be defined by considering the Bohr radius of the sample material. If the radius of the wire is smaller than the Bohr radius, then the transport should be influenced by the smaller dimensions. In the case of topological materials, the surface states should begin to dominate transport. For SnTe the Bohr radius has been calculated to be 95 nm [85]. We can expect to observe some effects associated with the surfaces states with samples of this size.

Superconducting nanowires, with a radius of ~ 200 nm, have been grown by GNP catalyst enhanced VTG by Kumaravidel et $al.$ [86]. In Chapter 5, evidence for contamination in growths using GNP catalysts is presented, using EDX elemental analysis. This finding has been published [3], the author of this work is joint first author with Sam Atherton. In response, Kumaravidel et $al.$ present EDX that does not show GNP contamination. The difference in observations could arise from the differences in growing methods, such as temperature and pressure. However, the EDX mapping in this work observed Au contamination near the limit of the resolution, ~0.1%, and so a smaller level of contamination would not be observable. Even though a smaller level of contamination is beyond the limit of the technique, it could be detrimental to the properties of the material.

2.4.5 Topological Superconductors

To extend the TI picture to superconductors, we take the Hamiltonian for TIs to be analogous to the Bogoliubov-de Gennes Hamiltonian for TSs. The superconducting bandgap being analogous to the insulating gap [87]. Due to the purity of samples available and the relatively early discovery of a non-trivial topological phase in this system, the most studied example of topological superfluid states is the unconventional p-wave superfluid ^{3}He [88].

Odd parity pairing of the superconducting state lies at the cornerstone of topological superconductivity; in fact, it is recognised as the main criterion when an odd number of time reversal momenta are enclosed within the Fermi surface [89, 90]. Odd parity pairing is defined by:

$$P\Delta(\mathbf{k})P^\dagger = -\Delta(-\mathbf{k}), \tag{2.51}$$

where P is the inversion operator, which flips the coordinates of the state, and as usual Δ is the BCS superconducting pair potential, which has a dependency on the momentum vector $\mathbf{k}$. For a single-band superconductor the most simple solution to Eq. 2.51 is the spin-triplet state. Higher energy states such as an f-wave pairing are also valid [84]. Some proposed TSs have odd parity pairing due to large spin-orbit coupling, this is predicted to make the odd parity superconducting state robust against non-magnetic impurities. This robustness overcomes the obstacle that unconventional superconductivity is usually highly susceptible to disorder [91]. Topology in 3D time reversal invariant TSs is defined by an integer winding number in Hilbert space.

2.4.5.1 Majorana Fermions in Solid State Physics

In 3D TSs, Majorana fermion quasiparticles are theorised to exist at surfaces interfaced with topologically trivial materials [92, 93]. It has been proposed that the Majorana fermions can be localised into Majorana zero modes at the real space surfaces of 3D TS using vortices [94]. Majorana fermions were first theorised by Ettore Majorana in 1937 [95], through consideration of Dirac's particle equation, with a non-complex, real, solution. The result is a spin half particle that is equal to its own antiparticle. The creation operator of the Majorana fermion is a sum of the electron and the hole operators, $\gamma_j = c_j^\dagger + c_j$. γ_j is equal to it's own conjugate, $\gamma = \gamma^\dagger$, and thus is also the creation operator for the antiparticle [96].

The Majorana fermion properties include: non-Abelian statistics, non-local correlations and an Ising magnetic response [97]. If discovered in a controlled environment, this could lead to exciting physical studies with potential in future topological quantum computing applications. One property thought to be useful for computing is the braiding operation, which exploits the non-Abelian statistics to use topological phases to encode information. This would allow new types of computation. Topological protection also prevents small perturbations to the state, and so Majorana fermions should be stable and immune to decoherence.

In order to create Majorana fermions in solid state systems, it is necessary to formulate a way to form a charge neutral, spin-half quasiparticle. Superconductivity provides solutions to these problems. The superconducting condensate provides a reservoir of particles with charge -2e. The quasi-particle charge -e becomes irrelevant as the addition or removal of a Cooper pair has no consequence for the overall state of the system. This situation occurs through

consideration of the fact that a negatively charged electron can be considered to be equivalent to a positively charged hole plus one pair of electrons in a Cooper pair. The same can be said for the reverse, the charge of a hole is equal to that of an electron minus a Cooper pair. The Cooper pair can be borrowed or loaned from or to the condensate, to create the particle-hole charge symmetry, by making the charge of both the electron and hole effectively irrelevant. In superconducting systems the Fermi energy is at the midpoint of the band gap. Naturally, this introduces particle-hole energy symmetry, which is also key. The overall effect is that the differences between electrons and holes are removed. The resulting electron-hole superposition or Bogoliubov quasiparticle can be formed with a real quantum wavefunction. This is the Majorana quasiparticle. Only when at zero energy, at the superconducting gap midpoint, does the quasiparticle truly behave as a Majorana fermion. The density of states for Majorana quasiparticles is maximum at zero energy and it is robust to small perturbations due to the topological protection of the state. It is this zero energy mode that if localised to a point on the surface could be used to perform braiding. For more information on quasi particle Majorana fermions in TSs, see the review by Sato and Fujimoto [98].

2.4.6 Detection of Topological Superconductivity

Clear detection of TI surface states is possible through transport and ARPES studies. The bulk contribution to transport can be reduced by material engineering and the surface states can be accessed by ARPES at reasonable temperatures. In contrast, TS surface states cannot be probed in a straightforward fashion. Majorana fermions have no direct charge signal, furthermore the superconducting bulk would short circuit any resistance. ARPES cannot be performed at very low temperatures, due to the energy generated in the procedure, and so the T_cs of TSs cannot be achieved in ARPES apparatus. Other methods have been used or proposed to try and capture evidence for surface states on TSs, here is a brief discussion of a few methods that are relevant to this work.

An alternative method to probe the density of surface states of a candidate TS is by tunnelling spectroscopy techniques. As mentioned previously, point contact spectroscopy is a powerful technique to probe the density of states in and around the superconducting band gap. The tunnelling probability, and therefore current measured, depends upon the density of states at a point probed by an atomically sharp point contact. In the work by Sasaki *et al.* [73] a "soft" point contact was used, which was shown to yield the exact same Andreev reflection as conventional, atomically sharp, point contact spectroscopy. Related to the study of the tunnelling current through a point contact is the study of surface states using scanning tunnelling microscopy. Scanning tunnelling microscopy studies have claimed to observe Majorana fermions in a chain of Fe atoms on a superconducting Pb surface [99]. Both spectroscopic studies rely on the occurrence of a large density of states at zero-energy, the Majorana quasiparticle states. In spectroscopic studies the bias across the tunnelling point controls the energy being probed in the density of states, zero bias equates to zero energy. Majorana fermions are expected to be found at the mid gap as this is the point of zero energy. There are many other reasons for a zero-bias conductance peak, but by eliminating them experimentally the peak can be attributed to mid gap Majorana fermion states.

It is expected that TS JJ should have a 4π periodic AC Josephson effect as the Majorana states allow single charge, -e, transfer across the junction [100, 101]. This is distinct from the

usual tunnelling in Cooper pairs with double charge, -2e. Single charge transfer is allowed due to gapless Andreev bound states of the TS. These gapless states are topologically protected resulting in an expected higher transmission probability than other modes through the junction. However, if the junction is gapped, conventional modes in the junction are significantly higher in number, and will dominate the periodicity. Various attempts were made using proximity induced topological superconductivity in SC/TI/SC JJs [102–113] and many signatures of Josephson currents and even a topological phase were observed, however initial investigations struggled to observe the expected 4π periodic interference. The failure of these devices arises from the bulk superconductivity dominating the junction signal. A SQUID device has been fabricated from proximity induced SnTe [114], again only 2π periodicity was observed. Specific experimental arrangements can be made to enhance the 4π contribution. 4π periodic effects have since been observed in a Nb/ HgTe/ Nb junction [115], and other JJs [116–118], providing evidence for the Majorana surface states.

Yamakage *et al*. predict that through the Josephson effect, it should be possible to detect bulk odd parity pairing and surface helical Majorana states. This is at a JJ between an s-wave superconductor and a TCI-based TS. Under a mirror reflection operation, s-wave pairing is even, while the TCI-based TS pairing, A_{1u} or A_{2u}, is odd. Mismatch in the pairing mirror symmetry causes the most dominant order of the resulting Josephson current to be $J(\phi) \propto \sin(2\phi)$, instead of the typical $\sin(\phi)$ dependence [119]. A SQUID fabricated out of parallel s-wave/TCI-based TS junctions will be able to detect the $\sin(2\phi)$ Josephson current [119]. The work by Yamakage *et al*. also anticipates an anomalous temperature dependence of the Josephson current in TCI-based TS/TCI-based TS JJ. These are proposed to have a strong dependence on the spin-helicity of the Majorana states across the junction. At low temperature, the Josephson current between two TCI-based TSs of like helicity increases with decreasing temperature. Whereas, between two TCI-based TSs of opposite helicity the Josephson current decreases with decreasing temperature. Measurement of this effect could provide distinct evidence of the spin locked nature of helical Majorana states. Using a VTG $Sn_{1-x}In_xTe$ nanowire, it may be possible to create a TCI-based TS / TCI-based TS JJ by creating a weak link in the wire. A TCI-based TS /non-superconductor/ s-wave superconductor JJ could be fabricated by patterning an s-wave SC, such as Nb, onto a VTG nanowire with a barrier layer in between.

Majorana fermions have zero charge, to satisfy particle-hole symmetry. However, there are expected to be signatures from thermal conductivity. Gnezdilov *et al*. [120], predict a Wiedemann-Franz type relationship between the thermal conductivity, $G_{thermal}$ and the shot noise, P_{shot} across a device simply made from a grounded TS contacted with two normal metal wires. Through electron-hole symmetry and time-reversal symmetry, the two parameters are related by $\frac{G_{thermal}}{P_{shot}} = \frac{\mathscr{L}T}{eV}$, where $\mathscr{L}$ is the Lorentz number, T is the temperature and V is the voltage across the normal metal contacts. Various perturbations to the ideal are considered, such as the introduction of disorder which does not affect the ratio. Analogous to the Wiedemann-Franz relation for thermal and electrical conduction for metals, but with the electron charge replaced with a Majorana change variance. The variance in charge due to the electron-hole superposition that forms the Majorana.

CHAPTER 3

Experimental Methods
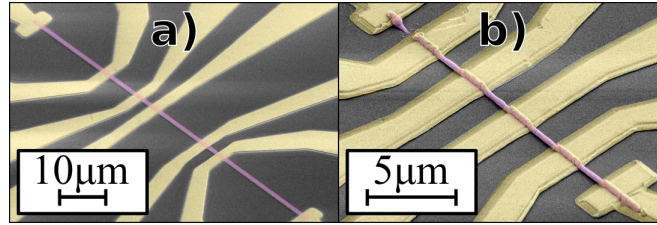
Figure 3.1: Scanning electron microscope images of nanowires of a) sputter deposited, lithographically defined Nb and b) vapour transport grown, naturally defined In-SnTe. The nanowires are highlighted in magenta and the Au electrical contacts are highlighted in yellow.

This chapter will introduce the various methods used to fabricate and characterise the superconducting samples discussed in the following chapters. There are two main sample preparation processes: Nb samples were grown by DC sputter deposition with lateral dimensions defined by optical lithography; and In-SnTe samples were synthesised by vapour transport growth where dimensionality is defined by crystal nucleation. Fig. 3.1 shows an example nanowire for both materials. Electrical contacts were fabricated by electron beam lithography, optical lithography, sputter deposition and thermal deposition. Additional steps are included to describe the manufacture of In-SnTe bulk source material used in vapour transport growths. Finally, the low temperature transport techniques used to characterise the final devices and several other characterisation techniques are described in the context of determining sample quality.

The Nb sputter deposition process was optimised by Dr Mannan Ali. Crystal growth procedures and equipment set up were performed by the author with advice from Dr Satoshi Sasaki and Dr Mannan Ali. Cleanroom fabrication processes were designed with assistance from Dr Mark Rosamond, Dr Georgios Stephanou and Dr Gavin Burnell. Gold nanoparticle dispersions and growth on nanoparticle substrates was performed by the author and project students: Samuel Atherton, Connor Wade, Elliot Dransfield, Matthew Vaughan, Gunasheel Krishnaswamy. EDX was facilitated and performed by Alexander Kulak of the School of Chemistry, University of Leeds.

3.1 Sample Fabrication

All samples were grown on Si, which was chosen during fabrication optimisation tests. As all magnetotransport measurements are performed at temperatures below 20 K, the conductivity of the substrate can be neglected. Thermally excited carriers in the Si will freeze out at low temperatures, giving an insulating substrate. Prior to growths, samples without lithographic patterns were cleaned using Acetone in an ultrasonic bath and then rinsed in IPA. This is blown off with dry N_2, rather than being allowed to evaporate, to prevent residue and contamination. Samples which were grown through a lithographically defined mask were developed in a cleanroom and then experienced a minimal amount of environmental exposure before deposition.

3.1.1 DC Magnetron Sputter Deposition

The principle of sputtering uses a highly excited, heavy, inert gas in the form of a plasma to bombard a target material, from which atoms become ejected. The process is illustrated in Fig. 3.2. The film quality can be very high and so the process is used commonly in research and applications. There are various types of sputter deposition [121], but in this work only DC magnetron sputtering in a pure Ar atmosphere was used.
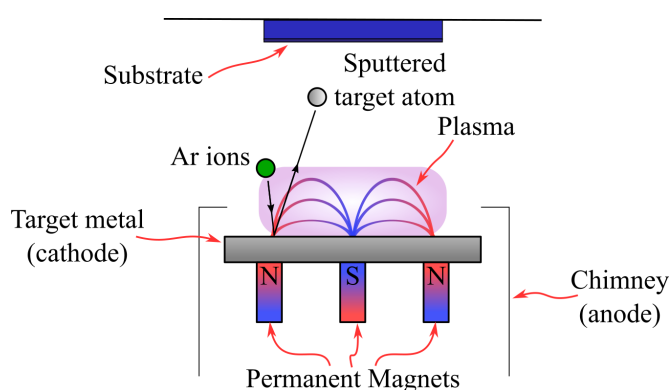
Figure 3.2: Schematic of DC magnetron sputtering of a target material onto a substrate. A large bias between the chimney anode and the target cathode generates a plasma, which is confined and accelerated by the permanent magnets below.

The base pressure of the chamber was typically 10^{-8} Torr with the use of a cryogenic pump and a Meissner trap, through which a supply of liquid nitrogen flows from an hour before growth until all samples are grown. The Meissner trap acts by freezing out residual water vapour from the chamber. When the partial pressures of the main contaminants, H_2O and N_2 were reduced to a satisfactory and stable level, pure Ar (99.9999%) was introduced and maintained at a pressure of 2.5 mTorr. A DC voltage was used to ionise the Ar gas into a plasma, localised above the target material. The target acts as the cathode, while a columnar chimney acts as the anode, in the ideal case this gives a radial electric field. Magnetron sputtering uses permanent magnets to confine the plasma, maximising the energy transfer from the Ar ions to the atoms of the target metal. The details of the energy transfer can be quite complex, however the majority of processes involve the ejection of atoms from the target surface. Liberated metal atoms diffuse through the chamber to the substrate, which is a typical travel distance of 10 cm. A typical mean free path for the ejected atoms is of the order of 1 cm. As the ejected atoms scatter many times before reaching the substrate, they will, in general, not be incident normal to the substrate. This creates a conformal coating on the surface of any objects. At the substrate surface the atoms arrange in a structure that depends upon the pressure of the environment, the electrical power used to drive the ionisation, the temperature of the substrate and the target to substrate travel distance.

In the study of Nb, the presence of impurities can either enhance or diminish the superconductivity. The use of high purity materials, clean growing techniques and consistent methods is crucial to having reproducibility. Immediately prior to growth, a low purity (99.99%) Nb target was used to coat the areas of the system that could be, whilst the

substrates remain covered. Nb is an excellent getter and reduces the density of impurity atoms by bonding with those in the residual gas. By sputtering Nb before growing on the substrates, the reactants that may contaminate the sample Nb are removed from the chamber and trapped under subsequent layers that coat the system. Before a high purity (99.999%) Nb target was used to grow samples, this was also sputtered with the substrates covered. This process removes contaminated layers and pre-heats the target material such that it does not begin outgassing during the thin film growth. The final step is to then expose the substrates to the high purity Nb. The thickness is controlled using the exposure time, using rates calculated from thin film thicknesses.

3.1.2 Crystal Growth

Crystal growth by vapour transport uses a temperature driven pressure gradient to diffuse vaporised material from a large bulk source to a substrate, whereupon reaching the surface the atoms arrange according to the most energetically stable configuration. Vapour transport growth was performed to grow sub-micron sized In doped SnTe crystals. To study the superconducting properties, a varied dopant concentration following the formula $Sn_{1-x}In_xTe$, with $0 < x < 0.25$, was used. The following procedures were all designed to have an accurate stoichiometry and the highest possible purity of material in the final product. These are critical to the properties observed and to the formation of the highest quality crystals.

3.1.2.1 Polycrystalline Source

High purity shots of Sn (99.999%), Te (99.9999%) and In (99.99%) were used. The purity of Sn and Te is highly important as these are in a higher proportion in the final source, whereas In makes up 0-10%. 3 mm diameter shots were used as opposed to powder as the surface to volume ratio is small, reducing oxidation and impurities in the mixing processes. To eliminate humidity and oxygen in the environment, a controlled atmosphere N_2 gas flow glove box was used to store and weigh out the materials. The boil off from a 300 L N_2 dewar provided the glove box with a continuous, steady supply of clean N_2 gas. While N_2 may still react with the stored chemicals at elevated temperatures it does not react at room temperature and so is a much cheaper and more readily available alternative to Nobel gasses, such as Ar. Measurements of the shot masses were performed using a balance capable of 1 μg precision, with an accuracy of ~50 μg. For a typical sample size of 1 g, this is an error of 0.006%, which is comparable to the purity of the shots. The design of the glove box is such that material can be passed into and out of a main chamber through a load lock, which is pumped and purged using a rotary pump and the boil off N_2.

Once mixed, the shots of materials were placed in a quartz tube with one end sealed and one end capped with a quick release "Speedivalve". With the shots and N_2 atmosphere sealed in the tube, it was carefully transferred to a gas handling rig. A schematic for the gas handling rig is illustrated in Fig. 3.3. At this point the tube was pumped and purged using a rotary pump and pure Ar (99.9999%) to minimise any impurities and reactive gasses that may be present in the tube. Pump-purging is more effective at impurity removal than pumping to UHV as the inert gas mixes with the contaminant gasses, so that they can be more readily removed. Pumping to UHV could also cause problems when sealing the tubes, as the glass can implode
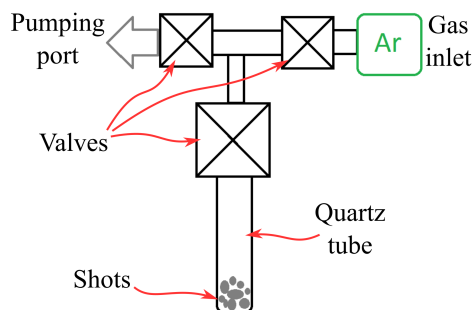
Figure 3.3: Schematic of the gas handling rig, the volume containing the shots was evacuated, and then filled with clean Ar repeatedly, before sealing under vacuum.

if melted under this high stress. The pump-purge process was repeated 6 times and then the tube was sealed at about 7 cm long using an Acetylene-Oxygen blowtorch. This burns at up to 3770 K, enabling the manipulation and sealing of the quartz tube, with a melting point ~2000 K. The result is a sealed quartz ampoule with a stoichiometric mixture of In, Sn and Te in which the residual gas, $P \sim 10^{-2}$ mbar should be predominantly Ar and so inhibit reaction with impurities.

The elemental shots must be well mixed to form homogeneous In-SnTe. Mixing was performed in an electric muffle furnace. The ampoule was placed in the centre of the furnace, where the temperature was observed to be uniform. In-SnTe has a melting point of ~800 °C, so samples were heated to 1000 °C for ~1 week. The natural diffusion of the elements in the viscous liquid phase is not great enough to form a homogeneous mixture and expanding vapours can cause bubbles. To stimulate the mixture the tube was shaken, tapped and upended. The frequency of physical stimulation was initially high (at least three times per day) and gradually reduced so that the tube was undisturbed for the last two days of growth. In this way homogeneous polycrystalline In-SnTe sources were synthesised. Upon cooling, the ingot will contract, allowing it to be removed by opening the tube using a glass cutter. From this point the ingot was vulnerable to oxidation and contamination and so was stored in a glove box.

3.1.2.2   Vapour Transport Growth

Physical VTG uses the diffusion of material from a bulk source to a substrate. A temperature gradient causes preferential diffusion of material, and is thus a key parameter in controlling growth deposition density. A horizontal three zone tube furnace was used, where each zone can be independently controlled, allowing the temperature gradient to be optimised for use. In general, the vapour transport environment can be an Ar flow [78–80, 122] or a pump-purged, sealed tube [84]. This study used the latter design as it is does not require an Ar flow furnace, which has the potential to cause sample contamination. Fig. 3.4 illustrates the VTG arrangement. The transfer rates of material depends upon the saturation vapour pressure, which is 20% higher for In than SnTe and so In may deposit preferentially at a different

temperature/ position than SnTe [123, 124]. In a large temperature gradient, this can result in spatial variations in the dopant levels of deposited material.
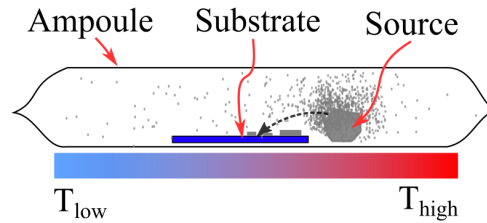
Figure 3.4: Schematic of the VTG in a sealed quartz tube. The source material provides a constant source of vapour, while a thermal gradient drives material onto the substrate where crystals may form.

In preparation for VTG, a clean silicon substrate and an ingot of In-SnTe were inserted into a quartz tube, with one end open. This tube was pump-purged with Ar and sealed under vacuum to form an ampoule. The ampoule was then placed into a three zone furnace. Measurements of the furnace temperature were made using a K-type thermocouple inserted through a narrow aperture in the end of the tube furnace. The temperature gradient found was linear over the range where the tube rested as seen in Fig. 3.5. The temperature and temperature gradient that were observed to yield the most useful samples for this study were 600 °C and 3 °C/cm. Samples grown by this method come in all shapes and sizes, from a few hundred nanometres to a millimetre, depending largely on the growth parameters.
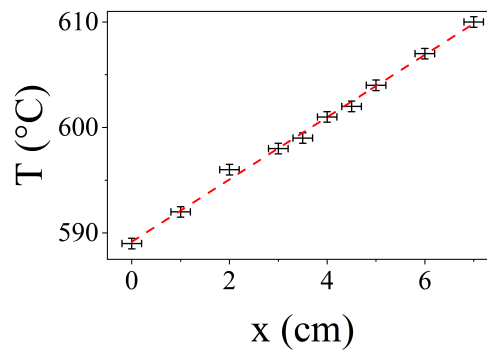
Figure 3.5: The three zone furnace temperature profile used for VTG growths. The temperature gradient measured is (2.95 ± 0.06) °C/cm.

Following a furnace cool, the quartz ampoule was removed and opened. The used polycrystalline ingot was returned to the glove box and the substrate was placed into a sealed pot of clean acetone. The VTG samples were then transferred in acetone to a cleanroom where they were gently cleaned in acetone, with a very short period of gentle ultrasound stimulation, and then rinsed in IPA and blown dry with N_2. The cleaning process of VTG samples must be gentle in order to try and remove glass dust and loose material, without removing the vapour transport grown crystals. The crystals are only weakly bonded to the surface by the van der Waals force. In order to be able to examine the VTG results, a polymer resist layer was spun onto the surface. This layer was purely to protect the Si and In-SnTe

surfaces from damage and contamination. Resist used for nanopatterning was dispersed directly before the lithographic processing.

3.1.2.3 Gold Nanoparticle Catalysts

Au nanoparticles used in this study has diameters of 20 nm or 50 nm. Citrate stabilised GNPs are available suspended in water in high concentration solutions of $\sim 10^{1}2ml^{-}1$. The initial concentration was diluted in pure deionised water to concentrations as low as $10{-}6ml^{-}1$. The diluted GNP solution is prepared freshly before depositing the particles onto a clean substrate. Deposition of the GNPs is as follows. The diluted GNP solution and HCl acid (0.03 M) are dispersed simultaneously onto the substrate, in a ratio 2:1. The acid acts to lower the pH of the GNP solution to 0.01 M, so that the particles can attach to the substrate [82, 125]. A settling time of 15 s is given, then the solution is rinsed away with copious amount of deionised water. The substrate is then blown dry. The concentration of GNPs was adjusted to suit the expected density of VTG crystal growths. GNPs were found to be stable to sonication in IPA and acetone. Before use in the VTG procedure, the GNPs were heated to the growth temperature without a source material, the result of this is discussed in Chapter 5.

3.1.3 Lithography

The lateral dimensions of the Nb nanowires and electrical contacts were all defined by lithography. For ease, where possible optical lithography was used. However, many of the In-SnTe samples required electron beam lithography to create smaller feature sizes. Lift-off lithography is a well established technique used to fabricate on the micro- and nanoscale. In this work a bilayer positive resistive process was used. The resists are chosen such that the top layer is high resolution, only dissolving where exposed, and the bottom layer is low resolution, dissolving when not exposed. This contrast enables the creation of an undercut profile. An undercut allows the creation of thicker features and reduces the creation of unwanted features such as free standing edges and conformal coverage, which can connect the sputtered material between exposed and unexposed areas.

   The basic work flow is illustrated for a blank substrate in Fig. 3.6. Initially, the clean substrate has two resist layers spun and baked onto it. This was then exposed with radiation in the desired pattern. A development process removes the exposed resist and creates the undercut. At a fixed temperature, the development time is the only control of the dissolution of the bottom layer. In Fig. 3.6 (e) and (f) a metal deposition is used to demonstrate the masking properties of the resist, leaving behind the exposed pattern. The following sections give the specific experimental details of the optical and electron beam processes.

3.1.3.1 Optical Lithography

The limit of the resolution in optical lithography is ~ 0.8 μm. For all but the smallest nanowires this is sufficient to make electrical contact and is adequate to define the mask required for the Nb nanowires in this work. An MLA Maskless Aligner, with a 375 nm source was used. Compared to shadow mask aligners, laser writing allows a greater variety of sample designs to be made quickly. This is particularly important when considering that VTG crystals
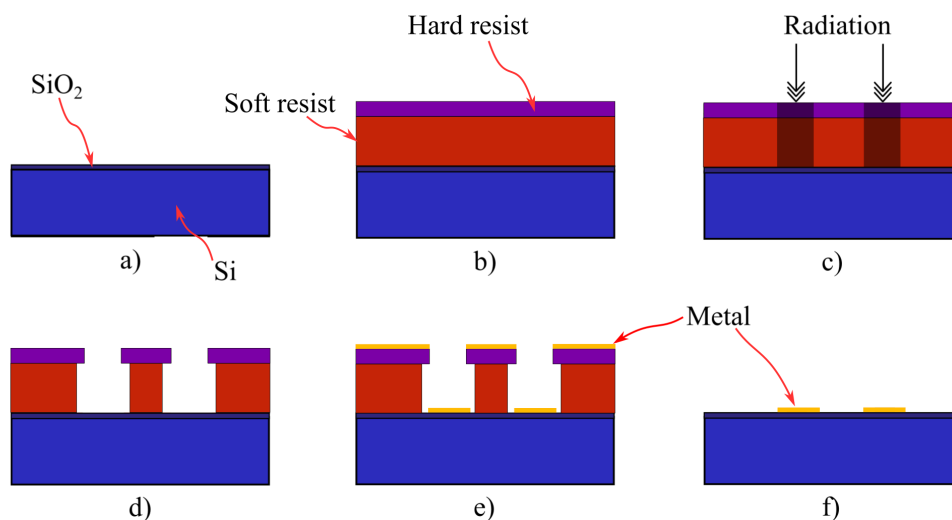
Figure 3.6: Positive resist bilayer processing. a) Clean Si with native oxide b) Two layers of resist are spun and baked. c) Exposure to radiation. d) Development in solution. e) Thin film metal deposition. e) Resist lift-off leaves the desired metallic pattern on the substrate.

form stochastically and often in awkward positions such as near to the substrate edge. A second advantage is that a large variety of samples could be patterned on the same substrate, minimising the number of growths required to obtain a sufficient range to study the desired effects.

Cleaned samples were dehydrated on a hot plate at 180 °C for 2 minutes and then cooled for 1 minute. The lift-off resist (LOR 7B) was then spin coated at 3000 rpm for 40 s and baked on a hot plate at 200 °C for 5 minutes. Once cool, the photo-sensitive resist S1813 was spin coated at 5000 rpm and baked at 115 °C for 1 minute. LOR 7B was chosen specifically as it it creates a uniform and relatively thick, 0.7 μm, layer which helps overcome the thick VTG crystal features. S1813 deposits at a thickness of 1μm at the spin speed used. When exposed, S1813 becomes soluble in the developer MF319, while LOR7B is always soluble. The development time used was 40 s, followed by a thorough rinse in deionised water and a N_2 blow dry. A Nb or Ti/Au thin film was then deposited. Following deposition, lift-off was performed in Microposit Remover 1165 at 75 °C, rinsed in water, Acetone, IPA and then blow dried using N_2. All samples were then covered in a thick layer of resist to stop oxidation and damage, or a bilayer for further processing.

3.1.3.2 Electron-beam Lithography

For all samples where the optical resolution was too coarse, electrical beam lithography (EBL) was used. The main disadvantage of EBL is the time consumption, as the beam has a smaller footprint and requires a longer exposure time at each point. A high dosage, low precision setting can be used to reproduce the same effect as the laser writer but this takes more than ten times longer. Contacts defined using EBL were ~500 nm in width, depending on the requirements of the sample.
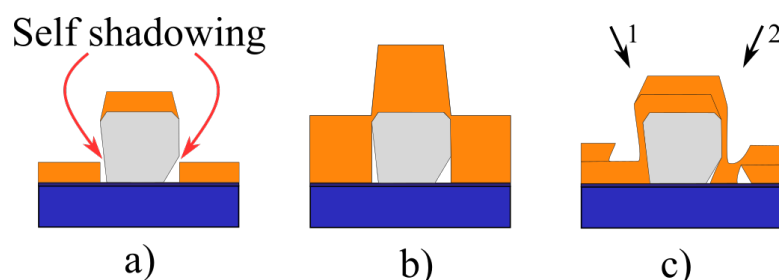
Figure 3.7: Comparison of deposition methods when attempting to make electrical contact to large crystals. a) Self shadowing in straight down deposition causes weakness in the contacts. b) Thicker contacts, can bridge the sample making good electrical contact. Although this requires an undercut layer much thicker than double the crystal thickness. c) Angled deposition creates a continuous layer without requiring very thick contacts. Arrows 1 and 2 show two angles of deposition, typically ~25°, to demonstrate the arrangement required to contact crystal objects.

Similarly to the optical bilayer processing, a harder, high resolution resist and a softer more soluble resist were used. The undercut layer in this case is diluted methyl methacrylate (MMA) EL11 and the top layer is polymethyl methacrylate (PMMA) 950k A4, both spin coated at 4000 rpm for 40s and baked at 180 °C for 5 minutes. Approximate thicknesses for the MMA and PMMA layers are 500 nm and 200 nm respectively. Patterning was performed in a Raith 50 EBL system, with an optimal resolution of ~100 nm, however the undercut bilayer required for this study decreases the resolution to ~400 nm.

3.1.3.3 Metallic contact deposition

Depositing material directly onto nanowires is relatively straightforward when the wires are flat and much thinner than the resist. When the objects to be contacted are thick or have sharp well defined edges, the situation becomes more complex due to self shadowing. The deposited metal can have a gap next to the object, as illustrated in Fig. 3.7 (a). In order to have smoothly connected, low resistance contacts a typical method is to grow contacts thicker than the object, see Fig. 3.7 (b). The thickness of sputter grown Nb was typically less than 100 nm, and so ~200 nm thick metal contacts can be grown to give Ohmic contacts. In the case of In-SnTe, the crystals were often around 300 nm thick, which would require ~400 nm thick contacts. If the total thickness of the contacts plus the sample nears that of the undercut resist layer, the deposited metal layer readily connects below and above the resist, making removal impossible or damaging to the nanowire. Thick contact deposition is illustrated schematically for a thin sample and a thick sample in Fig. 3.8. To overcome the problem of self shadowing, an angled deposition was used to create the contacts. In this way a conformal contact area is created and the Au can be made much thinner, ensuring a working lift-off process, as in Fig. 3.7 (c). The in plane angle of deposition was set using lithographically defined arrows and the tilt angle set using a glass slide. Examples of self shadowing by a thick nanoplate, thick contact deposition, and a nanowire contacted by angled deposition are given in Fig. 3.9.

Contact deposition used both sputter and thermal deposition of Ti/Au. Samples were initially loaded into a sputtering machine, with a base pressure 10^{-7} Torr. Initially, an Ar
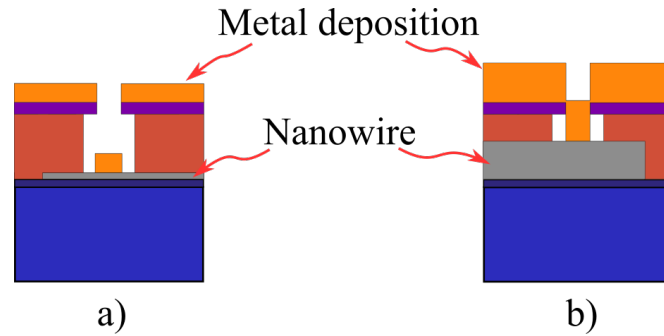
Figure 3.8: Metallic contact deposition on top of a nanowire. a) Thin wire with metal deposition. In this case, contacts can be made thick enough to have good contact. Lift-off is possible. b) Thick wire with metal deposition. In this case, the deposited metal layer is connected. Lift-off is not possible without removing the contacts and/or wire.
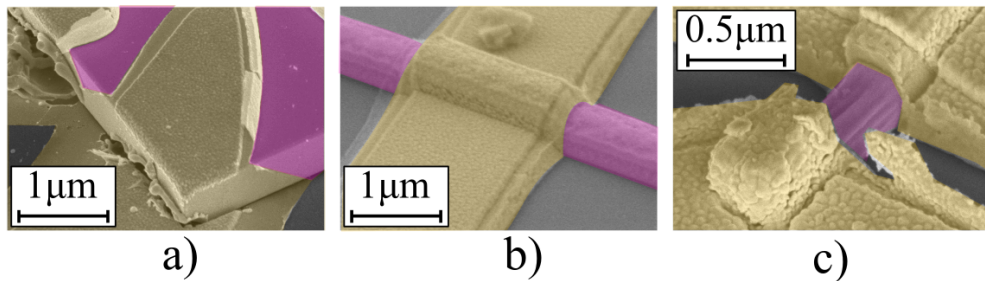
Figure 3.9: Scanning electron microscope images demonstrating three scenarios of deposition to a large crystal. All images are taken at a 45° angle to the normal in order to examine the contact area. a) Straight down thermal deposition. In this image, self-shadowing has weakened the connection at the base of the sample, leading to high resistance contacts which easily melt. b) Thick thermal deposition. In this case, the contact was grown to a similar thickness as the sample, a smooth connection over the wire is formed with low contact resistance. c) Angled deposition. In this image, there are two distinct layers in the contact metal, both deposited at different incident angles. The deposition angles connect to one side each, as per Fig. 3.7 (c). In-SnTe nano-objects highlighted in magenta and the Au electrical contacts are highlighted in yellow.

plasma etch was used to remove contaminants and residual resist, leading to better metallic adhesion and low contact resistance. This step was not included in the original process, but was found necessary to produce low resistance contacts. A 5 nm layer of Ti and Au were sputtered, covering the freshly etched surface of the nanowire with a thin layer of noble metal. This conformal coating prohibits oxidation of the contact areas.

Samples were then transferred to a thermal deposition chamber, with a base pressure of 10^{-6} Torr. Thermal deposition is performed under UHV, and so deposited particles have a long mean free path and are deposited at an incident normal to the base plate, leading to well defined, sharp edged features. Thick contacts were grown with 5 nm of Ti and up to ~100s of nm of Au. It is at this point where for thick crystals, substrates were loaded in with an incident angle of ~25° to the base plate and then rotated to 2 or 3 different positions to deposit Au onto all contact areas, see Fig. 3.7 (c).

3.2 Material and Device Characterisation

3.2.1 X-ray Diffraction

X-ray crystallography is a powerful tool, with a variety of methods available to study the structural characteristics of materials. X-ray diffraction was used in this work to verify that polycrystalline SnTe In-SnTe ingots had formed the correct phase.

X-rays incident on a crystal diffract constructively at incident angles that satisfy Bragg's law:

$$n\lambda = 2d\sin(\theta), \tag{3.1}$$

where n is a positive integer, λ is the wavelength of the x-rays, d is the lattice spacing and θ is the incident angle of the x-ray beam. A measurement schematic is illustrated in Fig. 3.10 (a). A $Cu_{K\alpha}$ source was used with $\lambda = 154$ pm, the lattice spacings that can be determined are of this order. The angle of incidence on the sample is coupled to the angle of a detector, thereby ensuring that the reflected interference is detected. An example spectrum for a bulk SnTe polycrystalline source material is shown in Fig. 3.10 (b). Before x-ray diffraction, bulk samples were polished using emery paper to obtain a flat surface, and alumina paste suspended in a felt pad for a mirror finish. From the spectra we can identify peaks associated with the (200) set of Miller indices for SnTe. Braggs law calculates these angles to be, $2\theta_{(200)} = 28.185°, 2\theta_{(400)} = 58.284°, 2\theta_{(600)} = 93.851°$ for a lattice spacing of d = 0.63268 nm [126]. Gaussian peak fitting gives peak centres, with FWHM errors as $2\theta_{(200)} = (28.18 \pm 0.03)°, 2\theta_{(400)} = (58.30 \pm 0.03)°, 2\theta_{(600)} = (93.89 \pm 0.09)°$. This yields a calculated lattice spacing of $d = (0.6326 \pm 0.0005)nm$, which matches the book value. Using the Debye-Scherrer formula, an estimate of the grain size can be calculated which, for this SnTe ingot, yields a grain size of $(3 \pm 0.6)\mu m$. This large grain size indicates the sample contains large, ordered crystallites, generated during the furnace cooling, solidification process. Due to the polishing required to gain insight into the bulk material, only a few ingots underwent this investigation as it contaminates the ingot irreparably.
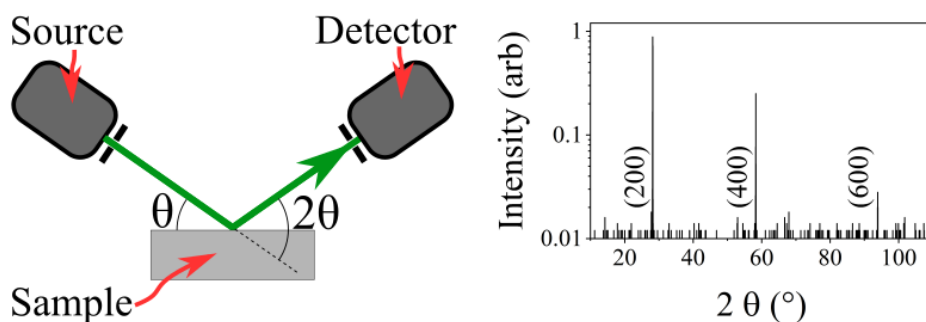
Figure 3.10: X-ray diffraction a) A schematic of an x-ray diffractometer with incident angle and detector angle labelled, θ and 2θ respectively. b) An example of X-ray diffraction from a bulk SnTe polycrystalline sample. The (200) set of Miller indices are observed as indicated.

3.2.2 Helium Flow Cryostat

The sample space in the cryostat used in this work is a variable temperature insert (VTI). This is suspended in a liquid ^{4}He reservoir, which is itself inside a liquid N_2 reservoir. Heat loss is reduced by a high vacuum space between the ^{4}He and N_2 and between the N_2 and the environment. The temperature is controlled in the VTI using a balance of ^{4}He gas flow and a heating element. Gas flow is controlled using a needle valve, which can allow a stable, continuous flow from the ^{4}He reservoir into the VTI. A rotary pump was used to reduce the pressure and continually remove gas. By reducing the pressure with a rotary pump, temperatures below the atmospheric boiling point of ^{4}He can be reached. The temperature range of both cryostats is 1.5 K to 300 K, monitored by one Cernox resistor in the VTI, near the sample and another in thermal connection to the sample through an oxygen-free Cu mount.

The samples sit near the bottom of the VTI on a Cu mount, which is interchangeable depending on the magnetic field orientation(s) required. The sample itself is mounted onto a chip carrier, such that it can be removed without damaging the device. The back of this chip carrier connects via pogo pins to the sample mount, which is connected to a metal tube containing the wiring. This wiring feeds to a port at the top of the cryostat. The tube is made of type 316 stainless steel, which is austenitic and so will not interfere with the magnetic measurements. All electrical connections are in twisted pairs, where positive and negative lines are twisted together to eliminate inductance. Noisy thermometry lines are shielded from the sample measurement lines and have a separate external plug. Signal lines are connected through a Cu loom which is wrapped non-inductively around the inner tube. All of these precautions are in place to reduce interference internally between signal lines and externally with the laboratory environment.

Magnetoresistance measurements make use of superconducting solenoids, situated at the bottom of the liquid ^{4}He bath. At this point it is necessary to distinguish the two types of cryostat used in the following work. The Oxford Instruments cryostat has a single coil solenoid, capable of providing up to 8 T, over the full range of temperatures. This cryostat is illustrated in Fig. 3.12. The Cryogenic cryostat utilises a split pair superconducting magnet, which allows radial probe access, as oppose to the axial access for a single coil. Radial access is beneficial,

as it allows samples to be rotated with respect the magnetic field orientation. However, the maximum field is typically reduced. In this system a maximum field of 3 T can be obtained, over the full temperature range. This cryostat and the rotation mechanism is illustrated in Fig. 3.13. Two distinct rotations were used to investigate the effect of field orientation on the magnetoresistance effects observed, an in plane and a transverse rotation. These are defined as follows: in plane, the applied magnetic field is applied parallel to the substrate, allowing the angle between field and current to be modified; transverse, the applied magnetic field is always perpendicular to the direction of current flow, thus any effects are not from a changing current-field vector (cross) product or projection (dot) product. Two angles, θ and ϕ will be used throughout the work to signify in plane and transverse rotations respectively. These angle definitions are illustrated in Fig. 3.11.
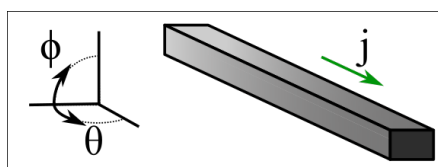
Figure 3.11: Schematic of the the angles θ and ϕ used to represent rotations. θ corresponds to a rotation from in plane, transverse to in plane, longitudinal. ϕ corresponds to a rotation from in plane, transverse to out of plane.

3.2.2.1 Magnetotransport

Determining the resistance of a nanowire requires a four point measurement with approximately one-third spacing between the probes. This spacing minimises spurious effects from local current distributions near to contact points. Low resistance, Ohmic contacts are also required. Contacts were defined using lithography, as discussed previously. Electrical measurements were performed using a Keithley 6221 current source, a Keithley 2182A as a DC voltage probe and a Stanford Research Systems SR830 lock-in amplifier as an AC voltage probe. Lock-ins are incredibly powerful in low noise measurements as they can sample and average rapidly, compared to DC measurements. Lock-in measurements, being in AC, are sensitive to the phase of the complex impedance of a sample, allowing the reconstructing of the out of phase, reactance component. In typical measurements this component is an inductance or capacitance in the circuit. However, there is potential that if some local phenomena is reacting out of phase to the input current source, then a complex impedance is created. Pulsed DC measurements were used to obtain current-voltage relations without heating the sample, as occurs for continuously applied currents. The pulse width used was 1 ms, and the delay between pulses was 100 ms. Current was pulsed in increments, ramping to a positive and negative maximum, and back to zero. While the pulsed IVs contain some features that make hysteresis difficult to observe, there are no obvious heating effects from applied currents. Experiment automation and data capture was performed using Labview software written and maintained by Dr Gavin Burnell. Angular dependent magnetotransport would not be possible without the support of the Electronics workshop.
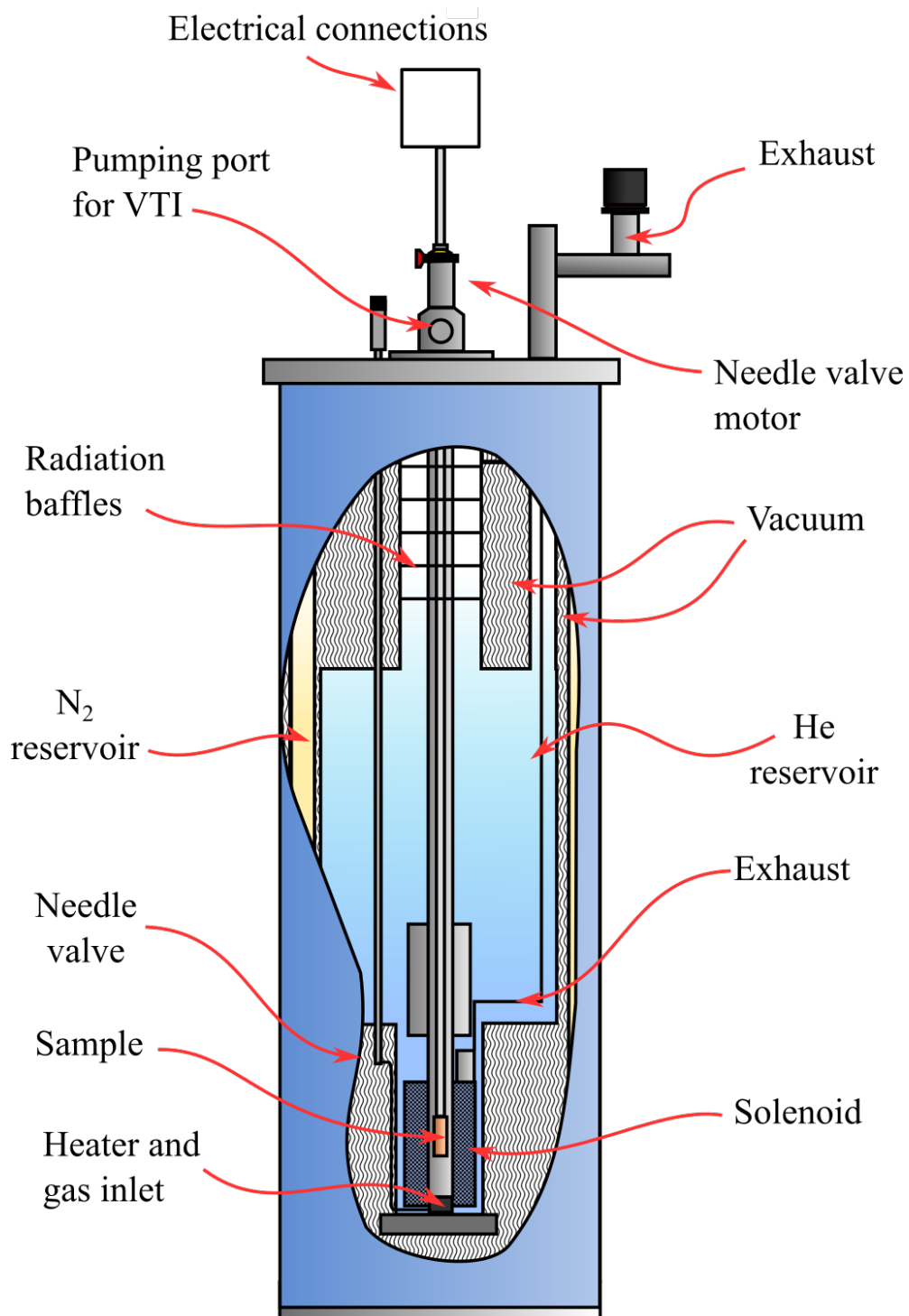
Figure 3.12: Schematic of the Oxford Instruments helium flow cryostat used in this thesis. Maximum magnetic field of 8 T, fixed sample orientation. Adapted from [127].

Electrical connections

Pumping port
for load-lock

Rotating seal

Rotation
motor

Pumping port
for VTI

Gate valve

Needle valve

Exhaust

N_2
reservoir

Vacuum

Needle
valve

^{4}He
reservoir

Exhaust

Sample

Heater and
gas inlet
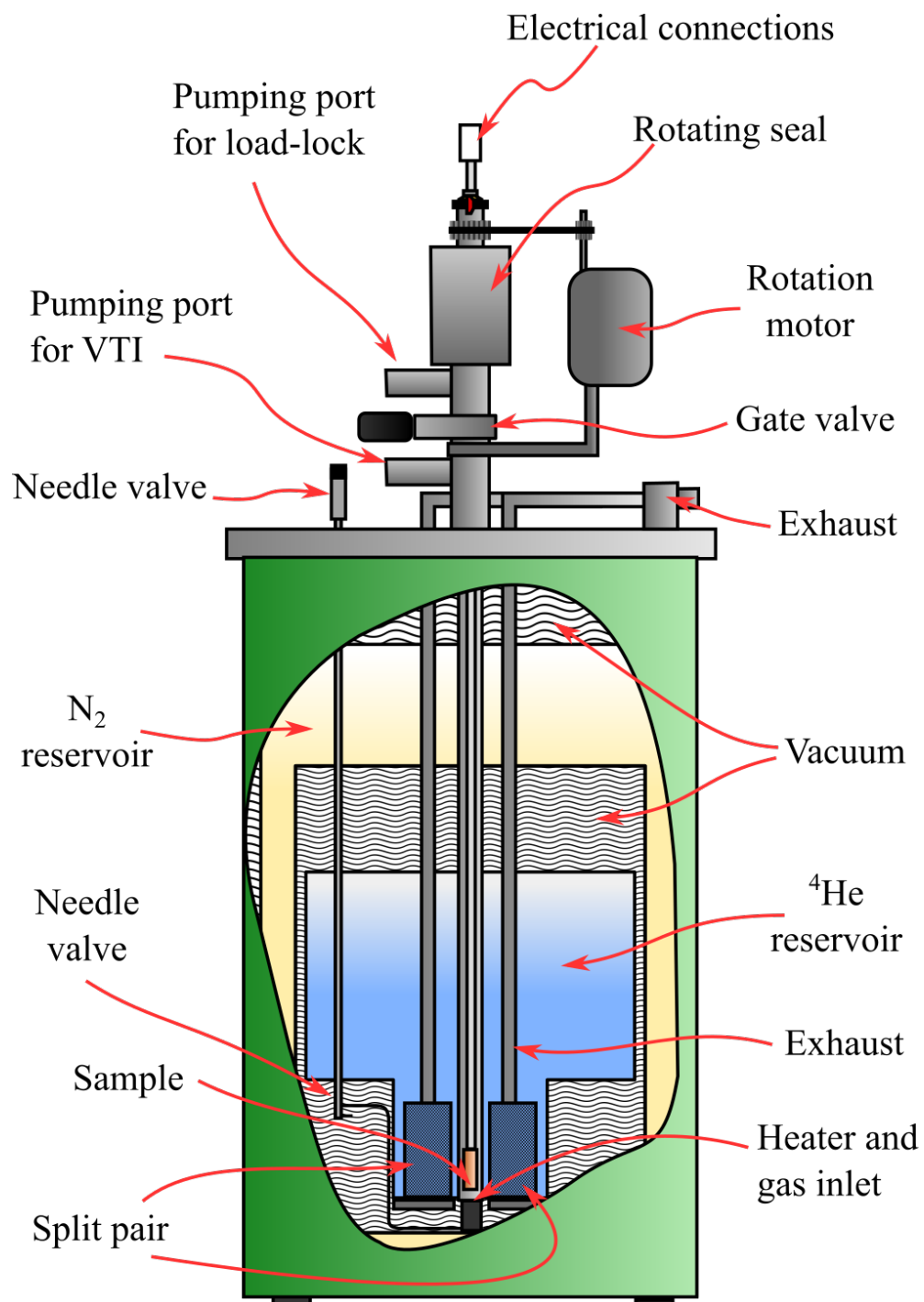
Split pair

Figure 3.13: Schematic of the Cryogenic split pair, helium flow cryostat used in this thesis. Maximum magnetic field of 3T, rotating sample orientation.

3.2.3   Scanning Electron and Electron Dispersive X-ray Microscopy

SEM and EDX utilise the interaction of electrons accelerated at an object and the electrons and ions of the object in a high vacuum environment. Electrons are emitted from a filament and accelerated by a voltage of a few kV and focussed onto an area of a sample. These electrons result in secondary electron emission, x-rays and backscattered electrons.

Standard SEM detects low energy secondary electrons. These are emitted from the surface of the sample, and therefore can be used to construct the topographical information of the sample with a resolution of 1-3 nm. The SEM used to image in this study was equipped with a field emission gun, which in this case was a sharp tungsten wire held at a negative high voltage relative to an electrode. Electrons are emitted from the tungsten wire tip by field emission, which provides a smaller diameter, higher intensity, and more coherent beam than filamentary electron guns. A rotating, tilting sample stage was used in the SEM, to allow measurements at an angle. The sample thickness could be measured this way. Also, in certain cases, the top down SEM topography images could be misleading. The main use of SEM in this study is to examine the topography of lithographically defined samples and contacts, VTG crystals, and GNPs.

EDX microscopy utilises the characteristic x-rays emitted by an element. A beam of high energy electrons excites ground state electrons in the sample elements. The ground state is subsequently filled by electrons from a higher energy. These transitions release discrete energy, equal to the difference in energy levels, in the form of characteristic x-ray photons. EDX provides a qualitative measure of the elements present. The x-ray intensity can be calibrated to give a quantitative measurement, using known test samples. EDX is a surface probe, as injected electrons are rapidly absorbed by the sample. The depth of the electron travel can be adjusted using the electron accelerating voltage. A typical depth penetration of an EDX probe is ~1 μm. For the samples studied here this is sufficient to gain all of the information required. Laterally, the technique is limited to a resolution of ~1 μm^2, however more precise elemental maps can be interpreted from dense raster scans. The EDX-SEM used to create elemental spectra and maps was equipped with a field emission gun. The sole use of the EDX-SEM in this work was to obtain the qualitative elemental composition of In-SnTe crystals grown with GNP catalysts.

CHAPTER 4

Oscillatory Magnetoresistance in Nb Nanowires

In this chapter, OMR exhibited by sputter grown Nb nanowires is examined. Firstly, the quality and general characteristics of the Nb material and the fabrication methods used are shown, with observations from both the normal state and the superconducting state. The novel advances come in the study of the OMR effect. Nb nanowires are an ideal system to study OMR. Firstly, high quality, controlled growths can be performed. Secondly, the material is well studied, and so observations can be supported by general knowledge. Thirdly, previous experimental studies and simulations of OMR have used Nb, allowing comparisons to be made.

In this thesis, a new analysis method for the OMR effect is presented. The technique treats the OMR, not as a sinusoidal oscillation, but as a series of resistive events. It is found that this fits to all of the data remarkably well. From this new analysis, several new parameters are defined to enable general discussion of OMR. While the OMR effect is most readily observed in AC MR measurements, DC, and pulsed IV measurements provide complimentary and vital information to probe the physical nature of the OMR effect.

Using the standard AC MR measurements, the dependency on environmental parameters, mainly sample temperature, AC amplitude and AC frequency, is used to elucidate general characteristics of the OMR effect. This includes limiting cases where the effect is diminished. Both a reactance component to the AC OMR impedance and a negative resistance in the DC OMR are observed, giving new insights into the complex state of the system during the superconducting transition in a magnetic field.

Previous explanations for OMR are discussed relative to the evidence presented, particularly with relation to the period of the oscillations and the orientation of the applied magnetic field. Both of which are key parameters in most explanations. The evidence appears to align with a periodic vortex motion induced OMR, with the period predominantly controlled by the pinning landscape.

This chapter begins with an overview of the general properties of the nanowires.

4.1 Nb Nanowire Fabrication

All samples discussed in this chapter were grown by a DC magnetron sputtering process, described in Chapter 3. Lateral dimensions were defined using bilayer optical lithography with lengths of 7 to 33 μm, and widths of 0.8 to 30 μm. Nanowire thickness was controlled using the length of time of sputter deposition, with predetermined deposition rates, measured using x-ray reflectivity of calibration thin films. Thicknesses were chosen to be between 2 and 6 coherence lengths, with an estimated ξ = 10 nm. At the lower limit, this will largely suppress the superconductivity, and so resistive effects are amplified in the measured signal. This follows from the definition of the coherence length as the minimum size of perturbations. ~6 coherence lengths is effectively a bulk sample and so the magnetoresistance superconducting transition should be monotonic and sharp.

An example of a Nb nanowire with detailed views of the contact and wire deposition is shown in Fig. 4.1. The sputtered Nb has some edge features typical of sputtering, material spreads under the undercut resist giving a tapered edge. This is in stark contrast to the thermally deposited Ti/Au in this image. The Nb structure is otherwise well defined. Contacts are placed at varying intervals in the device design so as to be able to test the effect of varying the length between contacts.
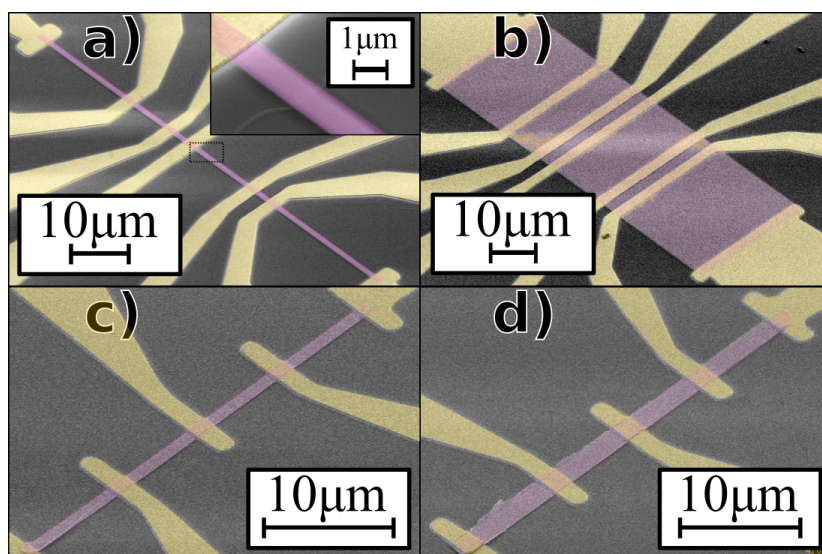
Figure 4.1: Detailed SEM of a sputter grown Nb nanowire. Thickness = 20 nm, width = 0.8 μm, total length = 80 μm, and the maximum length between voltage contacts = 30 μm. The contact is Ti (5 nm) and Au (5 nm) grown by sputter deposition and Ti (5 nm) and Au (100 nm) grown by thermal deposition. Nb nanowires highlighted in magenta and the Au electrical contacts are highlighted in yellow.

A variety of Nb nanowires were grown in the project with a varied width, length and thickness. A selection of different nanowires grown is shown in Fig. 4.2. In this study, several lithographic pattern designs have been used. The physical limits of the observed OMR effect are not well studied in literature. As a secondary investigation, a few different sizes of samples were used to partially investigate the spatial limits of the OMR effect. While far from comprehensive, there are a few notable trends.

4.2 Nb Nanowire Basic Characterisation

Several readily obtained parameters can be used to ascertain the quality of sputter grown samples in the normal and superconducting state. Resistivity and the RRR ratio, RRR = R(300 K)/ R(10 K) give information about the scattering of normal state electrons in the samples. Normal electron scattering influences the superconducting coherence length through Eq. 2.7. The resistivity of a metal at room temperature is dominated by electron-phonon scattering. This freezes out at low temperature, and the remaining residual resistivity is caused by intrinsic scattering from defects, impurities, and grain boundaries. Sample size affects the normal state transport when the dimensions are comparable to, or smaller than, the intrinsic mean free path of the electrons. An increase in surface scattering effectively shortens the mean free path. The RRR is a powerful measure as it encompasses a variety of sample dependent information in one index. The higher the RRR, the cleaner and more defect free a sample is. In bulk and thin film Nb samples, the RRR can be 100-1000. Patterning material into nanowires dramatically increases the effect of intrinsic scattering, reducing the expected
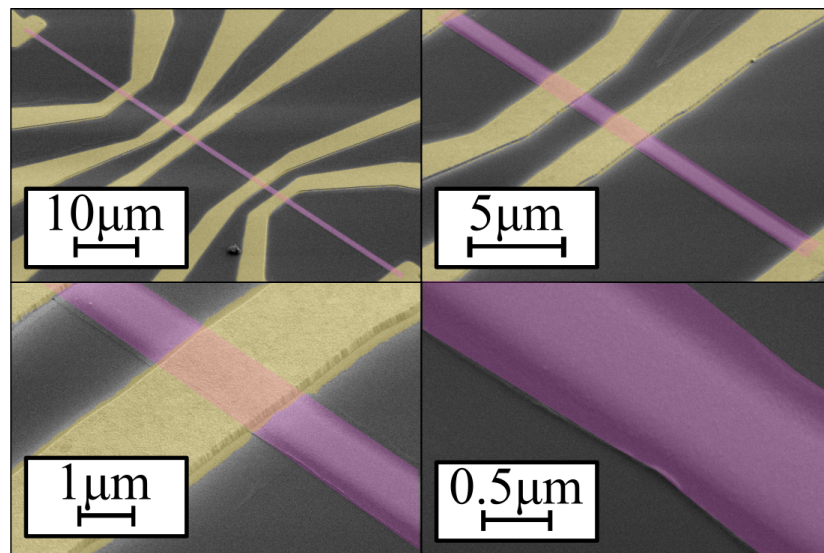
Figure 4.2: Four examples of Nb nanowires. a) Thickness = 20 nm, width = 0.8 μm, total length = 80 μm, maximum length between voltage contacts = 30 μm. b) Thickness = 20 nm, width = 30 μm, total length = 80 μm, maximum length between voltage contacts = 30 μm. c) Thickness = 60 nm, width = 1.0 μm, total length = 37 μm, maximum length between voltage contacts = 16 μm. d) Thickness = 60 nm, width = 2 μm, total length = 37 μm, maximum length between voltage contacts = 16 μm. Nb nanowires highlighted in magenta and the Au electrical contacts are highlighted in yellow.
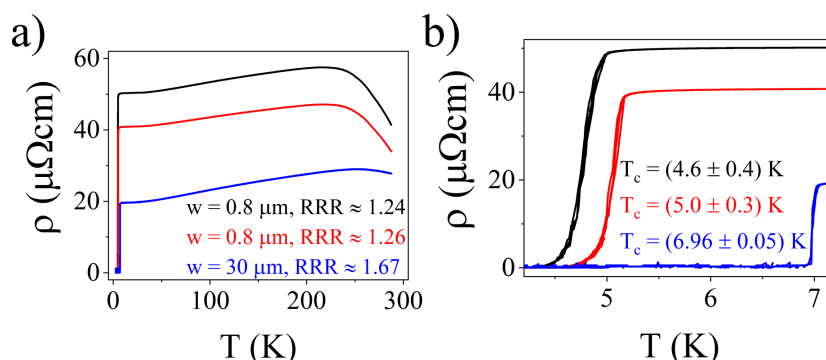
Figure 4.3: Resistance as a function of temperature for a selection of three nanowires. a) The full temperature range. b) A magnified view of the superconducting transition. Note the high temperature decrease in resistance is due to the silicon substrate. The resistance measurement was performed using a lock-in AC technique. Measurement frequency = 773.7 Hz, current amplitude = 2 μA. Temperature was swept in both a positive and negative direction. Hysteresis was not observed in the measurement due to the slow sweep rate, this is apparent in the data.

RRR values by two orders of magnitude. As the Nb is sputtered, it is polycrystalline, which also increases the intrinsic scattering.

Near to room temperature, the Si substrate reduces the measured sample resistance. To overcome this, RRR values are extrapolated from the linear regime of resistance as a function of temperature (50~150 K). This follows from the fact that the intrinsic resistance of Nb is linear above ~50 K and the Si conductivity is negligible below 150 K. An example of resistance as a function of temperature is given for three nanowires in Fig. 4.3 (a). The samples shown here are nanowires (width = 0.8 μm) or nanoplates (width = 30 μm), all patterned and grown on the same substrate. The intrinsic material properties should be nominally identical. The noteworthy features are: the non-linear resistance due to the substrate above 200 K, the different resistivity values but similar RRR values of nominally identical samples, and the halving of the resistivity and increase in RRR between the sample widths 0.8 μm and 30 μm.

Fig. 4.3 (b) shows a maximised view of the transition for the three nanowires shown in Fig. 4.3 (a). Throughout this work critical temperatures are quoted as the temperature at which the resistivity is half of the normal state resistivity, i.e. $T_c = T(R = 0.5R_N)$. The error in T_c is derived from the width of the transition, $2\delta(T_c) = T(R = 0.9R_N) - T(R = 0.1R_N)$. The most prominent features of these three samples are the suppression of T_c and the increased transition width for smaller A_{CSA} nanowires. Where the area, A_{CSA} = thickness × width. Sharp superconducting transitions occur in samples where the path between electrodes is homogeneous relative to the dimensions of the sample, such that there is a path through the superconductor that transitions simultaneously. Conversely, a broad superconducting transition indicates that during the transition the material separates into islands of superconducting and normal material, giving a slower rate of change of resistance in the transition with temperature.

In order to understand the effect of different dimensions on the OMR in Nb nanowires, the effect of the dimensions on the general properties must be discussed. According to the Drude
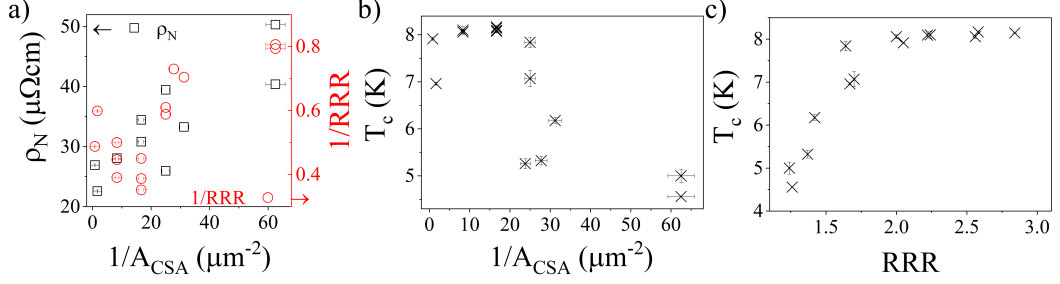
Figure 4.4: Nb nanowire normal state and superconducting characteristics. a) Normal state resistivity and inverse of the RRR as a function of the inverse of the wire cross sectional area. b) Critical temperature is dependent upon the thickness and width, which are both included in A_{CSA}. c) The critical temperature and RRR are strongly correlated, both are highly dependent on the material quality and the size of the sample.

model, the resistivity depends upon the mean free path through the equation, $\rho = \frac{m_e v_F}{n e^2 l}$, where we have used the Fermi velocity, v_F, the density of electrons, n, and the mean free path, l. The Fuchs-Sondheimer effect is a reduction in the mean free path due to a reduced sample size. This is more profound when both the width and the thickness of a wire are $\lesssim 1 \mu m$ [128, 129]. A shorter mean free path increases the resistivity. To enable comparisons across a range of samples with thickness and width varied, the A_{CSA} has been used as a measure to encompass both dimensions. In Fig. 4.4, reasonable correlations can be seen between A_{CSA}, ρ_N, RRR and T_c. Where ρ_N is the normal state resistivity. The reason the correlation is not stronger is because the width is an order of magnitude larger than the thickness. The dependency of the mean free path on width is less than the dependency on thickness. A more indicative comparison can be made directly between the RRR and T_c. The two are clearly dependent on the same parameters. Nb T_cs have been shown to be related to the resistivity by Testardi and Mattheiss [130]. With this as an example, we can assume that the RRR and T_c are related without the need to include the size or measures of sample quality, as both are encapsulated in the parameter RRR.

The coherence length was calculated experimentally using the definition of the upper critical field in Eq. 2.21 and the Werthamer, Helfand and Hohenberg equation for experimentally determining $H_{c2}(0)$ [131, 132]:

$$H_{c2}(0) = -0.693 \frac{dH_{c2}}{dT}\bigg|_{T_c} T_c, \tag{4.1}$$

where $\mu_0 H_{c2}$ is taken as the applied magnetic field when the resistivity is 99% of the normal state resistivity. $\mu_0 H_{c2}$ is temperature dependent.

Values of the coherence length determined using the upper critical field are shown against the normal state electron mean free path, l, in Fig. 4.5. The observation shows that the coherence length is suppressed from the bulk value of 39 nm [35], due to the low dimensions of the nanowires. The variation in l has no influence on ξ. The average value of ξ measured is $\xi = (11 \pm 1)$ nm. Coherence length suppression occurs when the mean free path is smaller than the bulk coherence length, the so called dirty limit. For Nb, l was estimated using the normal
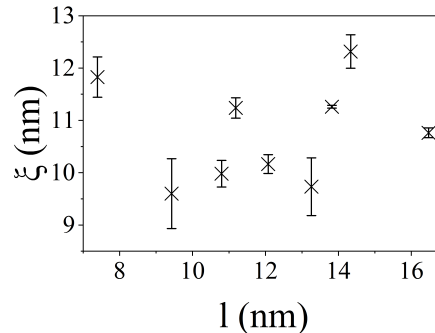
Figure 4.5: The coherence length vs mean free path for a selection of Nb nanowires. Coherence length estimated using the Werthamer, Helfand and Hohenberg equation and the definition of $\mu_0 H_{c2}$. There is no clear correlation, suggesting that for the range of samples measured the coherence length is nominally unchanging.

state resistivity, ρ_N. Mayadas *et al.* [133] generated the relationship $\rho_N(\mu\Omega cm)l(nm) = 3.72 \times 10^{-7}\mu\Omega cm^2$ for Nb thin films. This relies on the assumption that the band structure is close to that of bulk Nb and has been used successfully several times [134–136]. Resistivity from transport measurements gives the upper and lower limit of l as 7 nm and 18 nm which are for the smallest and largest A_{CSA} wires respectively. This value is significantly smaller than the bulk coherence length, therefore we can confirm the dirty limit is appropriate for all of the samples studied.

4.3 Oscillatory Magnetoresistance

To quantify information from the MR data, certain parameters have to be used. The most straightforward are the periodicity and the resistivity of the peaks, however these are not trivial to define. One could use the turning point of the raw data to define the peak position, and use the resistivity to define the peak resistance. However, this assumes that the resistance of the sample is purely originating from the OMR, which may not be the case. We have found that the OMR is poorly defined by oscillatory functions, and better defined by a series of normal distribution functions superimposed onto a monotonic background created by interpolating between minima in resistivity. In certain measurements a background can be defined using measurements where the OMR is suppressed, this is indicated when used. For simplicity we continue to use the term OMR, which is ubiquitous in literature, to describe the effect. A more appropriate description may be periodic resistance events in the superconducting magnetoresistance transition. As we have used an unconventional analysis technique, care will be taken to define the parameters presented and how they are used to quantify and compare OMR signals. Several measurement techniques are employed throughout this section, the most common being AC MR. AC transport measurements were used as they are low noise and have a high data acquisition rate, other methods used include DC MR and pulsed IVs, the merits of which are explained where the data is analysed.

As we shall see later in this section, the background is dependent on the measurement settings, as such cross comparison between datasets is approached with care. Through simulation [19], it has been shown that a monotonic background can originate from the same mechanism as the OMR. The OMR and background smoothly connect as we shall observe, which further complicates the task of distinguishing the effect from a background MR.

To add context to the analysis, a selection of OMR observations, through lock-in AC resistance measurements are shown in Fig. 4.6. The OMR results are shown in three stages: the full transition, a magnified view of the peaks in resistance, and the data after background subtraction with the associated Gaussian peak fits. To assist the reader, the remainder of this section describes detailed steps of the analysis, which is then used to generate characteristic OMR parameters as defined in the next section.

Between Fig. 4.6 (a) and (b) the OMR is highlighted at the onset of resistivity and a smooth background is generated. For this temperature varied dataset, the background is created using a smooth interpolation between minima of resistance. The background is made to be monotonic and smoothly connect to the high magnetic field superconducting transition, where OMR is not observable. Each measurement has a separate background resistance to conform to this later point. After subtraction the result should be dominated by the OMR signal only. Panel (c) shows an example of the fitting done throughout this study, for the data in (b) at 2.9 K. The fit shown is a series of Gaussian distributions either centred at a local maxima, or centred at positions that allow the fit to simulate the curve where local maxima are not available. The later kind tend to only occur at high magnetic fields. The OMR signal, $\Delta\rho$, and the sum over these Gaussian fits match well. The closeness of the fitting, and the clear incompatibility of the data to be fit with a standard oscillatory function shows that this OMR effect can be considered to be caused by a series of events, which occur over a range of magnetic fields.

An alternative analysis is shown for a dataset where the current is varied in Fig. 4.7. In this case the OMR signal is clear from the onset of resistivity to the fully normal state. Due to this, the background is taken as the lowest current value, $I_{ac} = 5\mu A$, where the resistance has no oscillations. This technique works in the ideal case, where the only additional resistance is from the OMR signal. As can be seen from the fitting in Fig 4.7 (c), $\Delta\rho$ matches well to the sum of the Gaussian fit with this subtraction method. This second method encompasses all the additional resistance due to an increased current, but can still be described by the Gaussian peak fits, this suggests that the OMR is responsible for all of the $\Delta\rho$. This analysis technique is only possible when the variable range probed has some limit that lacks an OMR signal. This is only observed at low currents or high frequencies. Consequently, measurements such as the temperature dependency of OMR cannot have an experimentally determined background and require the method previously described, where a smooth interpolation to resistance minima is used.

4.3.1 Oscillatory Magnetoresistance Characterisation

To describe Gaussian fits to the AC OMR signal, several measures of the OMR effect will be defined. The peak field, $\mu_0 H_{Peak}$, defined as the centre of the Gaussian distribution contains information about the amount of energy required to drive the resistive events. In a vortex motion induced OMR picture, this is related to the Lorentz force and the strength of the Meissner screening. The peak order, n, is an integer counting peaks in order of increasing
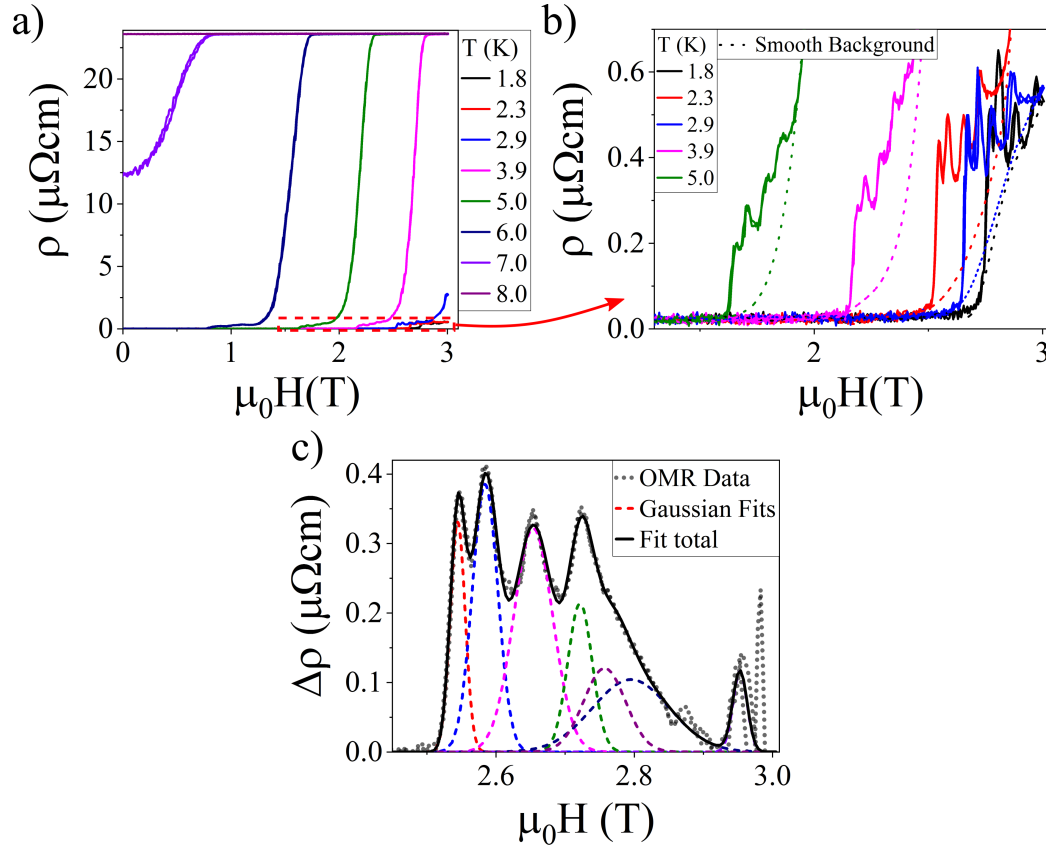
Figure 4.6: Examples of Gaussian Fitting to the OMR signal after a background subtraction. Temperature dependence for a Nb nanowire in the longitudinal orientation, with the current and magnetic field parallel. Measurement frequency = 773.7 Hz, current amplitude = 2 μA. Thickness = 40 nm, width = 1 μm, length = 7.4 μm, T_c = (7.1 ± 0.3) K. a) MR data. b) A focus on the OMR effect at the onset of resistivity, corresponding to the red square highlighted in (a). The background resistance to be subtracted from the MR is shown for each temperature using a dotted line of matching colour. c) An example of Gaussian fitting to the MR at 2.9 K, after background subtraction. After a smooth background subtraction, the data (grey dotted line) fits well to the sum of series of Gaussian distributions (black solid line). Individual peaks are shown in coloured dashed lines.
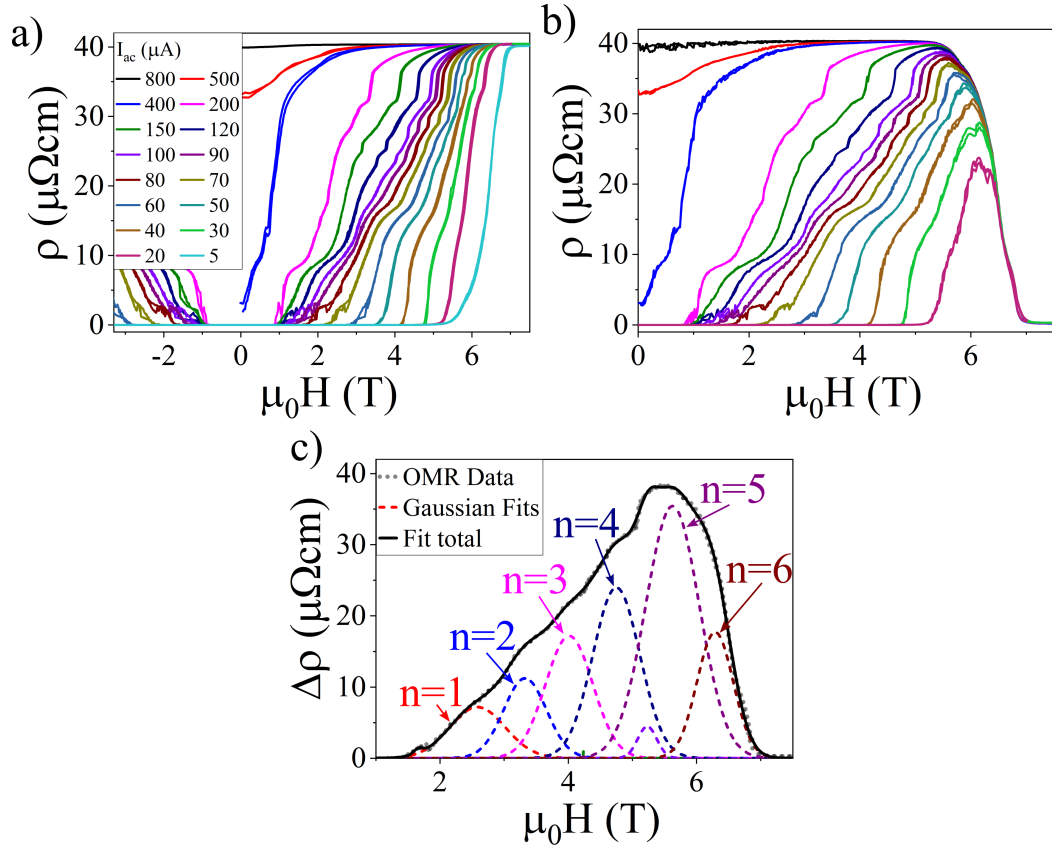
Figure 4.7: Examples of Gaussian Fitting to the OMR signal after a background subtraction. Applied AC current amplitude dependence for a Nb nanowire in the transverse, in plane orientation. Measurement frequency = 773.7 Hz, temperature is 1.6 K. Thickness = 20 nm, width = 0.8 μm, length = 33 μm, T_c = (3.8 ± 0.6) K. a) MR in the transverse orientation, showing the full transition to normal state at a series of applied AC currents. b) Data from (a) with the lowest current data subtracted, taken here as the best approximation to a background. c) An example of Gaussian fitting to the 90 μA MR, after background subtraction. After a smooth background subtraction, the data (grey dotted line) fits well to the sum of series of Gaussian distributions (black solid line). Individual peaks are shown in coloured dashed lines. The peak order, n, is labelled to clarify the definition.
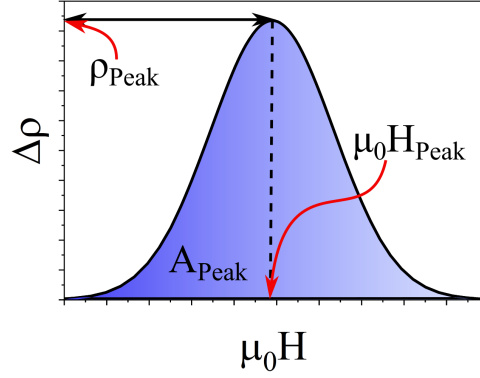
Figure 4.8: An example Gaussian peak, with the associated definitions for the OMR fitting. $\mu_0 H_{Peak}$ is the magnetic field at the centre of the peak. ρ_{Peak} is the maximum resistivity of each peak. A_{Peak} is the area integral under the peak, shown in blue.

$\mu_0 H_{Peak}$, shown for the example fit in Fig. 4.6 (f). The peak resistivity, ρ_{Peak}, or peak resistance, R_{Peak}, contains information about the energy dissipated by the system due to the resistive events. The peak area, A_{Peak}, or total OMR integral, $\int \rho \, dH$, gives a measure of the total energy lost due to OMR in the superconducting transition. Where $\int \rho \, dH$ is effectively a sum over all A_{Peak}. The definitions of $\mu_0 H_{Peak}$, ρ_{Peak}, and A_{Peak} are shown for an example Gaussian distribution in Fig. 4.8. Throughout the next section we will use these newly defined parameters to discuss trends and relationships, and gain understanding into the mechanisms behind the OMR effect.

4.3.1.1 Periodicity

Many of the possible mechanisms for an OMR effect have a distinct periodicity. Here we discuss the periodicity of the effect in Nb nanowires and how this effect changes with respect to the temperature (T), AC current amplitude (I_{ac}), and AC frequency (f_{ac}). Fig. 4.9, 4.10, and 4.11, panels (a-d) are concerned with several measures of the periodic nature of the OMR effect. (a) panels show the peak field as a function of an environmental variable. (b) panels show the peak field as a function of the peak order with the gradient of a linear fit in the inset. This gradient is a measure of the period, as it gives a measure of the average period weighted by the errors in peak field. If the average period was dependent on an experimental parameter, this would be the clearest way to observe a trend. Panels (c) and (d) are concerned with the step size between adjacent peaks, which will be discussed later.

The temperature has a clear effect on $\mu_0 H_{Peak}$. $\mu_0 H_{c2}$ is also shown in the figure for temperatures 4 K to 6 K. It is clear that the overall trend in $\mu_0 H_{Peak}$ is due to the general suppression of superconductivity by the temperature, and not due to some OMR specific mechanism. To further examine the effect of temperature on the OMR peak field, $\mu_0 H_{Peak}$ is shown in Fig. 4.9 (b) against the peak order. In the inset of Fig. 4.9 (b), over the temperature range measured, the average period is shown to be approximately constant. 4 out of 5 points fall within the same error, and the 2.9 K data point is only 15% higher. Given that the 2.9 K gradient has the most peaks, it could be the case that the highest n oscillation is at a

spuriously higher $\mu_0 H_{Peak}$, skewing this gradient above the rest. The OMR at 2.9 K has more observed oscillations. The lower temperatures may have more oscillations, but are limited by the 3 T range of the magnetic field. At higher temperatures the background dominates the resistance, distorting or hiding OMR peaks. These two effects cause a maximum in peak number for 2.9 K, which is not related to the intrinsic OMR effect.

The period for this sample is approximately 70 mT. In terms of Little-Parks and SQUID OMR origins, this period equates to flux quanta passing through an area of $2.9 \times 10^{-14} m^2$. This value is very similar to the area of the end face of the sample, $4 \times 10^{-14} m^2$. This would suggest that the sample is acting as a superconducting cylinder, with only a very thin shell of superconductivity. This explanation is clearly spurious. Additionally, the OMR period is observed to be independent of temperature, which in these OMR explanations would require the normal cylindrical core to have a fixed area in the range $0.2 T_c < T < 0.75 T_c$. It is highly unlikely that a normal core would not change size over this temperature range.

Superconducting properties are highly dependent upon the temperature, however it appears that as the temperature is raised the OMR is simply shifted to lower magnetic fields and eventually dominated by the background monotonic resistance. The periodic vortex motion model does not expect to have a change in $\mu_0 H_{Peak}$, but does not consider the reduction of $\mu_0 H_{c2}$ and the early penetration of flux at higher temperatures. It is reasonable to assume that the vortex motion model applies, but as the thermodynamic fields are reduced, the fields required to cause the OMR events are reduced equally, but the OMR period remains reasonably stable.

Generally, a higher AC current amplitude has the general effect of reducing the peak field, as shown in Fig. 4.10 (a). This may seem to oppose the argument used in the vortex motion model, that a higher local current density impedes vortex entry and flow. However, a larger transport current would reduce the magnetic field required to cause resistive events. Considering the Lorentz force required to cause resistive hopping of vortices, a higher transport current would require a lower magnetic field to generate the same force on the vortices. The sudden drop in $\mu_0 H_{Peak}$ for 80 and 90 μA is due to a peak that became pronounced over this current range, signifying a period where the energy barrier for an event at that field was minimised. Other explanations for the OMR effect should not have a smooth reduction in the peak fields, having either a periodic dependency on the transport current or requiring quantised flux and thus quantised field values. Fig. 4.10 shows $\mu_0 H_{Peak}$, vs the peak order n. The data fits well to linear fits, showing that for this OMR range the period is approximately constant. In the inset of Fig. 4.10 (b), over the current range probed, the average period is modulated drastically and non-monotonically. In the SQUID or Little-Parks based OMR origins, the normal state cylinders, which form the SQUID loops, could only increase in area with increased current. The area will increase as the superconductivity is suppressed at high transport current densities. At the onset of the OMR effect from 20 - 40 μA, the period dramatically increases, and so this effect cannot be explained by multiply connected SQUID loops or Little-Parks cylinders. Taking the period to be 0.6 T, this equates to flux quanta in an area of $3.3 \times 10^{-14} m^2$. With the magnetic field applied in the transverse orientation, even assuming a hole could be formed in the superconductor at the limit of the 20 nm thickness of the sample, this would mean the width of the hole was 1.7 μm, this is an unreasonable shape for the proposed SQUID or Little-Parks normal core.
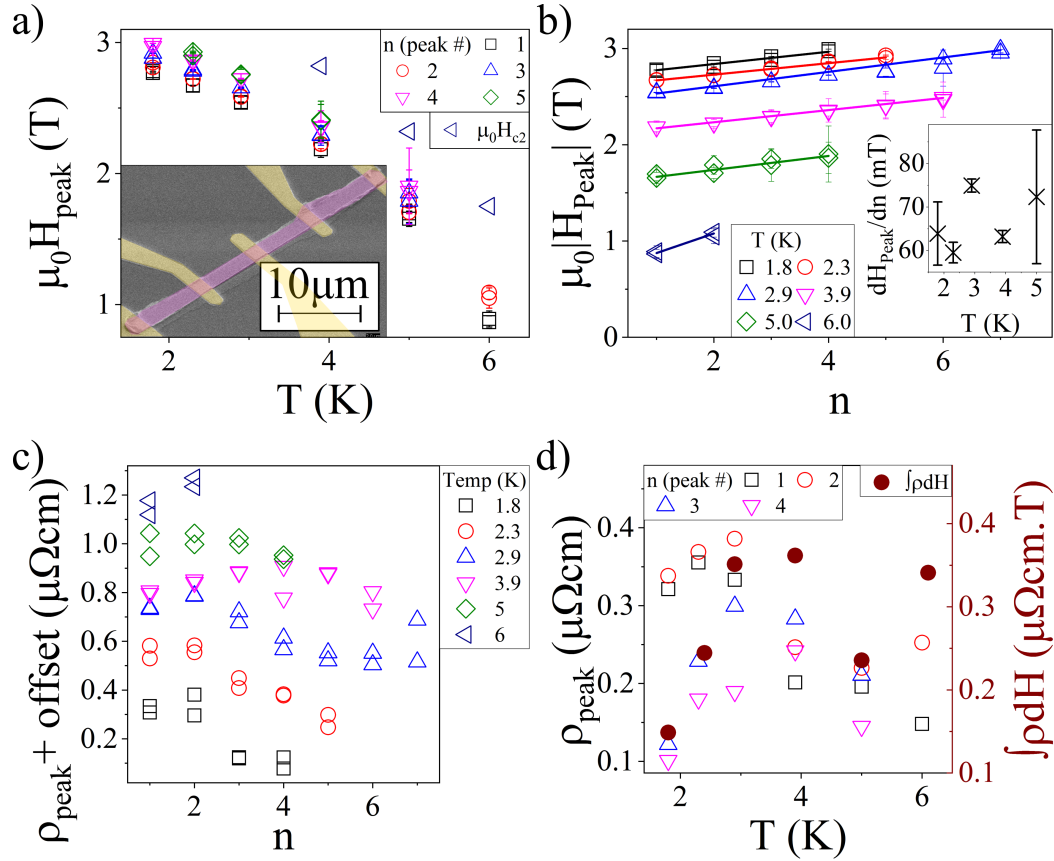
Figure 4.9: Temperature dependence of the OMR fit parameters for a Nb nanowire in the longitudinal orientation. Measurement frequency = 773.7 Hz. Current amplitude = 2 μA. Thickness = 40 nm, width = 1 μm, length = 7.4 μm, T_c = (7.1 ± 0.3) K. a) The centre field of each Gaussian peak fit vs temperature. Included for 4-6 K is the upper critical field, $\mu_0 H_{c2}$. The inset shows an SEM image of the nanowire used in this study, coloured to distinguish Nb and Au. b) The centre peak field of each Gaussian fit vs peak order, as defined in Fig. 4.6. Inset: The gradient of the linear fits vs sample temperature. c) The maximum resistance in each Gaussian event vs peak order. A constant offset of 0.2 $\mu\Omega cm$ separates the temperatures for clarity. d) The maximum resistance (open symbols, left y-axis) in each Gaussian event vs temperature, right hand axis shows the total integrated OMR (solid circles). During analysis the subtracted background resistance was taken as a smooth spline to points of minimum resistance.

4. OSCILLATORY MAGNETORESISTANCE IN NB NANOWIRES

At very low currents, the OMR effect is not observed. In the vortex motion model, this would be due to the current amplitude not providing a large enough Lorentz force, resulting in pinned, unmoving vortices. The average period increases with current to a maximum between 40 and 60 μA, and then reduces before the superconductivity is destroyed. These sections appear similar on the plot of $\mu_0 H_{Peak}$ vs n, as if there are three phases of resistive behaviour. In the first section, with increasing average period w.r.t. current amplitude, the resistive events require large magnetic fields and so appear close together at fields near to $\mu_0 H_{c2}$. This low current data smoothly connects to currents so low that the resistive events merge to become a monotonic background. At the mid-range currents, the balance is such that the currents applied weaken the barriers to vortex motion and the field strengths required are spread out. At the higher range of currents, the transport current in conjunction with the applied magnetic field are capable of overcoming vortex barriers at low fields, where vortex crossings occur up until $\mu_0 H_{c2}$. In this higher current regime, the vortices are not as strictly constrained and so motion can occur after a smaller interval in field between resistive events. At very high AC currents, the sample will experience localised Joule heating and become normal. The temperature is observed not to have a strong effect on the average periodicity of the OMR, and so the effect of heating on this measure is assumed to be negligible.

Fig. 4.11 (a) shows that $\mu_0 H_{Peak}$ has a small dependency on the frequency over the range probed. At the upper frequency range, there is a small upturn, indicating there is a higher power input required to cause a resistive event. In the inset of Fig. 4.11 (b), over the frequency range probed, the average period has a clear dependency on f_{ac}. The lowest frequency, 3.3 Hz, has a very large error due to the small number of peak fields available for fitting. The reduction of period with an increasing measurement frequency could be caused by either a change in the probe time-scale, or a change in the driving frequency. Later in this chapter, DC probes find the time-scale to be of the order of 1 s. In the vortex induced OMR model, the reduction of OMR magnitude at high f_{ac} can be considered to be due to having a much higher driving frequency than the system fundamental frequency. As the measurement frequency nears MHz, the Lorentz driving force on the vortices will be fast relative to the vortex response times. The length of time that the current or force is in one direction is very small. The result of this is that the vortices never receive enough energy to overcome the pinning potential. The vortices may have a small oscillation amplitude, but be unable to escape the pinning potential to dissipate energy. This would also result in the observed increase in magnetic field required to stimulate the first resistive event. As in the case of reducing the applied current, if the frequency were to be increased further we can expect that the OMR effect will disappear as the applied magnetic field required to give the adequate Lorentz force to liberate the vortices increases above $\mu_0 H_{c2}$. This would give zero resistivity until a sharp, monotonic resistance transition to the normal state at $\mu_0 H_{c2}$. The other OMR candidate origins cannot explain this frequency dependence as they cannot have a time scale of the order of 1 s.

From the temperature, current and frequency dependence of the average period we can summarise that increasing the temperature acts to shift the OMR effect to lower fields and cause a background resistance so large that the effect cannot be observed; the current amplitude clearly plays a strong role in determining the field at which the OMR peaks occur, this could be attributed to Lorentz forces and edge barrier effects; and the f_{ac} dependence has shown that at MHz frequencies the period reduces, as the driving time-scale becomes much faster than the reaction time-scale of the system. The study of the $\mu_0 H_{Peak}$ and the average periodicity point
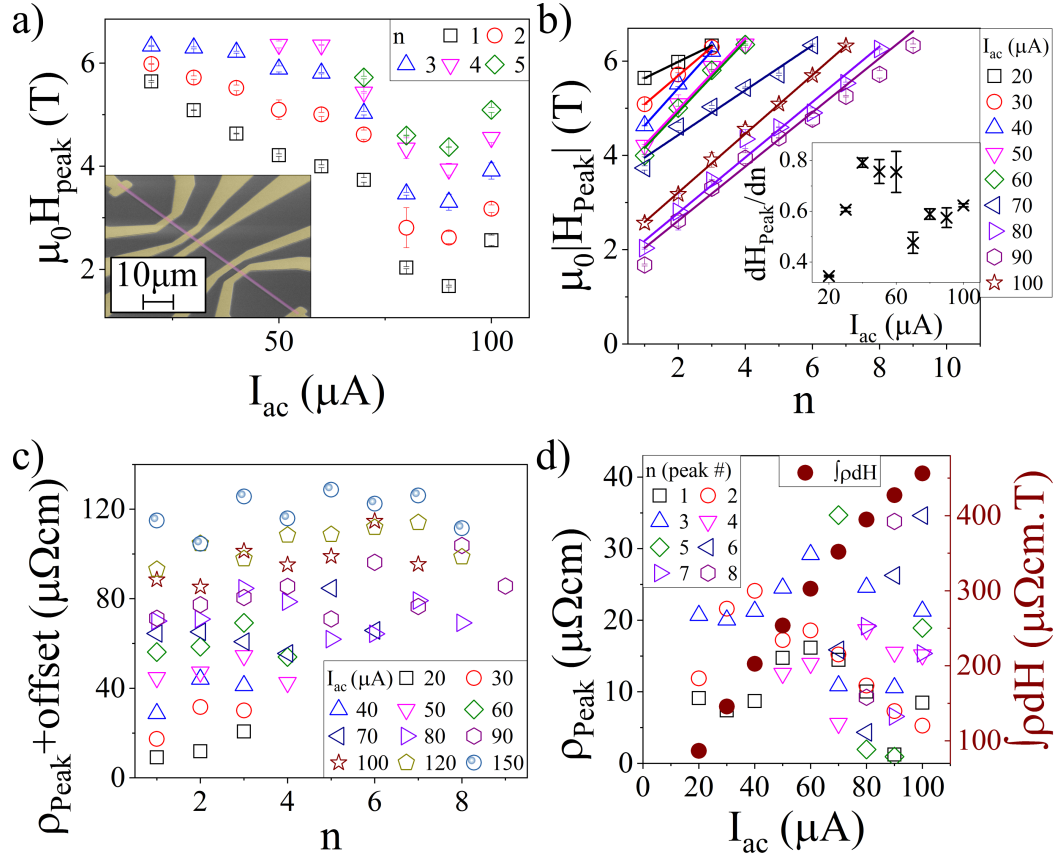
Figure 4.10: Applied AC amplitude dependence of the OMR fit parameters for a Nb nanowire in the transverse orientation. Measurement frequency = 773.7 Hz. Temperature = 1.6 K . Thickness = 20 nm, width = 0.8 μm, length = 33 μm, $T_c = (3.8 \pm 0.6)$ K. a) The centre field of each Gaussian peak fit vs the applied AC current amplitude. Inset shows an SEM image of the nanowire used in this study, coloured to distinguish Nb and Au. Note two lower order peaks were observed at 80 and 90 μA only. b) The centre field of each Gaussian peak fit vs the peak order n as defined in Fig. 4.6. Inset: the gradient of the linear fit vs applied AC current amplitude. c) The maximum resistance in each Gaussian event vs peak order. A constant offset of 20 $\mu\Omega cm$ separates the temperatures for clarity. d) The maximum resistance (open symbols, left y-axis) in each Gaussian event vs applied current amplitude, right hand axis shows the total integrated OMR (solid circles). In terms of current density, 20 μA = 1250 MAm^{-2} and 100 μA = 6250 MAm^{-2}. During analysis the subtracted background resistance was taken as the data at the lowest current amplitude.
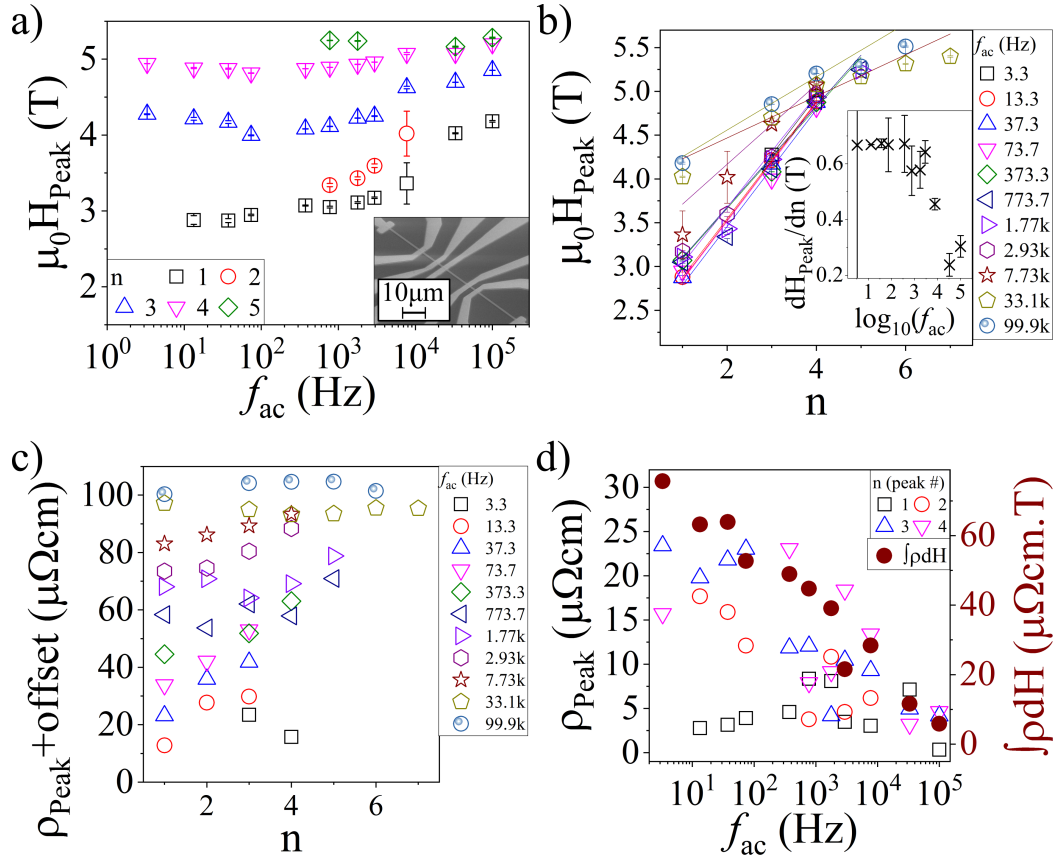
Figure 4.11: Applied AC frequency dependence of the OMR fit parameters for a Nb nanowire in the transverse orientation. Measurement temperature = 1.6 K. Current amplitude = 50 μA. Thickness = 20 nm, width = 0.8 μm, length = 33 μm, $T_c = (3.8 \pm 0.6)$ K. a) The centre field of each Gaussian peak fit vs applied AC frequency. Inset shows an SEM image of the nanowire used in this study, coloured to distinguish Nb and Au. b) The centre field of each Gaussian peak fit vs peak order, n. Inset: Gradient vs applied AC frequency. c) The maximum resistance in each Gaussian event vs peak order. d) The maximum resistance (open symbols, left y-axis) in each Gaussian event vs applied current frequency, right hand axis shows the total integrated OMR (solid circles). During analysis the subtracted background resistance was taken as the data at the highest frequency.

to periodic vortex motion, modulated by edge barriers, as the most probable cause of the OMR in these samples.

4.3.1.2 Peak Field Step Size

While the average period is a powerful measure of the general dependency of the environmental parameters, in general, the magnetic field step between peaks is not perfectly periodic. This is encompassed in the large error associated with the linear fits to $\mu_0 H_{Peak}$ vs n. With regard to the slight aperiodicity observed in these Nb nanowires, it is worth noting that Berdiyorov *et al*. [19] discuss the influence of defects on the period of the OMR effect. In an ideal sample the OMR is perfectly periodic, however the introduction of disorder and pinning sites causes aperiodicity in the otherwise periodic OMR effect.

4.3.1.3 Magnitude and Power Loss

The maximum resistivity, ρ_{Peak}, the peak area, A_{Peak}, and the total OMR integral, $\int \rho dH$, give a measure of the power dissipated by an event. $\int \rho dH$ is a measure of the total power dissipated by the OMR effect during the superconducting transition. Fig. 4.9 (c) and (d) show that as the temperature is increased the most resistive event is not always of the same order, n. It is also clear from the total OMR integral that, there is an optimum temperature for OMR. Below this thermally excited vortex motion will be reduced, and above this the OMR events merge with the resistive background. Fig. 4.10 (c) and (d) show that for the range of currents studied the peak orders have a structure where high resistivity and small resistivity peaks are mixed, but there is a strong overall trend of an increasing $\int \rho dH$ with I_{ac}. It is pertinent to note that the smooth connection between the OMR effect and the smooth background resistance results naturally from the fact that the normal state is effectively a fully packed, unpinned vortex lattice in constant motion. Fig. 4.11 (c) and (d) show that, as expected from the discussion of the average period at high frequency, the resistance due to the OMR tends to zero around the MHz range. Again, this is considered to be due to the high driving frequency relative to the fundamental relaxation time scale for the vortex lattice.

To cause maximum power absorption, the driving force must be in resonance with the dissipative effect. Radio frequency studies of vortex lattice relaxation timescales have shown that these are typically of the order of MHz-GHz [137, 138]. Below this time scale there should be no observable frequency dependence in dissipation from an isolated vortex. In contrast, Nb Corbino disks have been observed to have resistance switching with a period of 1.2-1.5 s, a frequency of ~1 Hz [137]. This is not explored in great detail, however is attributed to thermally driven metastable vortex lattice arrangements. That work also suggests the Corbino disk shape may play a role due to the unusual effects generated by the geometry. However, it has also been suggested that the Corbino disk is just a convenient demonstration of the effect, and that it may be observed in other circumstances [139]. This later investigation observes an unstable jump in IV measurements. Later in this chapter we will discuss a similar effect in Nb nanowires. It is possible that there are two different timescales involved in the motion of the vortices. One, the relaxation of a free moving vortex of the order of MHz-GHz and two, the relaxation of the vortex lattice under rearrangement stress. It also pertinent to mention that above a threshold frequency, in the high GHz range, superconductivity breaks

down as the normal state electrons dominate the resistance. This study has not probed such high frequencies, however it would be interesting to test similar samples up to this breakdown frequency. From the discussions presented here, it is unlikely that a vortex induced OMR would reoccur, as at high frequency the vortices are effectively trapped in pinning sites. However, at the cross over between superconductivity and the normal state the system may behave differently.

4.3.1.4 Magnetic Field Orientation

Common causes of oscillatory magnetoresistance such as the Little-Parks effect and SQUID interference require specific geometries. An angular investigation should elucidate if any of these effects are involved in the observed phenomena. The effects also require a loop-like geometry which is not explicitly present in this system. It has been argued that weak sections of a sample such as grain boundaries, damaged areas or anti-proximitised sections could generate such a scenario [33]. In order to generate a collective, constructively interfering effect, weak sections would have to be of a similar size and regularity. Berdiyorov *et al*. [140] categorically show that a Nb strip with regular holes generates an OMR effect. Interestingly, this is entirely attributed to vortex motion, rather than a quantum interference effect. The result of this discovery is that even if there is a case where there are regular weak points in a superconducting strip/wire, the dominant process will be periodic vortex motion induced OMR. To further demonstrate the OMR effect is not caused by interference, the following is an investigation into the angular dependence of the effect. This includes magnetic field sweeps at several in plane angles (θ) and at several transverse, in plane to out of plane angles (ϕ). Angular measurement orientations are defined in Fig. 3.11, which is replicated throughout this work.

In plane measurements are key to determining whether the effect is from an interference effect, as in every case the voltage is produced perpendicularly to the magnetic field orientation. For example, in the SQUID or Little-Parks effect, when measuring the voltage along a wire, only the component of the magnetic flux transverse to the wire is important. The flux through transverse loops will tend to zero as the longitudinal configuration is approached, and thus $\mu_0 H_{Peak}$ will tend to infinity. This should manifest in no effect in the longitudinal configuration. Fig. 4.12 shows some select observations of OMR with in plane rotations. Two relevant observations can be made from this data. Firstly, the peak field is modulated by a maximum factor of ~2, and appears to have the maximum close to in plane transverse (θ ~0°) and a minimum close to in plane longitudinal (θ ~90°. This is contradictory to the expectations of the SQUID or Little-Parks phenomena, where $\mu_0 H_{Peak}$ should be largest in the longitudinal orientation. It is possible that the relatively small change in peak field shown here is actually not related to the in plane rotation and is actually caused by an out of plane component of magnetic field that changes upon an in plane rotation. This out of plane component could occur due to a small error in the mounting or from having a small non-uniformity in the applied magnetic field. As we will discuss later in this section the out of plane field has a much larger influence on the peak field than the in plane field.

One could argue that with the magnetic field along the length of the wire, vortices will experience a negligible Lorentz force. However, in the in plane configuration, and with wire thickness 2ξ-4ξ, a lattice of straight vortices fully aligned with the magnetic field is

unreasonable to expect. It is more reasonable that the vortices will tend towards being out of plane. This will be a much stronger effect for wires of thickness 2ξ. Any small inhomogeneity in the applied magnetic field or the arrangement of pinning sites could result in some vortex bending. The bending reduces the vortex length and thus total energy of each vortex, and so is likely to be more energetically favourable. The picture of in plane vortices is now of spaghetti strings with some component transverse to the current direction. This transverse component is then susceptible to creating a voltage along the length of the wire through vortex motion. Spaghetti lattices could also reduce $\mu_0 H_{Peak}$ as the lattice is more flexible. In the longitudinal configuration, the vortices, will tend to move in any direction transverse of the wire, whereas in the transverse, in plane configuration the vortices will move predominantly towards the out of plane direction. This higher freedom of movement in the longitudinal orientation could explain the observation of higher ρ_{Peak} in this configuration.

Two samples are shown in Fig. 4.12. The first has a large in plane angular dependency in $\mu_0 H_{Peak}$, shown in panel (a), and ρ_{Peak}, shown in panel (b). The second has a much smaller angular dependency, shown in panels (c) and (d). For example, in the latter case, values of $\mu_0 H_{Peak}(\theta)$ for n=1 do not vary far beyond the error. The reason for this distinction between the two samples could simply be a misalignment in loading into the cryostat, where the out of plane component of field varies more in the sample with the much larger change. A more satisfying explanation, which fits in with the idea that the vortices weave through the wire, comes from the fact that the wire in panels (a) and (b) is half the thickness of the wire in panels (c) and (d). A thinner wire is more prone to having weaved vortices, with a larger out of plane vortex component. This would allow vortex reconfiguration at a lower field and generate more resistance in the longitudinal orientation. The phenomena of tilted vortices is explored and modelled by de C. Romaguera et $al.$ [141], where the small thickness tilts vortices towards a length reduced configuration, reducing the energy of the vortices. If this is the cause of the angular dependence here, further studies of OMR in nanowires could focus on a thickness dependence in these two orientations, elucidating a trend or limit to the in plane angle variation of the event inducing field, $\mu_0 H_{Peak}$.

Transverse rotations, where the field and current are always perpendicular can elucidate many physical phenomena that rely on other parameters than the cross product of the magnetic field and the current vector. OMR is no exception and has some surprising characteristics. Fig. 4.13 shows one example of OMR in transverse rotation, and the key extracted parameters for a set of five samples, nominally identical except for thickness. On close examination, in Fig. 4.13 (a), the angular dependence of the OMR is interesting. The OMR appears as distinct events with clear Gaussian distributions at transverse, near in plane, $\phi = 0$. However, at angles tilted towards out of plane, the peaks are compressed together and $\mu_0 H_{Peak}$ and ρ_{Peak} reduce. The overarching trend in $\mu_0 H_{Peak}$, see Fig. 4.13 (b), shows that at low ϕ, near in plane, the field required to create an event is large, while at large ϕ, near out of plane, the field is reduced or events are not observable. This relationship is not simple, as it must include many parameters that change at different orientations such as the demagnetisation factor, the vortex travel distance, the vortex tilt and the vortex length. The length changes the vortex total energy and the number of pinning sites that the vortex interacts with. The calculated demagnetisation factors increase the internal magnetic field by 5% at low ϕ and 50% at high ϕ, this does not account for the trends. However the travel distance (or dimension in the direction of the Lorentz force) can be calculated and the vortex length can be estimated. The vortex travel distance is
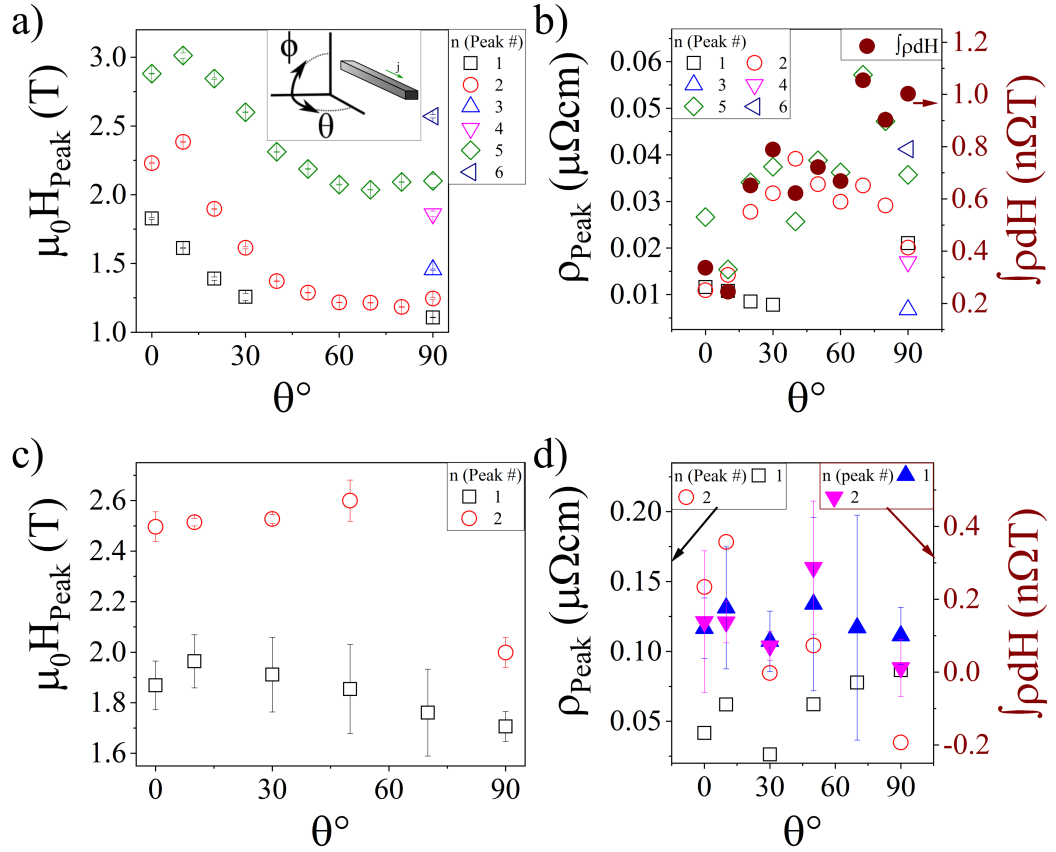
Figure 4.12: In plane rotation OMR extracted parameters for two Nb nanowires. a) and b) Thickness = 20 nm, width = 0.8 μm, length = 33 μm, T_c = (3.8 ± 0.6) K. c) and d) Thickness = 40 nm , width = 1.4 μm, length = 33 μm, T_c = (6.2 ± 0.1) K. a) and c) The peak field of each Gaussian distribution for a quarter of a complete in plane rotation, positive and negative fields are averaged. Angle θ is defined in the inset of (a), a replica of Fig. 3.11. b) and d) The peak resistivity (open symbols) and integrated peak resistivity (solid circles). During analysis the subtracted background resistance was taken as a smooth spline to points of minimum resistance.

simply $t/\cos(\phi)$ at small ϕ and $\sim w$ at large ϕ. The vortex can be assumed to be rigid and thus have vortex length $l_v \sim w$ at small ϕ and $t/\cos(\phi)$ at large ϕ. This rigid vortex assumption is not appropriate, as discussed previously, vortices are prone to bending to reduce the energy. A more appropriate image, takes into account the minimisation of the vortex energy by vortex tilting, as described by de C. Romaguera *et al.* [141]. The tilted vortex picture assumes that close to the surface there is a length of vortex which is fixed normal to the surface. This is in fact required, as the screening current at the surface can have no component perpendicular to the surface, and the vortex screening current and flux must be perpendicular. The vortex will be smoothly connected between these two points and may experience pinning, distorting the shape. The true length cannot be known and will be different for each vortex. However, de C. Romaguera *et al.* calculate that a straight line between the two entry points of this vortex model, with perpendicular entry points, is a good approximation for a vortex length.

The vortex length proposed is:

$$l_v = \begin{cases} \frac{w}{\cos(\phi_{dCR})}, & \phi_{dCR} < \phi_D, \\ \frac{t}{\sin(\phi_{dCR})}, & \phi_{dCR} > \phi_D \end{cases},\tag{4.2}$$

where $\tan(\phi_D) = \frac{t}{w}$ and $\tan(\phi_{dCR}) = \frac{\tan(\theta)}{1-\frac{2\xi}{t}}$ defining two new angles: ϕ_D is the angle of the diagonal across the nanowire, and ϕ_{dCR} is an angle proposed by de C. Romaguera *et al.* which encompasses the tilting towards out of plane, due to the entry and exit points of the vortex. The angle and effective vortex shortening is shown schematically in Fig. 4.14 (e) for a vortex tilted towards out of plane.

4.3.1.5 Nanowire Size

As discussed earlier in this work, the effect of changing the dimensions of nanowires that show OMR is not fully explored in literature, with most studies focussing on a set of samples or a single sample. In this study we have varied the sample thickness and width, and the length between voltage contacts. What follows is a summary of observations and possible explanations.

The most straightforward comparison of sample size available is between measurements of the same sample using contacts to measure the voltage, changing the length of sample measured. Fig. 4.15 (a) shows this for a sample under transverse rotation, from in plane to out of plane. The most striking features of this being that at an in plane angle, $\phi = 0°$, the length has a negligible effect on the MR observed. As the angle is tilted towards out of plane the MR begins to be distinguishable for the two lengths. Fig. 4.15 b) shows the difference between the two lengths in (a). As the angle ϕ is increased so does the deviation from $\Delta R = 0$. The two lengths are shown to have the same in plane MR at a range of I_{ac} in Fig. 4.15 (c). These results suggest that the intrinsic mechanism of OMR is not dependent upon the length of sample probed. The deviations between the two lengths when the magnetic field has an out of plane component could be due to the rapid destruction of the superconducting state by the out of plane magnetic field. Following from the vortex motion toy model proposed in Chapter 2, one might expect a longer sample to have a greater number of vortices stabilised in each row, n_{stable}, and thus a greater period. The period is not effected by the length probed, which is
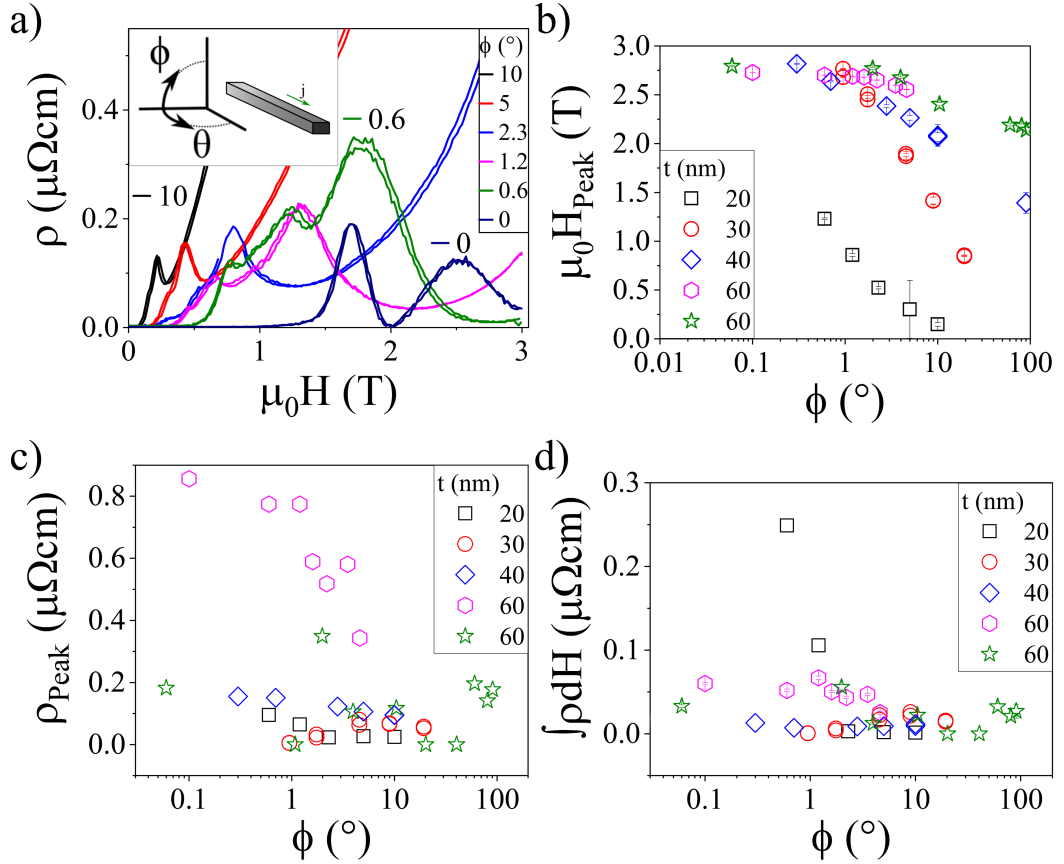
Figure 4.13: In plane to out of plane, transverse rotation MR and OMR extracted parameters. a) Example data for a 20 nm thick Nb nanowire showing the complex evolution of the OMR. Both positive and negative magnetic field sweep directions are shown. There is negligible hysteresis in the OMR effect. Angle ϕ is defined in the inset of (a), a replica of Fig. 3.11. b)-d) Extracted parameters for five nanowires with thickness = 20, 30, 40, 60, and 60 nm and widths of all ~1 μm. For simplicity only one dominant peak at each angle is shown. b) The peak centre field of the most dominant peak in the OMR of each sample vs out of plane angle. c) The maximum resistance of the most dominant peak in the OMR of each sample vs out of plane angle. d) The area integral of the most dominant peak in the OMR of each sample vs out of plane angle. During analysis the subtracted background resistances were taken as a smooth spline to points of minimum resistance.
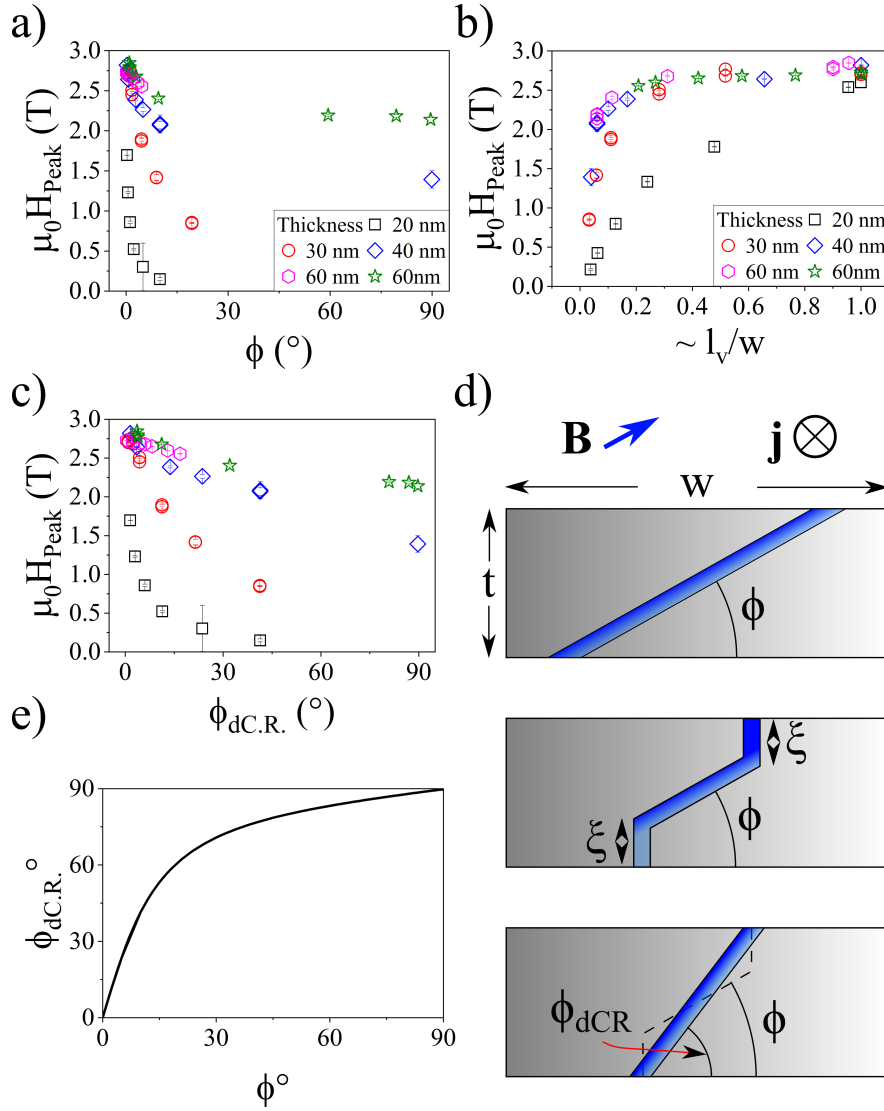
Figure 4.14: In plane to out of plane, transverse rotational OMR parameters and periodic vortex motion analysis. a)-d) Dominant extracted peak field for five samples with thickness = 20, 30, 40, 60, and 60 nm and widths of all ~1 μm. a) vs out of plane angle. b) vs vortex travel distance. c) vs the effective angle calculated by de C. Romaguera. d) vs the de C. Romaguera vortex length, normalised by the width of the sample. e) The construction of ϕ_{dCR}. Each box shows a cross section across an idealised nanowire. Top, a straight vortex perfectly aligned with the external field. Middle, a vortex following the field with end points at normal to the surface. Bottom, the approximation used by de C. Romaguera *et al*. [141]. Angle ϕ is defined in the inset of (a), a replica of Fig. 3.11. During analysis the subtracted background resistance was taken as a smooth spline to points of minimum resistance.
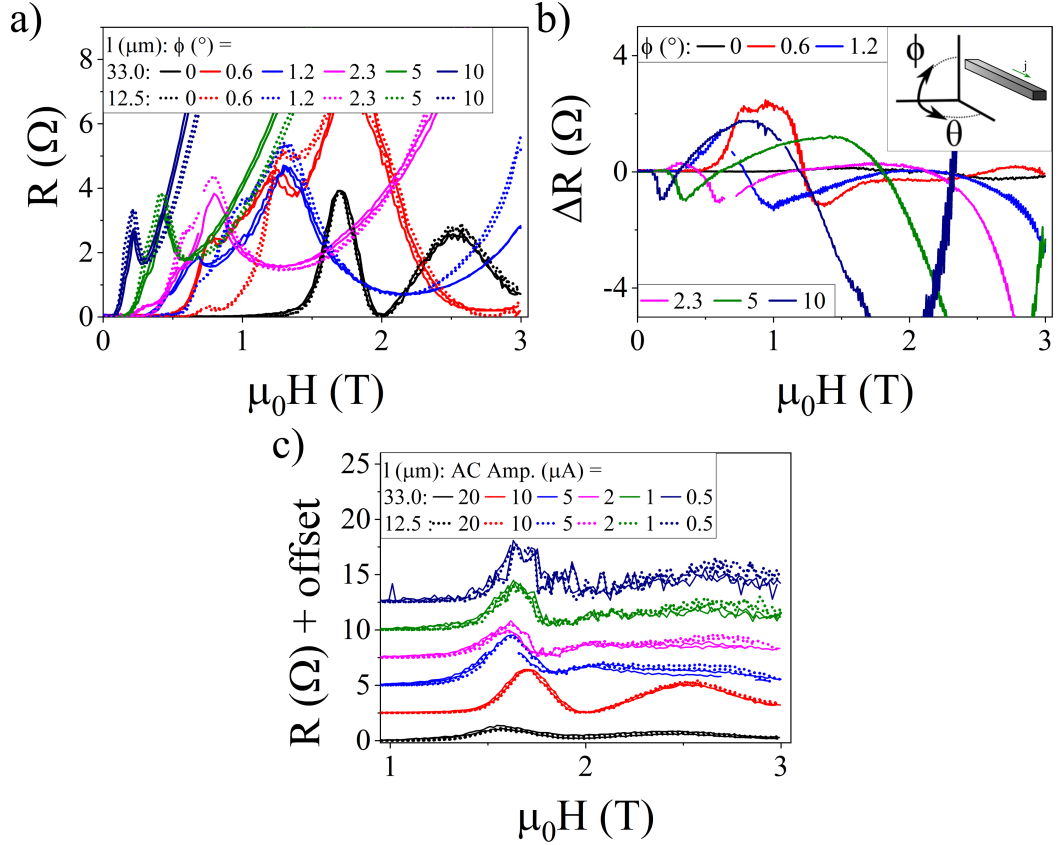
Figure 4.15: Voltage contact separation dependence on the MR of a Nb nanowire. Thickness = 20 nm, width = 0.8 μm. Lengths = 33.0 and 12.5 μm, T_c = (3.8 ± 0.6) K. Temperature = 1.6 K. a) In plane to out of plane, transverse rotation MR for both lengths. Applied current amplitude = 10 μA. Temperature = 1.6 K. AC frequency = 773.7 Hz. b) The difference between the two lengths shown in (a). c) In plane, transverse MR at a range of current amplitudes, for both lengths. Angle ϕ is defined in the inset of b), a replica of Fig. 3.11.

understandable as n_{stable} should be defined by the total length of the sample. In summary, the length of sample probed has little to no effect on the OMR characteristics when measured in plane. This knowledge helps to generalise the measurements taken when voltage contact separation is not the same. This study has not changed the total length of nanowire. This would be an interesting study to test the effect of sample length on OMR period.

While this thesis is not designed to investigate the width of nanowires in relation to the OMR effect. In the range of widths measured there is no clear correlation between wire width and the presence or size of an OMR signal. However, it has been observed that large widths suppress the OMR signal and replaces it with a smooth, sharp transition.

The focus of this study has not been to explicitly determine a thickness threshold for which OMR will occur in Nb nanowires. As discussed previously, the thickness of nanowire grown was chosen that it was in the range of 2ξ-6ξ. Judging using the data available from the samples
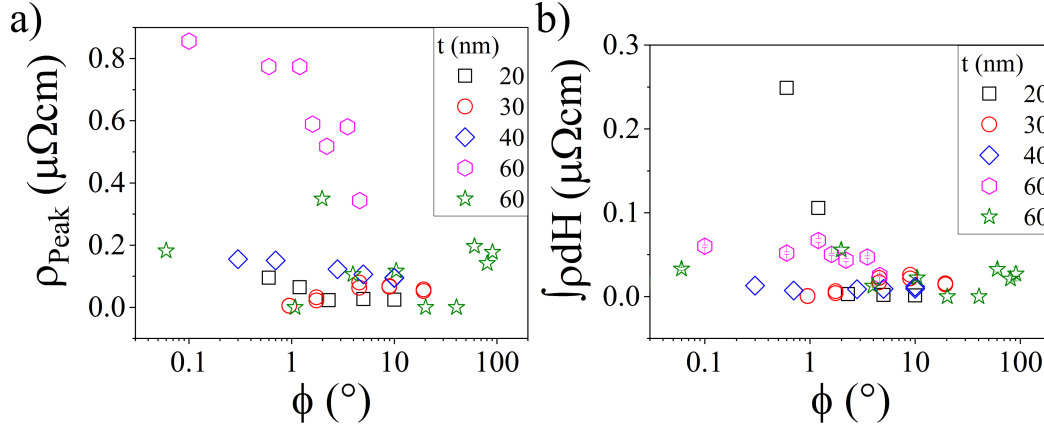
Figure 4.16: In plane to out of plane, transverse rotation OMR parameters, showing the a) Resistivity and b) Peak area of the dominant peaks for a set of 5 samples with thickness = 20, 30 , 40, 60, and 60 nm and widths of all ~1μm. Angle ϕ is defined in the inset of (a), a replica of Fig. 3.11. During analysis the subtracted background resistance was taken as a smooth spline to points of minimum resistance.

grown, it is possible to conclude that thinner nanowires exhibit a clearer OMR signal than thicker nanowires. The majority of data presented in this chapter is from nanowires of thickness 20 nm or 40 nm. However, when we consider the data set showing the angular dependence of the OMR under transverse, in plane to out of plane rotation, 60 nm Nb nanoribbons have more robust OMR. Peaks are observable up to $\phi = 90°$ and have only a small reduction in the peak field required to create the OMR events, as shown in Fig. 4.14 (a). Fig. 4.16 shows the peak resistivity, ρ_{Peak}, and peak area, A_{Peak}, for the five samples shown in Fig. 4.14. Fig. 4.16 demonstrates the diminishing of the OMR magnitude for the thinner nanowires at $\phi \approx 25°$, while the 60 nm thick nanowire has OMR in the out of plane, $\phi = 90°$, configuration. The difference may be some fundamental OMR physics, however it is apparent that for thinner wires with an out of plane magnetic field the superconductivity is rapidly destroyed, and so any OMR effect that might occur is overshadowed by the rapid penetration of flux at small magnetic fields. Generally, to summarise the observations of many samples, the OMR effect was more obvious in 20 and 40 nm nanowires, although only with an in plane field.

To summarise the dependence of OMR on the sample dimensions, the length appears to have a minimal effect on the intrinsic OMR. The width and thickness are both required to be below a poorly defined threshold to exhibit OMR, although this alone does not guarantee OMR will be observable. As the thickness of nanoribbon/ nanowires nears the order of ξ, OMR should be strong when the field is applied in the plane of the sample. The overriding observations of all samples is that the periodicity and strength of the OMR is not predictable. This matches well with the prediction of Berdiyorov *et al*. [19], that pinning sites can alter the periodicity. As the samples studied are expected to have a reasonably high pinning density, the period should vary considerably between samples.

4.3.1.6 Complex Impedance

Inductance and capacitance in a circuit give a complex impedance, which can be determined using lock-in amplifier techniques. Faults in the circuit or poor wiring could give spurious complex impedances, however these would also be present in normal state measurements. In the AC measurements discussed previously in this section, the resistance is represented using the magnitude of the impedance, $R = \sqrt{X^2 + Y^2}$, where X and Y are the in phase and out of phase component of the impedance. Alarmingly, when a closer examination of the X and Y components is presented a complex inductance and sign reversal in the OMR effect is illuminated.

In superconductors, vortex motion can be responsible for the out of phase or the sign reversal of voltages, Hagen *et al*. [142] observe a reversal of the Hall effect in the superconducting state in YBCO and Nb films, near to T_c, over a low field range. This parameter range is exactly when vortex motion is expected to be most prevalent. The discussion dismisses traditional models for the force on vortices, as these cannot provide the counter motion of vortices required to generate a reversal of the Hall coefficient. Instead, an alternative friction force developed for superfluid Helium by Hall and Vinen [143], and Ambegaokar, Halperin, Nelson and Siggia [144] is proposed. This alternative friction force has a cross product component which allows vortex motion to counter propagate with respect to the supercurrent direction. The validity of an additional force is justified by Hagen *et al*. as they claim it does no work. This statement invalidates the work, force, distance relationship, $W = Fd$, as the vortex will pick up a component of velocity in the direction of the new force.

A more robust explanation to the superconducting Hall anomaly is provided by Ao [145], where pinning of correlated vortices in a lattice, rather than imposing a force on each vortex, gives a Hall anomaly. An intermediate pinning density creates defects in the vortex lattice, interstitials or missing vortices. It is these that dominate the transverse transport and give a reversed Hall coefficient. The work also discusses a relationship between the Hall resistance and the linear resistance, implying there may be a reverse linear MR in certain cases. Interestingly, Ghenim *et al*. [146] have experimentally observed an oscillating Hall resistance in Nb strips, which they attribute to the same phenomena described by Ao. Reverse MR could easily be included in the vortex motion OMR model, as it already includes the correlated motion of vortices in a pinning landscape.

An example selection of data showing the complex phase of the OMR measurements is shown in Figs. 4.17 and 4.18. From these, we can qualitatively examine the change with I_{ac} and f_{ac}. As noted in previous discussions, I_{ac} affects the Lorentz force acting on the lattice and f_{ac} is a probe of the relaxation time of the vortex lattice .

In Fig. 4.17 we can see that while the overall OMR effect increases, at higher currents the proportion of OMR that is out of phase, Y/X, increases. The higher driving force leads to more vortices being liberated from pinning sites and overcoming edge barriers. Both of these require vortex rearrangement up until the point that there is constant uniform motion from the vortex lattice. This is equivalent to the normal state. Thus there is a large out of phase OMR effect at high current, which rapidly decays to zero as the field is increased and the current and magnetic field suppress superconductivity. At applied currents significantly lower than the critical current but high enough to have thermally excited vortex depinning, vortex motion remains non-uniform and inconstant from the onset of resistivity, until the normal state is reached. The non-uniformity of the vortex motion generates peaks in and out of phase that do
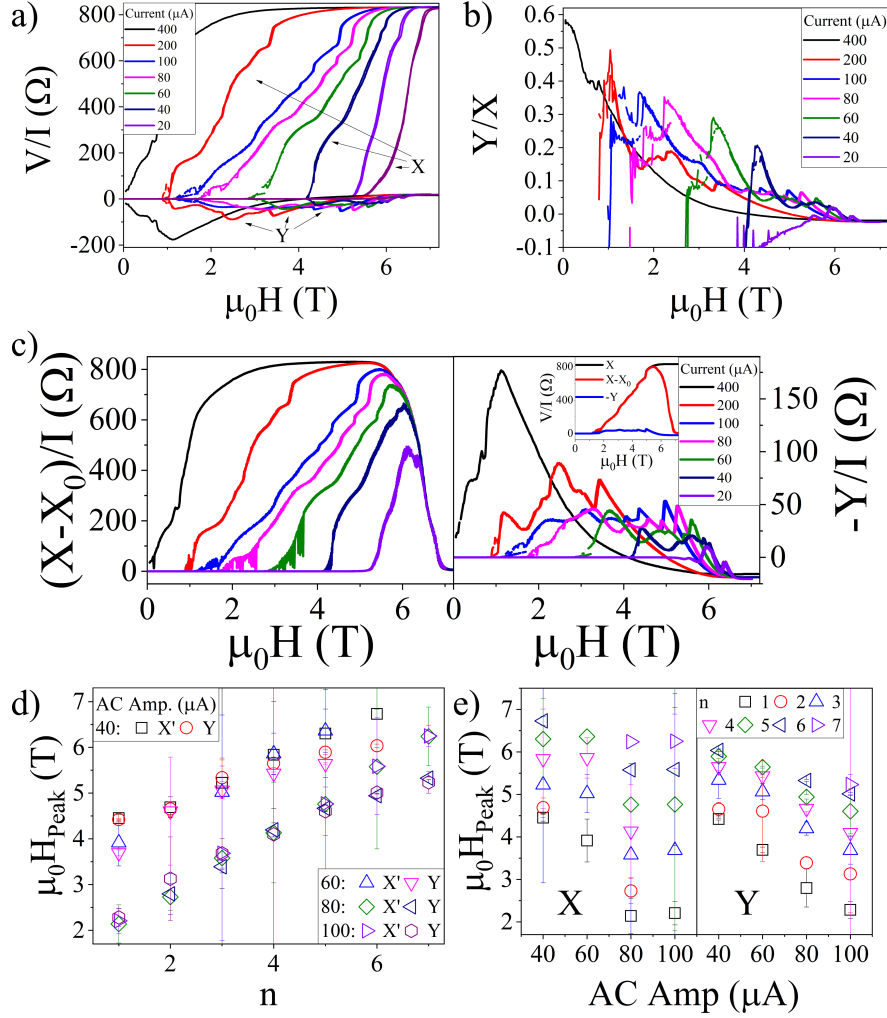
Figure 4.17: In phase and out of phase voltage measurements, at a range of applied current values. AC frequency is fixed at 773.7 Hz. Temperature is 1.6 K. Thickness = 20 nm, width = 0.8 μm, length = 33 μm, $T_c = 3.8 \pm 0.6$ K. Magnetic field orientation is in plane, transverse. a) Phase separated OMR signal. X is in phase, Y is out of phase. Note the Y component is negative. b) The ratio of the in phase and out of phase components. c) Comparison of the in phase and out of phase component after a background subtraction from the in phase. The subtracted background, X_0, is taken as the data for the lowest current. The inset shows the amplitudes of X, $X - X_0$ and $-Y$ for 100 μA. d) The peak fields extracted from the in phase and out of phase components, shown in (c) vs the peak order. e) The peak fields extracted from the in phase and out of phase components, shown in (c) vs the current amplitude.

not necessarily align to the same $\mu_0 H_{Peak}$. At the lowest currents, vortices remain pinned and there is minimal rearrangement. The result is that vortex displacement is small and dissipation is in phase.

Quantitative analysis of the in phase, X, and out of phase, Y, OMR voltages for the MR taken at a range of I_{ac} is shown in Fig. 4.17 (d) and (e). Both figures show that $\mu_0 H_{Peak}$ is the same, within the error, for components X and Y. Panel (d) demonstrates that, for the majority of OMR peaks, the in phase and out of phase match well. At high n, there is some deviation. This could be an artefact from the analysis technique. The background subtraction can skew peaks when the background is large. This is the case in phase for the highest n peaks. For $\mu_0 H_{Peak}$ extracted from in phase measurements there appears to be two levels, while for the out of phase component the change in $\mu_0 H_{Peak}$ is steady. The in phase data analysis requires the subtraction of a large, signal dominating, background resistance. Due to the difficulty in isolating the OMR peaks from the background of the in phase data, the out of phase component has smaller errors and a clearer observable trend. This observation provides a path to studying the intrinsic OMR effect without the need to subtract a subjectively defined background. Care should be taken to note that the phase between X and Y is not constant, as shown in Fig. 4.17 (b). This caveat means that from this study we can conclude that $\mu_0 H_{Peak}$ is identical for the two components, however the OMR magnitude for the two components may differ. Further experiments, where the background does not dominate the signal, would be required to test if the X and Y components of OMR are proportional.

Fig. 4.18 (a) shows the in phase, X, and out of phase, Y, components for the frequency dependent OMR measurement. Fig. 4.18 (b) demonstrates that the phase (encapsulated in the ratio of Y/X) is not constant during the field sweep and has no hysteresis. This signifies that the out of phase component is not simply some capacitive poor connection, or inductive loop in the circuitry, but is an intrinsic effect associated with the OMR. In the transverse, in plane orientation, the vortex travel width is 20 nm, and so vortices will be packed very tightly in the sample. A combination of a regularly rearranging vortex lattice, pinning, and edge barrier effects could generate resistances that lose phase coherence with the probe AC oscillation. This would be prominent if the vortex lattice relaxation timescale differed greatly from $1/f_{ac}$. The continual perturbing of the vortex lattice by the AC current, and the sweeping of the magnetic field, generate a system continually adapting to these inputs. Vortex lattice instabilities will have a relaxation time associated with them as thermal excitations are required to displace the vortices from pinning sites. At the lowest frequency, there is still some lag between the input current and the resistive process, suggesting that the fundamental frequency of the process is $\lesssim 1$ Hz. This supports the general investigation into OMR with frequency, where the maximum OMR is observed at the lowest frequencies.

In summary, the out of phase component in AC magnetotransport measurements can be used to probe the OMR effect without the need to consider and subtract alternative resistance mechanisms.
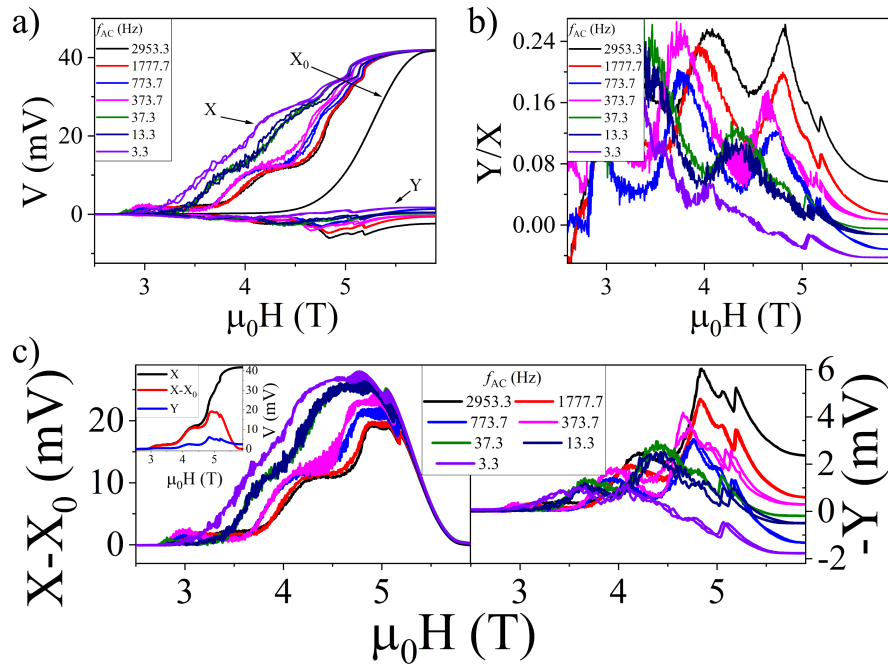
Figure 4.18: In phase and out of phase voltage measurements, at a range of AC frequency values. AC amplitude = 50 μA. Temperature is 1.6 K. Thickness = 20 nm, width = 0.8 μm, length = 33 μm, $T_c = 3.8 \pm 0.6$ K. Magnetic field orientation is in plane, transverse. a) Phase separated OMR signal. X is in phase, Y is out of phase. Note the Y component is negative. b) The ratio of the in phase and out of phase components. c) Comparison of the in phase and out of phase component after a background subtraction from the in phase. The subtracted background, X_0, is taken as the data for the highest frequency. Inset shows the amplitudes of X, $X - X_0$ and $-Y$ for 2953.3 Hz.
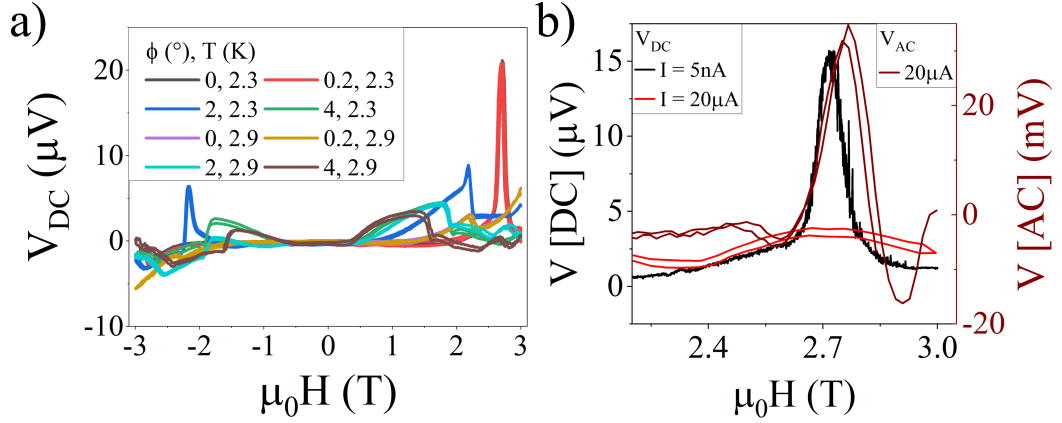
Figure 4.19: MR measured with a direct current source. Thickness = 30 nm, width = 1.4 μm, length = 33 μm, T_c = (5.3 $\pm$ 0.2) K. a) Magneto-voltage at two temperatures, 2.3 K and 2.9 K and four ϕ, transverse in plane to out of plane, angles: 0°, 0.2°, 2°, and 4°. Angle ϕ is defined in the inset of (a), a replica of Fig. 3.11. b) Comparison between DC and AC. The magneto-voltage is normalised. The DC current amplitudes are 5 and 20 nA. The AC measurement frequency = 773.7 Hz and current amplitude = 20 μA. The magnetic field is transverse, in plane and the temperature = 2.3 K.

4.3.2 Oscillatory Magnetoresistance in DC

4.3.2.1 Constant Current Magnetoresistance

AC measurements are useful for fast, low noise resistance measurements, however in this case they must be compared with DC measurements. The reasoning here is that f_{ac} had a profound effect on the measured signal and so a DC probe should help understand the low frequency limit, $f \to 0$. To reduce measurement noise, each data point is an average of 8 measurements at $\pm I_{DC}$, where positive and negative are alternately used to compensate thermally induced voltages. While the current does alternate polarity, each voltage measurement is taken at a stable current value, and the resulting voltage readout is an average of the absolute voltage.

Fig. 4.19 shows a selection of DC MR measurements for a Nb nanowire. As for the AC measurements, there is a superconducting region at low magnetic field followed by a non-monotonic resistance increase. Otherwise the similarities are not so clear. There is a clear asymmetry in the voltage with applied field direction and both directions include positive and negative induced voltages. As the AC MR effectively takes the magnitude of the signal, this directional information is lost. It is reasonable to expect the entry and exit barriers to vortex motion to be uneven across a nanowire. In addition, the magnetic field could include some non-uniformities, providing directional differences to the OMR voltage. As discussed previously, the dissipation voltage does not necessarily align with the direction expected from the Lorentz force due to the collective motion of the vortex lattice and lattice rearrangement. This OMR has the potential to generate the asymmetric and unusual patterns observed in these magneto-voltage curves.

Fig. 4.19 (b) compares similar DC and AC measurements. The OMR occurs in DC and AC at the same magnetic field, which is expected from the low frequency plateaux in Fig. 4.11
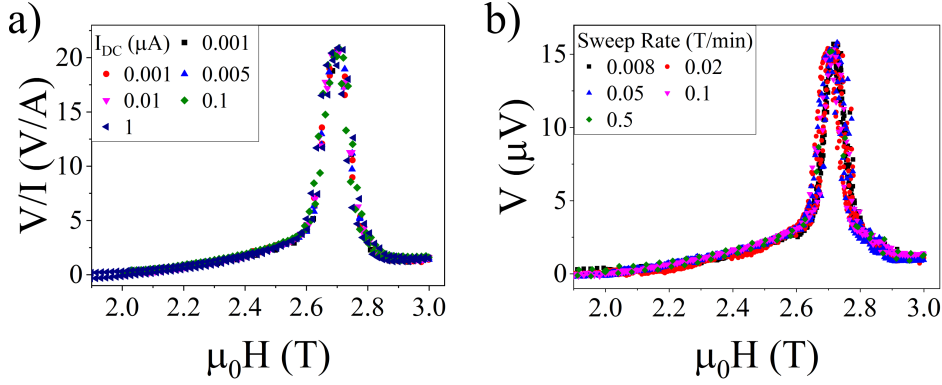
Figure 4.20: Current and sweep rate dependence on the magneto-voltage using a DC source. Thickness = 30 nm, width = 1.4 μm, length = 33 μm, T_c = 5.3 ± 0.2 K. Temperature = 2.3 K. Magnetic field is in plane, transverse. a) Current dependency of the OMR. Voltage is normalised by current. In terms of current density, 0.001 μA = 0.024 MAm^{-2}, 1 μA = 24 MAm^{-2}. b) Magnetic field sweep rate dependency of the OMR.

(a). This confirms that the AC and DC measurements are probing the same physical process. In this case, the magnitude of the OMR peak differ by 5 orders of magnitude. It is unlikely that this difference is due to differences in the environmental set up, which should be nominally identical. It is more likely that the different methods of electrically probing the induced voltage have a profound effect on both the induced voltage and the magnitude observed. This creates the question as to which of the probing techniques are more powerful.

In the range studied, the DC OMR is independent of the amplitude of the current applied. Fig. 4.20 shows that for the range of applied current magnitudes and magnetic field sweep rates, the DC OMR is unchanged. $\mu_0 H_{Peak}$ is constant and the peak voltage scales linearly with the current. AC measurements had a clear current dependence, the differences could be either due to the difference in the driving mechanism or from differences in the voltage measurement as AC and DC both stimulate and probe differently. The current density of these DC measurements is below that of the AC measurements as the effect was observed in this lower different range of currents. This may mean that DC probing is more sensitive to the OMR effect.

In summary, the DC OMR effect is observed and elucidates some properties that could not be distinguished in the AC measurements such as the strong asymmetry in the magneto-voltage signal, negative voltages. Following on from the MR measurements presented in this section, where the magnetic field was swept constantly and rapid measurements at a fixed current amplitude probed the resistance, the next section presents the results when the current is swept at a fixed field.

4.3.2.2 Pulsed IVs

Standard current-voltage (IV) characteristics can be determined by sweeping the applied current and measuring the voltage. In superconducting samples, and particularly nano-objects,

the current densities involved cause the material to heat and smooth out sharp intrinsic features. To overcome this issue, a pulsed IV is used which limits the amount of heat applied and gives the system time to dissipate the heat generated such that there is no smoothing or distortion of the IV characteristics. In generic superconducting samples, there is a low current range for which the voltage is zero and a high current, Ohmic range. The two ranges are usually connected by a sharp transition, at the critical current. In these nanowire samples, there are more features in the IV curve. The main parameter that is extracted is I_{step}, the current at which steps in the IV occur. These steps appear to be closely related to the OMR observed in DC and AC measurements. The IV characteristics do not match those expected for the Weber blockade type OMR effect. For a Weber blockade, the critical current should follow a zig-zag trend with applied magnetic field. As this is the main probe of this proposed OMR origin, it can be assumed that the observations presented here are not caused by a Weber blockade. The Weber blockade description requires the thickness in the out of plane orientation, in this case the width in the in plane orientation, to be smaller than the penetration depth. As the width of the nanowires is large, the entry and exit of a single vortex should not be observable using the critical current.

Fig. 4.21 (a) shows a selection of IV curves for a range a magnetic fields showing the complete spectrum of superconducting behaviour. From fully superconducting, 0 - 1 T, to fully normal and Ohmic at 7 T. At intermediate fields stepping and jumping between two different resistances is observed. The resistance jumps here provide further evidence of the time dependent, probabilistic nature of the OMR events. In particular environmental states the voltage measured can take two or more values. These environments are when vortex flow and rearrangement is possible, but must overcome an energy barrier. The voltage measured then depends upon this probabilistic vortex lattice rearrangement. When the pulse probes the system during a resistive event, the resistance is observed. While the vortices are stable a lower, or in the case of the first event zero, resistance/ voltage is observed. The consecutive stepping observed in these IVs can be compared directly to the AC OMR peak fields at fixed I_{ac}. In this orientation, in plane and transverse, the vortices can readily block a superconducting path, resulting in a monotonic increase in resistivity onto which the unstable jumps are superimposed. Comparing with the directly equivalent AC measurement, for which the MR data is shown in Fig. 4.6 (d), the resistance measured is monotonic with the OMR superimposed. Hence, the two measurements correspond to an equivalent scenario. Further supporting this idea is the observation that the trends in extracted step current, taken as an average where there are multiple jumps, matches well to the trends in AC peak field when the applied current is varied, shown in Fig. 4.21 (b).

The Lorentz force on the vortex lattice, scaled to many vortices in Eq. 2.35, should be proportional to the current pulse amplitude, I_{pulse} and $\mu_0 H$. Fig. 4.21 (c) shows the dependence of the product $\mu_0 H.I_{step}$ against $\mu_0 H$, in which a plateaux is observed for magnetic fields in the range 2.5 - 3.5 T. This smoothly connects to a linear reduction above 4 T. The plateaued region indicates that the imparted force on the vortex lattice at the step event is constant irrespective of the state of the system. At higher fields the vortex density increases. This could reduce the force required to generate OMR/ IV steps, as the vortices interact more, acting more like a fluid. The magnetic field dependence of the $\mu_0 H.I_{step}$ product suggests that the vortex lattice could evolve from being a weakly interacting array following an
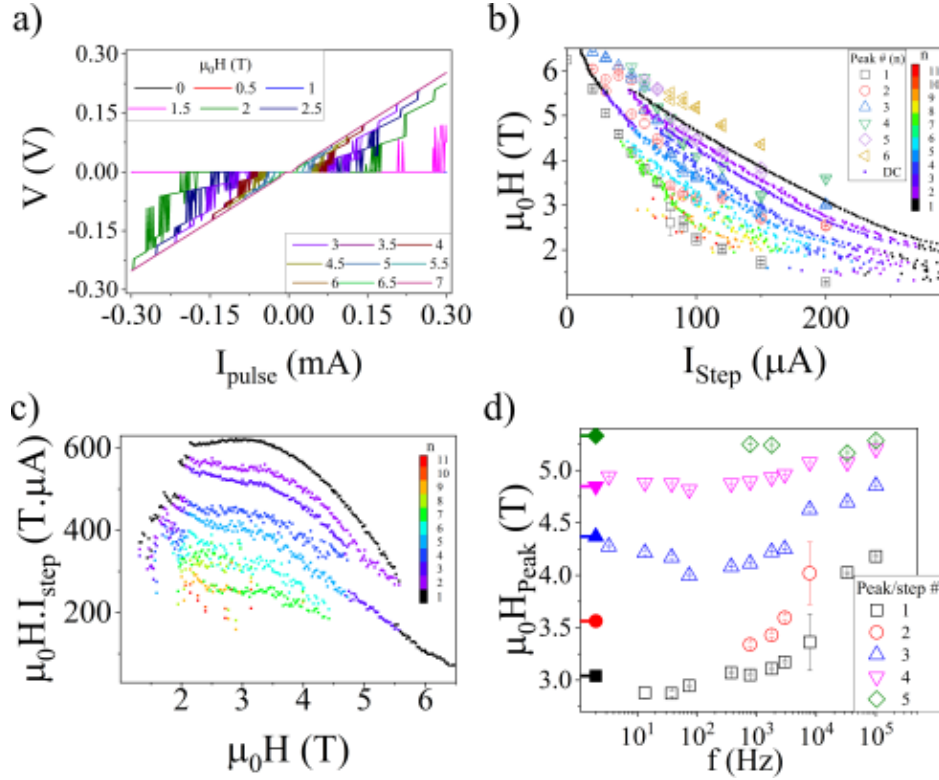
Figure 4.21: Pulsed IV measurements and extracted step characteristics for a Nb nanowire. Thickness = 20 nm, width = 0.8 μm, length = 33 μm, T_c = (3.8 ± 0.6) K. Temperature = 1.6 K. Magnetic field is in plane, transverse. a) IV characteristics for a selection of fields showing the evolution from a superconducting state to Ohmic state. b) Extracted steps from the IV curves (small solid data points, peak number shown in colour) and peaks extracted from AC OMR data in the same sample under the same conditions (AC data from Fig. 4.10 is shown as open symbols). Note: The peak order, n, for AC and DC are in reverse order due to extraction techniques. c) Applied magnetic field and step current product vs applied magnetic field. d) The magnetic field that resulting in a step at 50 μA and the centre peak fields from AC MR measurements at 50 μA. DC data points are shown using a solid symbol and a line extending towards DC (0 Hz).
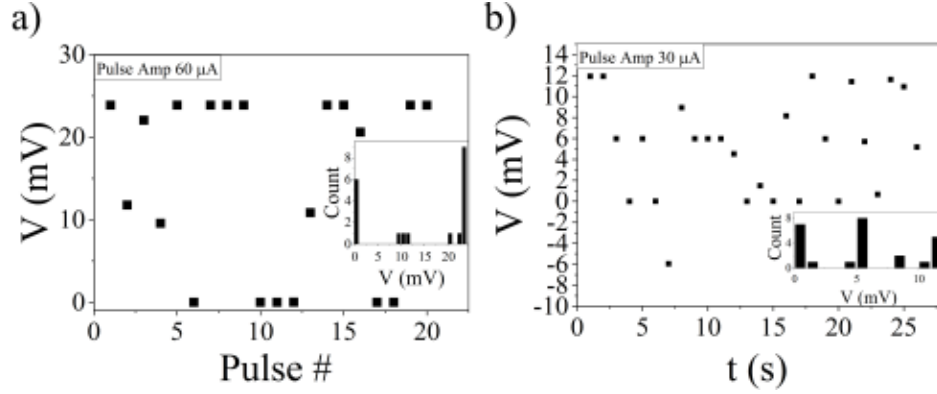
Figure 4.22: Pulsed IV measurement repeats a) Voltage measured for a series of 20 current pulses of amplitude 60 μA shown against the pulse number at a field of 4 T, the inset is a histogram of the data. b) Voltage measured for a series of 27 pulses of amplitude 30 μA shown against the time since measurement start at a field of 4 T, the inset is a histogram of the data.

Anderson-Kim flux creep at low $\mu_0 H$, to a strongly interacting, highly mobile lattice at high $\mu_0 H$.

Another relevant comparison with the AC OMR, is to compare the IV steps and AC OMR $\mu_0 H_{Peak}$ values. From Fig. 4.21 (d), it can be seen that the magnetic fields applied to cause an IV step at 50 μA and the AC OMR peak fields at 50 μA correspond to very similar values. We can conclude that when sweeping the field and measuring the AC MR, the measurement is probing an average of this voltage jumping that can be probed using DC pulses. This corroborates with the DC MR, where a scatter of resistance values can be averaged to generate a curve approximating to the AC signal.

To confirm the probabilistic nature of the resistive events, DC pulsed measurements were taken at a fixed value of I_{pulse} and $\mu_0 H$. Figs. 4.22 (a) and (b) show the results for this. Fig. 4.21 (a) is a single measurement with 20 consecutive current pulses of 60 μA at 4 T applied field. The voltages appear to occur in bundles of two or three and have a n amplitude that varies between a maximum resistance and zero resistance. This rapid probing technique demonstrates that the system changes on a similar scale to the resolution of the pulse probe ~100 ms. It also shows that the voltage is more likely to be at extreme values, but can be measured at some intermediate values. The pulse probe could trigger a vortex motion and rearrangement event, by both applying a Lorentz force and disruption the edge barriers. The intermediate voltages are potentially probed when the resistive event is in the process of initiating or ending. The intermediate values could also arise from smaller events that do not generate the maximum voltage. Fig. 4.21 (b) is essentially the same as (a), however, a time delay of 1 s was added between pulses. The current pulse amplitude is also halved. The time scale is now longer than the event time scale, giving the system time to relax to a stable state. There is less bundling of data point and a greater spread of values between the maximum and minimum. This is confirmed in histograms of the voltage values, as seen in the insets. Certain current values have a greater amount of stepping than others, resulting in a different spread of voltages. Unlike the DC MR, there are no negative voltages observed. This is simply due to the fact that the

pulsed currents rapidly exceed the current amplitude used in the DC MR measurements. The large pulse provides directionality to the voltage through the Lorentz force. Only at low current densities might a negative voltage be expected.

Further to the depth of understanding available in the discussion of Fig. 4.21, three more samples have been studied from which supporting comments can be made. The results for these samples in shown in Fig. 4.23. Presented here is a reference AC MR, pulsed IV measurements, and extracted I_{step} values at two temperatures, for three samples. This shows that in agreement with Fig. 4.21, there are steps and jumps in the IV curves when an OMR is observed. Also, no steps are observed when there is no significant OMR. For the first two samples, the extracted I_{step} appears to have a qualitatively similar dependence on $\mu_0 H$, with more steps occurring at lower $\mu_0 H$/ higher I_{step}. The steps merge into one critical current at higher fields/ lower currents, as seen in Fig. 4.23 (c) and (f). For the samples shown in Fig. 4.23 (g-i) the AC MR data shows a small kink in the resistance which could be OMR, but is not significant. As the OMR is not clear, the pulsed IV curves show a simple transition from superconducting to Ohmic without steps. The IV slope smoothly transitions from the superconducting state to the normal state

In summary, the pulsed IV measurements contain stepping and jumping at applied current and magnetic field values that correspond to the OMR observations. The pulses probe the OMR effect in a novel way, with the evidence supporting the conclusion of the AC and DC OMR observations. The pulse probes the voltage due to the probabilistic motion of vortices, yielding unstable ranges of applied current and magnetic field.

4.4   Conclusion

Three main techniques have been utilised to probe the OMR in Nb nanowires defined by optical lithography: AC MR, DC MR, and pulsed IVs. All three techniques have proved to be comparable by the existence of events at particular magnetic field values. These events appear in the form of Gaussian peaks in the MR or stepping and jumping in pulsed IVs. Comparison of the techniques using the values of magnetic field is relatively simple. If there are events at similar values of magnetic field then the events are most likely from the same physical source. Comparison using the magnitude of each event is not as straightforward. In the case of AC OMR, after background removal, the data can be broken down into an in phase, resistance and an out of phase, reactance component. Both components are in the form of a series of n Gaussian peaks, centred at $\mu_0 H_{Peak}(n)$. In the case of DC MR the resistance is scattered to both positive and negative resistance values. By taking the average of the absolute value, a curve approximating to the AC MR can be reconstructed. Scattering in DC MR could occur due to changes on the time scale of a single measurement. In AC MR this scattering is averaged out over the ~100 current cycles. The AC MR and DC MR magnitude, encapsulated in the peak resistivity, does not have the same dependence on the applied current amplitude. This means that the measured OMR magnitude differs depending on the measurement technique. The DC OMR peaks are extracted without averaging, and so the discrepancy could arise due to the variation in voltage observed in DC at low applied current amplitudes. The variations are only observed in DC, and could inflate the measured peak resistivity at low current. Throughout this study the extracted OMR peaks have a maximum resistivity in the
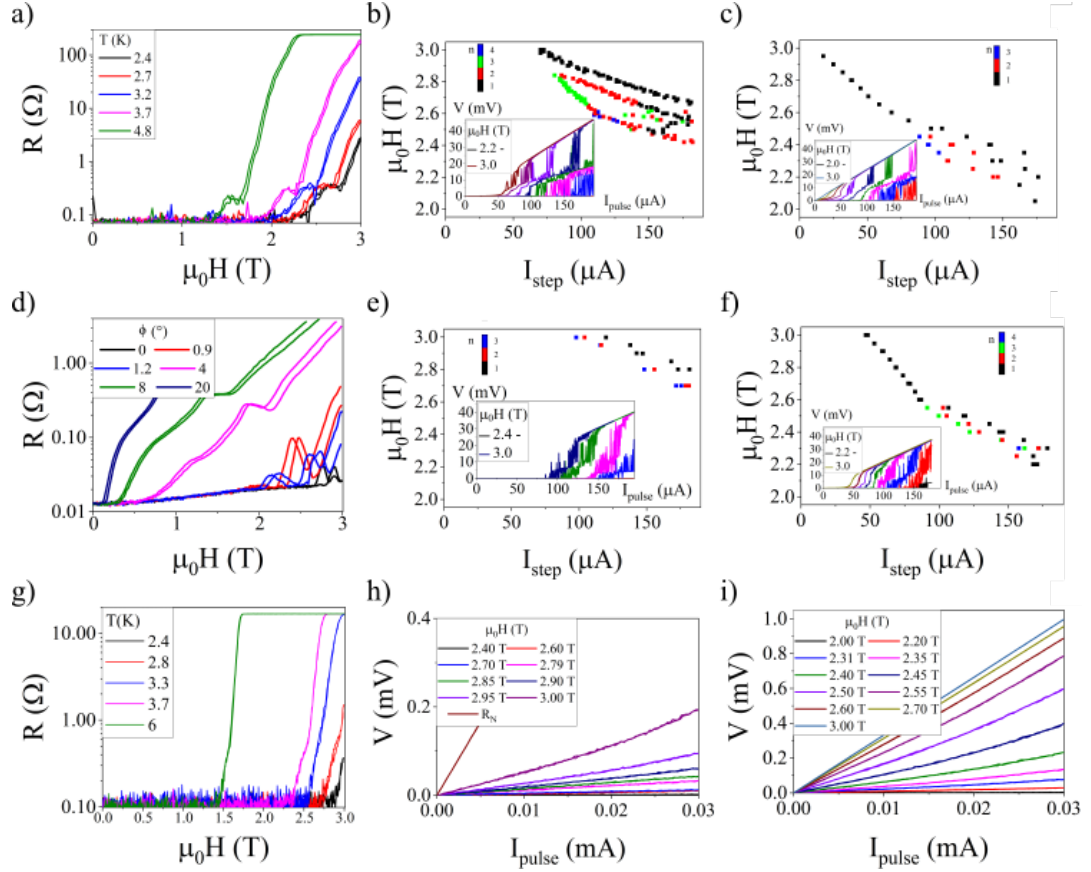
Figure 4.23: Supporting information showing pulsed IVs in 3 samples. a)-c) Nb nanowire, thickness = 40 nm, width = 0.8 μm, length = 33 μm, T_c = (6.2 ± 0.1) K. Orientation is in plane, transverse. a) Temperature varied AC MR for reference. b) and c) Extracted steps from pulsed IVs, step number shown in colour. IVs are shown in insets with magnetic field, ranging from superconducting to Ohmic behaviour. Temperatures are 2.7 K and 3.5 K for b) and c) respectively. d)-f) Nb nanowire, thickness = 30 nm, width = 1.4 μm, length = 33 μm, T_c = (5.3 ± 0.2) K. d) AC MR for a transverse, in plane to out of plane rotation, small ϕ variation. A small amount of hysteresis is observed, this is simply due to a small temperature shift. e) and f) Extracted steps, from (d), step number shown in colour. IVs are shown in insets with magnetic field, ranging from superconducting to Ohmic behaviour. Temperatures are 3.0 K and 3.5 K for e) and f) respectively. g)-i) Nb nanowire, thickness = 60 nm, width = 1 μm, length = 14.8 μm, T_c = (8.1 ± 0.1) K. g) Temperature varied AC MR for reference, orientation is in plane, transverse. h) and i) Pulsed IVs at several magnetic field values, showing superconducting to Ohmic behaviour. Magnetic field orientation for h) is in plane, transverse and i) out of plane, transverse. No steps are observed in this sample under any conditions.

range $\rho_{Peak} \sim 30\mu\Omega cm$. As the data shows, the OMR can be negligibly small, as environmental parameters diminish resistive causes. The similarity of the OMR magnitude range supports the conclusion that both techniques are probing the same resistive mechanism. There are no quantifiable OMR magnitude parameters available in the pulsed IV probe, and so this cannot be included in discussions of power losses due to the OMR effect. In summary, this chapter has shown that the different techniques each have their own merit, but are most powerful when used in conjunction with one another to build a picture of the OMR effect.

In many of the potential mechanisms for OMR, the orientation of the applied magnetic field relative to the sample and current direction is key. In spite of that, it is something that few studies have investigated. The evidence presented here shows that the OMR effect is not intrinsically dependent upon the orientation of the magnetic field. There do appear to be limits on the sample dimensions, above which OMR is not clearly observed. If the magnetic field is incident on a sample such that the dimensions facing the flux are large the resistance is dominated by a monotonic background. The limiting cases of this being a large bulk sample or out of plane of a thin film. This study suggests that the requirement to observe OMR is limited by the thickness and width of the sample. This study has observed OMR in samples with 10s of nm thickness and micron widths. The largest OMR has been observed for a magnetic field applied in plane to the thinnest samples. Hence it can be postulated that the OMR may be observed when a nanowire has dimensions of the scale of the superconducting parameters. If either the width or the thickness exceed a limit, the OMR effect becomes more difficult to observe. This limit is not well defined by this study, although the wires exhibiting OMR are below the limit. The length of the voltage probe is typically not relevant to the intrinsic OMR, but can affect the OMR when the effect becomes mixed with the background resistance. A background resistance signifies that sections of the nanowire have become normal, changing the shape of the superconducting sections. As we have already outlined the shape of the nanowire has great influence on the OMR effect. In summary, the evidence presented in this chapter makes some progress in understanding the influence of sample size and magnetic field orientation on the OMR effect, but cannot provide a comprehensive understanding with exact limits.

Quantum interference effects cannot cause the OMR observed. The measured periodicity would require SQUID loops or Little-Parks cylinders that are unlikely to be able to form. The angular dependence of the periodicity also dismisses quantum interference explanations, as the effect is strong when the applied magnetic field and current are parallel. This is impossible for both the SQUID and Little-Parks effect. The pulsed IV characteristics show that the OMR effect observed in these Nb nanowires is not caused by a Weber blockade type effect, as the distinct zig-zag trend in the critical current is not observed. The evidence presented suggests that the periodic motion of vortices is the main mechanism for the OMR in these Nb nanowires. The periodic voltage being both from the rearrangement of the vortex lattice and from the flow of vortices across the nanowire. The rearrangement of the vortex lattice being predominantly controlled by the vortex density, packing, and ordering. The vortex density is mostly dependent on the applied magnetic field. The flow of vortices is primarily controlled by the Lorentz force on the vortices, which is proportional to the current-magnetic field product. DC constant current and pulsed IV measurements detect a time varying voltage, signifying that the vortex motion is probabilistic. Observations show that the OMR voltage is not always generated in phase with the AC probe. In DC this can manifest as a negative voltage. These two observations

can only occur if the vortex rearrangement is not coupled perfectly to the driving current. For instance, in the AC case, the rearrangement could lag behind the driving frequency. In summary, the periodic motion of vortices is considered to be the principle mechanism that drives the OMR and associated effects.

The overarching trends uncover the OMR process as a probabilistic event with a time scale of the order of 1 s. The evidence suggests that the events occur due to vortex lattice rearrangement which can be triggered when the Lorentz force becomes large enough. The Lorentz force, vortex interaction, and entry and barriers are modulated by the temperature, the AC amplitude, and the AC frequency. From the periodicity of the OMR, it can be postulated that the entry and exit energy barriers and vortex rearrangement energy barriers are semi-periodic with the applied magnetic field. The exact periodicity must depend upon macroscopic details of the sample topography and the microscopic structure of the material. In the AC OMR effect, when $f_{app} \gg MHz$, $I_{app} \ll I_{crit}$ and $T \ll T_c$ the OMR magnitude is reduced, with the appearance of superconductivity to higher magnetic fields. When $f \sim 1 Hz$, $I \sim I_{crit}$ and $T \sim T_c$ the OMR smoothly connects to a monotonic background resistance, becoming the normal state resistance. At the limit of OMR reducing to be negligible, there could be two reasons. Firstly, the case where the Lorentz force, in addition to thermal excitations, is too small to cause the collective motion of vortices. Or secondly, the case that the driving force is at too high a frequency to force the vortices from their pinned, metastable lattice sites, and the lattice simply vibrates with a negligible amplitude unable to displace and rearrange. At the limit of OMR, before become the normal state, the Lorentz force is large and near the resonant frequency of the vortex motion. This situation easily drives the vortex lattice alternately across the sample generating a large amount of resistance. The vortex pinning processes becomes ineffective. As the vortex population fills the sample volume, the vortex motion induced resistance connects smoothly to the normal state, which is in effect a fully packed and fully mobile vortex lattice.

CHAPTER 5

Superconducting In-SnTe Nanowires

Having investigated vortex motion in sputter grown Nb nanowires, our attention now turns to a lesser studied material, In doped SnTe. As described in Chapter 2, In-SnTe is a superconducting topological crystalline insulator and candidate topological superconductor. Vortices in topological superconductors may have the capacity to stabilise Majorana fermion zero modes, which have potential uses in topological quantum computing. In-SnTe is the only topological material to be fabricated into superconducting nanowires, without patterning or use of a proximity effect [147]. Nanowires of topological superconductors are important as they will make up the building blocks of topological computing devices. The study of In-SnTe nanowires is important to the field of topological devices.

A large section of this chapter is devoted to the general characterisation of this material. This includes the growth of nanowires using vapour transport growth without Au nanoparticle catalysts, and the contamination observed when Au nanoparticles were used. Problems discovered due to fabrication issues and the fragility of the In-SnTe crystals are discussed. Thermal cycling of the samples caused degradation and cracks, evidence of these problems is presented. Due to the damage inflicted on samples by simple measurement procedures, most samples could not be reliably measured in multiple orientations. As such, observations are made through comparison of data from different samples.

Following the assurance of the quality of the In-SnTe nanowires, observations and analysis of the OMR observed is given with reference and comparison to the study using Nb nanowires. Following the methods used to analyse OMR in Nb, the temperature, AC amplitude, AC frequency and magnetic field orientation are investigated. The aim of this chapter is to begin to provide a method of probing the state of the vortices, which would be used to manipulate Majorana fermions. It is found that the nature of the OMR in these In-SnTe nanowires is more problematic to analyse than in the Nb nanowires grown by DC sputter deposition.

This chapter presents an inconclusive picture of OMR. Comparisons are drawn with the clear observations from the Nb nanowires. Fewer pieces of complimentary evidence are available to examine the origin of the OMR. The OMR is analysed from the perspective that the Nb nanowires were more suited to studying the intrinsic OMR effect, and so it is assumed that the OMR in these samples is altered by extrinsic effects.

In addition to the superconducting MR, the normal state MR also has an interesting feature in the form of weak anti-localisation. This is one element of proof that the topological crystalline insulator surface states exist, and as such there is potential that in the superconducting state, the In-SnTe studied here is topological in nature.

This chapter begins with the discovery of Au contamination in the VTG method used to grow the In-SnTe. This is followed by a brief overview of the synthesis of In-SnTe nanowires with radii on the scale of 100 nm grown without a Au catalyst. Detailed experimental details are covered in Chapter 3.

5.1 Vapour Transport Growth

Vapour transport growths were initially performed in a temperature gradient of ~1 °C/cm, this yielded growths of predominately plate shaped nano-objects. Nanoplates of superconducting In-SnTe have been studied in previous literature [77, 84]. The path to novel understanding is
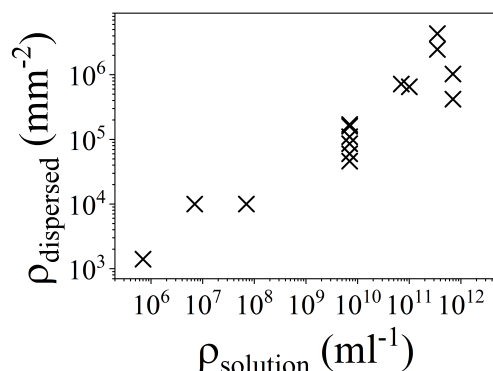
Figure 5.1: The relationship between the density of GNPs in solution to the density of GNPs dispersed.

to further reduce the bulk contribution using nanowires. Two options are available to confine the dimensionality of the growths, adjust the growth parameters by trial and error, maximising long thin growths; or use a growth enhancing catalyst. Trial and error is a lengthy process with no guaranteed results, and so Au nanoparticles were employed as an intended growth catalyst. This method has been used to grown nanowires of both SnTe and In-SnTe [56, 79, 80, 86]. The use of the catalyst gave an unexpected result. The work is published by Sam Atherton, the author and Dr Satoshi Sasaki [3]. The discovery is explained in the following section.

5.1.1 Au Nanoparticle Dispersion and Heat Treatment

An optimum density and dispersion of nanoparticles is required to have a successful growth of nanowires. The ideal case is to have a similar density of GNPs to the density of nano-objects in a typical growth. Fig. 5.1 shows the relationship between the solution density and the dispersed GNP density. The later was measured by counting the number of GNPs per area in SEM images. The density of dispersed GNPs chosen for use in the VTGs was such that there should be approximately one GNP per crystal growth, assuming the growth density would not change with the presence of nanoparticles. At high dispersion densities the GNP cluster together, which can only act as a nucleation point, not to assist nanowire growth. Evidence for clustering is shown in Fig. 5.2 (a).

Prior to using GNP for a growth, GNP dispersed on a Si substrate went through the VTG procedure without a source material. Through this methodology the effect of heating the GNP can be found. It is expected that in order to facilitate the growth of In-SnTe nanowires the nanoparticles must be in the liquid phase during VTG. GNPs were imaged before and after the mock VTG growth using high resolution SEM. As shown in Fig. 5.2 (b) and (c), GNP were observed to be rounded after the mock VTG. The facets of the GNP are not as clearly defined after heating. The clusters of GNPs, as shown in Fig. 5.2 (a), we observed to melt together, forming a large particle. A required for catalyst enhanced, vapour-liquid-solid growth. The GNPs are in a liquid phase at the temperatures required for VTG.
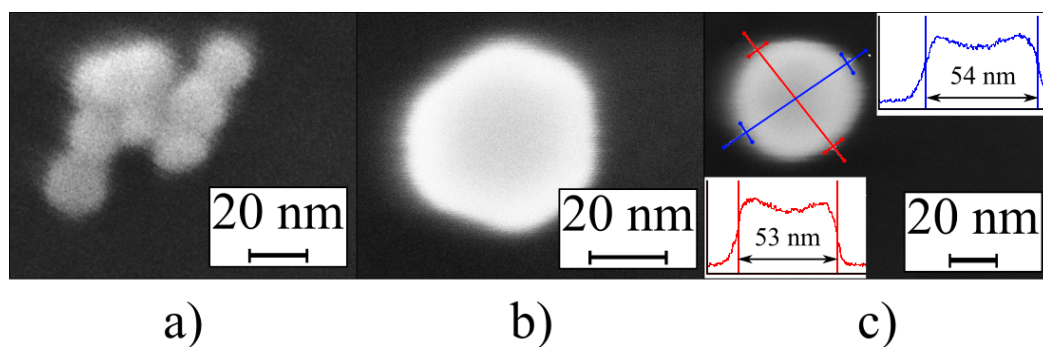
Figure 5.2: SEM evidence of clustering and melting of GNPs. a) 20 nm diameter GNPs dispersed from a high density solution. Clusters of ~20 particles were observed. b) A single 50 nm GNP with clear facets. c) A single 50 nm GNP after heating to 600 °C in a VTG process without any In-SnTe. The facets are smoothed, yet the radius is the same.
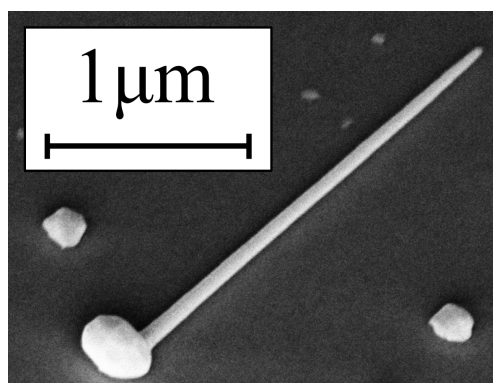
Figure 5.3: SEM topography image of a VTG object grown with 20 nm GNP dispersed on the substrate. This sample shows that nanowires can be grown with GNPs present.
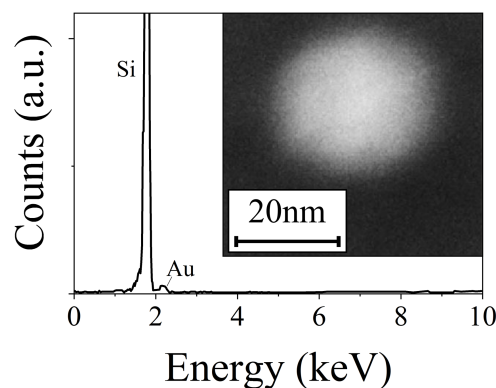
Figure 5.4: EDX Spectrum for a single 20 nm diameter GNP on a Si substrate. Inset shows a topographical SEM of the same GNP.

5.1.2 Crystal Contamination

VTG crystals were observed to grow where GNP were dispersed, however only a small number of GNP assisted VTG growths yielded any nanowire-like objects. One such example is shown in Fig. 5.3. The GNP assisted growths resulted in the same thick nanoplates that were observed without a catalyst. The GNPs were not behaving as expected in a vapour-liquid-solid catalyst assisted growth. To better understand the mechanism of growth from the GNP site and the uniformity of the growth, EDX elemental mapping was employed. As explained in Chapter 3, EDX is not a quantitative measure of the elemental composition of a material. The technique provides a qualitative, relative measure of the composition. By scanning the measurement across the sample, a two-dimensional relative composition map can be constructed. In this study, the elements observed include In, Sn, Te, and Au from the GNPs.

An individual GNP is a relatively small object. Before proceeding with a discussion of the observation of Au in EDX spectra, it must first be shown that a single GNP can be observed by the EDX instrument. Fig. 5.4 shows the EDX spectra for a single nanoparticle. The probe area was checked to ensure that this was the only GNP in the range of the instrument. The EDX instrument is capable of observing a single nanoparticle in the field of view. The GNP measured is shown in the inset.

Upon EDX examination of a VTG crystal grown onto a substrate with GNP dispersed, it was found that the Sn, In and Te were dispersed evenly throughout the crystal. Unexpectedly Au was spread across regions of the crystal, not localised at a single point. A peak is observed in the EDX spectrum at 2.12 keV, the characteristic x-ray photon energy for Au. This is shown in Fig. 5.5 (a), with an SEM image of the nanoplate studied. Fig. 5.5 (b) shows a colour map of the In-SnTe crystal, where the intensity of colour represents the intensity of characteristic x-rays for the elements Sn, In, Te and Au. Sn, In and Te have a uniform intensity. In appears lower in intensity, qualitatively this is expected from the lower concentration of the element in the crystals. Au appears in patches of the nanoplate. This shows that the Au peak registered in the EDX spectra is observed to be spread across the sample. To show that the Au is not simply registered due to the noise of the instrument, a sample grown without GNP is shown in 5.5 (c). In this case there is no Au signal in the nano-crystals. This evidence shows that GNP do not
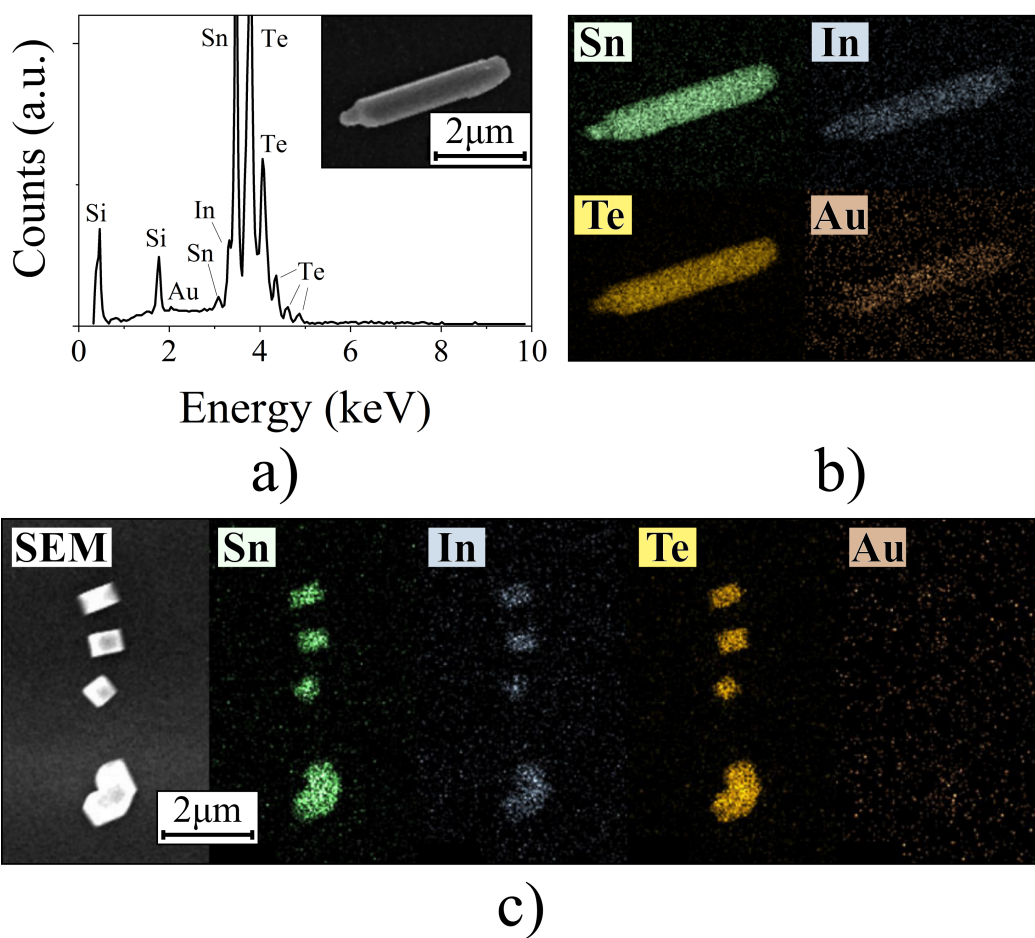
Figure 5.5: The EDX spectrum from point analysis of an In-SnTe crystal grown using 20 nm GNP. The inset shows a topographical SEM of the sample. b) EDX elemental colour maps of the VTG In-SnTe crystal, for which the EDX spectrum is shown in (a). c) SEM and EDX elemental colour maps of VTG In-SnTe crystals, grown without GNP on the substrate. No Au is observed.
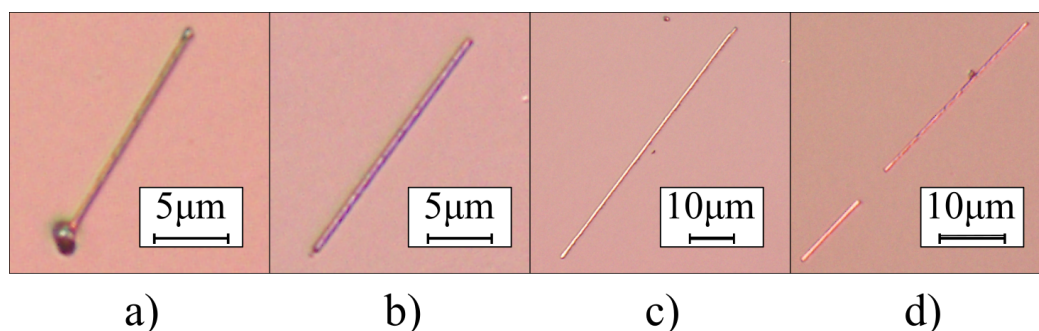
Figure 5.6: Optical microscope images of a selection of successfully grown nanowires, using VTG without a catalyst. a) t = 200 nm, w = 250 nm, l = 16.7 μm. b) t = 330 nm, w = 300 nm, l = 20.9 μm. c) t = 100 nm, w = 470 nm, l = 58.3 μm. d) t = 50 nm, w = 350 nm, l = 31.3 μm.

act as growth defining catalysts, in this VTG procedure. Instead they alloy with the deposited material. Future studies of nanoparticle enhanced nanowire growth should take special care that the catalysts are not contaminating the growth.

5.1.3 Successful Nanowire Growths

Trial and error is a time consuming process to try to obtain a particular crystal formation. Crystal nucleation is a fundamentally stochastic process. However, it is imperative to minimise contamination. Using statistical optimisation of growth parameters, a process was created that could yield nanowires of the radius required, $\sim 100nm$. Optical images of four example nanowires are shown in Fig. 5.6. Considering that these crystals were grown without the use of a catalyst the ratio of the length to thickness and length to width is incredibly large. The uniformity in width can be observed through the optical images. Fig. 5.6 (c) shows a particularly well formed nanowire with a smooth flat top surface, indicated by the uniformity of the reflection of the microscope light.

5.2 In-SnTe Crystal Characterisation

Initial characterisation of substrates formed in the VTG process was conducted using an optical microscope. Well formed crystals were identified, with a particular emphasis on long thin objects. The thickness of the objects at this point could be estimated using the distortion of the covering resist layer. Very thick nano-objects could be seen to break out above the ~1 μm resist layer. Samples thicker than the resist layer are not suitable for patterning contacts and are not nanowires. Lateral dimensions were measured using an optical microscope with a calibrated length scale, to a precision of ~0.1 μm.

5.2.1 Electrical Contacts and Exploding Devices

During the development of nano-patterning processes, the contact resistance was initially observed to be high, ~ 1 kΩ. This produced noise in measurements and caused large Joule heating localised at the small contact areas. These contact points had a tendency to explode during electrical measurements. Due to the high resistance, many of the initial samples gradually stopped working during transport measurements. Under SEM examination it became clear that the contact resistances were causing material to melt, evaporate or sublimate. Fig. 5.7 shows a selection of eventful sample failures. Panels (a), (b) and (d) show complete sample destruction, which could be caused by experimental errors. However, panels (c) and (e) show that the heating is localised at the contact areas. Contact heating is high when the contact area is small. This is due to the high resistance of the contact and the small volume over which the high Joule heating power is dispersed. Heat can rapidly deform and melt these points, increasing the resistance and causing a runaway contact destruction process. The resistance across a junction, such as between electrical contacts and a sample, has a fixed resistance-area product. To reduce the resistance, the area of the contact must be increased. Following some catastrophic device failures, the contact patterning process was altered to include an Ar milling and sputter step, which removed residual resist from the crystal walls. Angled thermal evaporation was used to overcome self-shadowing, which is explained fully in Section 3.1.3.3.

In addition to the developments required in the contact making procedure, very thin wires were prone to developing nanoscale breakages as evidenced in Fig. 5.8. These samples were observed to have a sudden increase in resistivity during measurements. Often one or two thermal cycles was enough to cause damage. The increase in resistance at a crack point could cause a runaway destructive, melting process. This is the most likely explanation for nanowire sample destruction, the likes of which can be seen in Fig. 5.7 (d).

Despite the issues experienced, samples were able to be fabricated and some measurements taken. Unfortunately, due to the short lifetime of samples and the inability to repeat thermal cycling, complete sets of measurements on any particular sample were impossible to achieve. General trends and cross comparisons allow a general study of the properties of In-SnTe superconducting nanowires. Optical microscope images of successfully contacted In-SnTe nanowires are shown in Fig. 5.9.

5.2.2 Superconductivity and Transport Properties

5.2.2.1 Superconducting properties

Example normalised resistance versus temperature characteristics are given for a selection of ten In-SnTe nano-objects are given in Fig. 5.10 (a). There is some difficulty in determining the exact resistivity of most of the In-SnTe samples due to the non-uniform shape. In addition, SEM images could only be taken after measurements, when many samples were no longer intact. Fig. 5.10 (a) shows the superconducting transition and normal state behaviour. The resistance vs temperature profile is typical for a metal, which is appropriate for this doped narrow bandgap semiconductor. Conversely to the Nb nanowires studied in the previous chapter, the critical temperature and residual resistivity ratio have a negative relationship, as shown in Fig. 5.10 (b). This difference can be understood through the In dopant level, x,
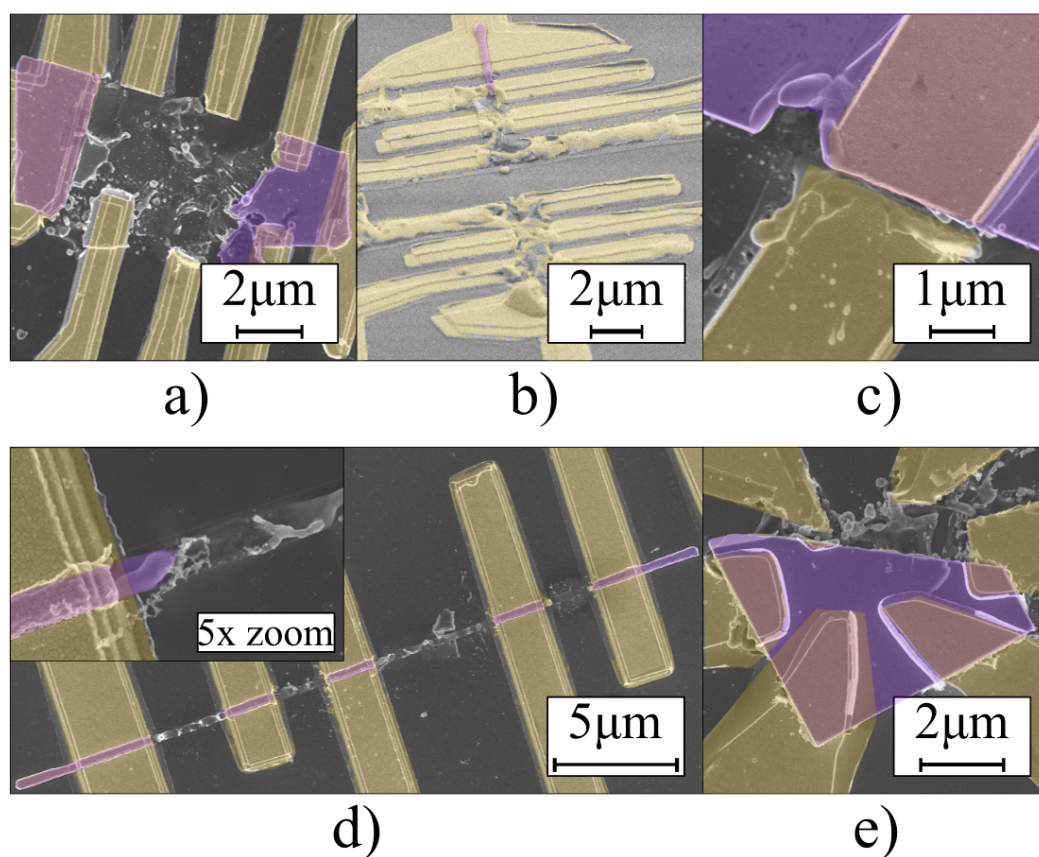
Figure 5.7: SEM images showing dramatic examples of In-SnTe devices that were destroyed during measurements. Images are coloured, In-SnTe in magenta and Au in yellow. a) A nanoplate nearly fully removed. b) A destroyed 100 nm thick nanowire. c) Evidence that the contact areas can cause high resistance and Joule heating. d) A 40 nm nanowire that has exploded but not due to the contacts, which appear to be intact. e) Evidence that the contact areas can be the cause of the high resistance and Joule heating.
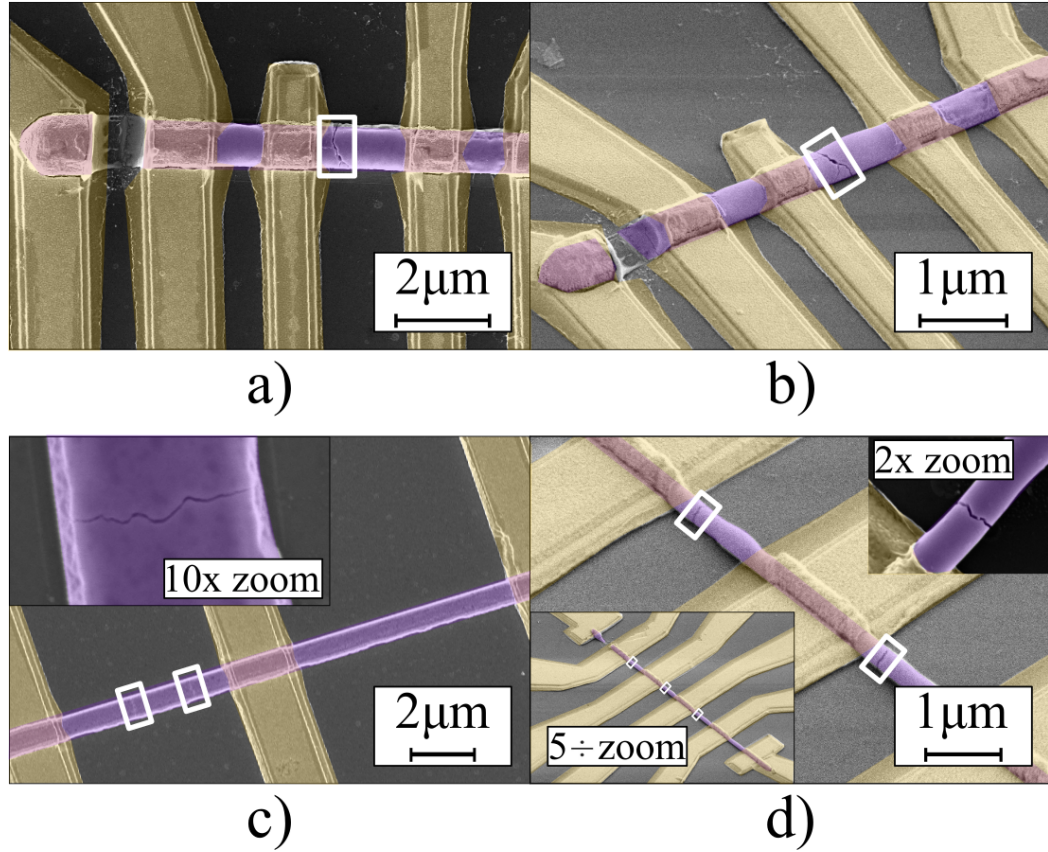
Figure 5.8: SEM images showing examples of nanowires with cracks highlighted by boxes. Images are coloured, In-SnTe in magenta and Au in yellow. a) and b) A nanowire with a melted section and a crack, thickness ~300 nm. c) A 200 nm thick nanowire with several cracks along the length. Inset, 10× scale magnification. d) A 300 nm thick nanowire with several cracks along the length. Upper right inset, 2× scale magnification. Lower left inset, 5× scale reduction.
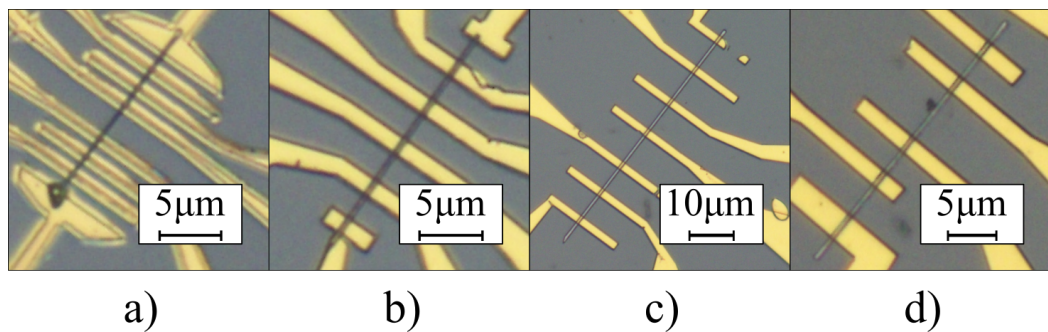
Figure 5.9: Optical microscope images of a selection of nanowires with patterned contacts. a) t = 200 nm, w = 250 nm, l = 16.7 μm. b) t = 330 nm, w = 300 nm, l = 20.9 μm. c) t = 200 nm, w = 700 nm, l = 64.3 μm. d) t = 50 nm, w = 350 nm, l = 31.3 μm.
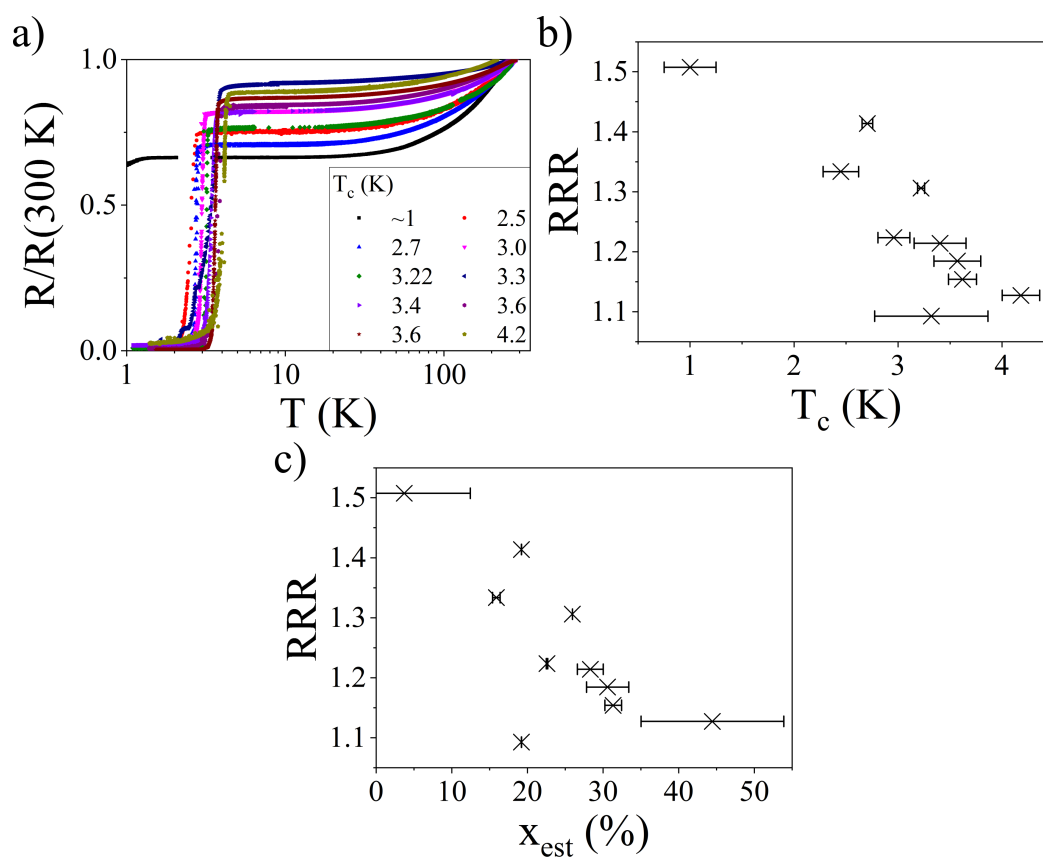
Figure 5.10: Resistance vs temperature for ten In-SnTe nano-objects. a) Resistance normalised to R(300 K) vs temperature. b) Residual resistivity ratio vs superconducting critical temperature. c) Residual resistivity ratio vs estimated Indium dopant level.

which is shown to have a negative relationship with RRR in Fig. 5.10. RRR decreases at higher dopant levels as the In doping increases the carrier density and introduces disorder in the lattice. This have the effect of increasing the intrinsic scattering rate and this in turn raises the low temperature residual resistivity. A similar trend has been reported before in bulk crystals [148]. This study have a larger sample count than presented previously, showing the clear relationship between the In dopant level and the RRR. As the dopant concentration nears x = 50%, the RRR tends to 1. A RRR of 1 signifies that the intrinsic scattering from dislocations is more dominant than the temperature dependent phonon scattering, which makes a very poor conductor.

The dopant level is estimated by comparison with bulk data from Zhong *et al.* [149], where the critical temperature is seen to be correlated with the dopant level. This is shown in Fig. 5.11 (a). Fig. 5.11 (b) shows a spread in the estimated In doping level, x_{est}, relative to the initial VTG source concentration, x_{source}. The range of dopant concentrations in each growth is caused by the different throwing distances of In and SnTe. VTG relies upon a temperature gradient to transport the material, and each constituent will aggregate and deposit when it reaches the saturation vapour pressure. In and SnTe have different saturation vapour pressures by a margin of 20% [123, 124]. Consequently there is a spatial dependency on the dopant level in VTG crystals. Fig. 5.11 (c) shows the spatial dependency can be modelled as an exponential decay for a set of three crystals measured on the same substrate, where the position of the source and samples was well known. The exponential fit predicts the source dopant level to be correct at $x_{source} \sim 20\%$.

In addition to the effect on resistivity, disorder from increased doping influences the coherence length through Pippards reduction, Eq. 2.7. A reduction in the normal state mean free path has the effect of increasing the intrinsic resistivity and reducing the superconducting coherence length. While the doping increases the critical temperature, it also reduces the coherence length through the increased disorder. Fig. 5.12 shows that, while there is generally a small amount of variation in the coherence length, samples with a higher dopant concentration and higher critical temperature have a smaller coherence length.

MR for a selection of nanowires is shown in Fig. 5.13 (a-c). The three cases shown have three clear features. (a) and (c) show a large suppression of resistivity at the lowest temperatures, this is clearly the superconducting phase, which is discussed in detail in a later section. The normal state behaviour has two contributions to the resistivity. At temperatures T_c < T < 10 K there is a small dip in resistivity, which is attributed to the weak anti-localisation effect. The WAL is examined in detail towards the end of this chapter. The remaining MR appears to be linear and negative up to 8 T, the MR gradient $\Delta R/R \sim -10^{-4}T^{-1}$. Negative MR is quite unusual, and is not expected for In-SnTe. The negative MR could be an experimental artefact, although a thorough investigation would be required to clarify this. Fig. 5.13 (d) shows the MR for a nanoplate, which is similar to the MR for the nanowires, except that the high field MR is positive. The MR gradient is comparable in magnitude $\Delta R/R \sim 6 \times 10^{-4}T^{-1}$. Panel (e) shows the Hall resistance for the same plate. The noise to signal ratio in the measurement appears large. The Hall signal was small and there was a large R_{xx} component that dominated the measurement. Ideally a Hall bar geometry would be used to measure the Hall effect, for the lithographic resolution and this size of nanowire a Hall bar geometry is not possible. The R_{xy} component was extracted by taking the asymmetric component of the signal. In-SnTe is a doped narrow bandgap
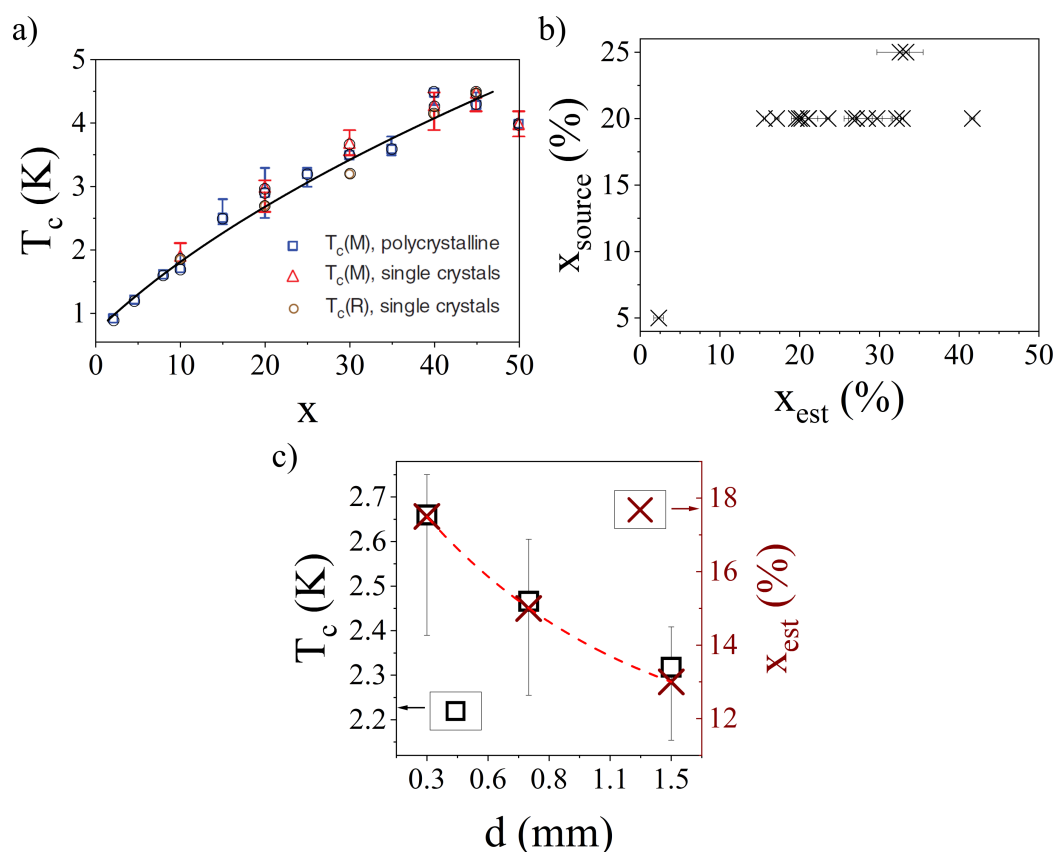
Figure 5.11: Estimation of the dopant level, *x*, inside the VTG nanowires. a) A quadratic fit to data taken from Zhong *et al*. [149] is used to estimate the dopant percentage from the measured T_c. b) A comparison of the estimated dopant level and the dopant level in the source material used to grow the samples. c) Critical temperature and estimated dopant level vs the distance between the source and three grown crystals. The exponential decay predicts the dopant level at the source to be 19.1%, in good agreement with the actual source dopant level of 20%.
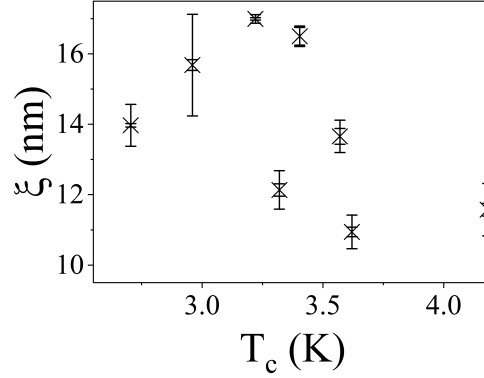
Figure 5.12: The coherence length vs RRR for a selection of In-SnTe nanowires. Coherence length estimated using the Werthamer, Helfand and Hohenberg equation, Eq. 4.1, and the definition of $\mu_0 H_{c2}$.

semiconductor. It is expected that both n and p type carriers should contribute to the transport and so the Hall resistance would ideally be interpreted using a two-band model. As the Hall signal is small, and the noise large, this analysis is not possible and leads to spurious results. An estimate of the carrier density can be made using the single-band model, assuming one carrier type dominates. From the equation for the Hall resistance with a single carrier type, the carrier density is given by, $n = \frac{\mu_0 H}{R_{xy} e d}$, where R_{xy} is the transverse resistance and d is the sample thickness. The gradient of the Hall MR is $\frac{R_{xy}}{\mu_0 H}$, hence the carrier density can be estimated form the Hall resistance. From this nanoplate, the carrier density is found to be $n = -(11 \pm 6) \times 10^{22} cm^{-3}$. This is negative carrier density, which is surprising given that the In doping provides p-type carriers. However, in a previous study by Zhang *et al*. [150] In-SnTe was observed to have a cross over between p-type and n-type dominated bulk transport at a dopant level of $x_{source} \sim 25\%$. The nanoplate studied here has a critical temperature of $3.22 \pm 0.03 K$, and an estimated Indium dopant level of 27%. This estimate puts the sample into the electron dominated regime. The conclusions of the previous study state that bulk Dirac-like hole pockets coexist alongside the dominant electron carrier density. The mixing of two carrier bands brings the nature of the superconductivity into question. Unfortunately, that is a question that cannot be answered here and is one of the many mysteries of In-SnTe.

5.3 Oscillatory Magnetoresistance in In-SnTe nanowires

OMR has not been reported in previous works involving magnetotransport measurements of In-SnTe nanowires. In the following section oscillations in the magnetic field induced superconducting transition of In-SnTe nanowires is presented. These oscillations are not caused by the surface states. Aharonov- Bohm and Shubnikov-de Haas oscillations are known to occur in the normal state MR of topological insulator materials. These effects are associated with the surface surfaces and have been observed in SnTe nanowires [56]. The oscillations presented here are not in the normal state, instead occurring exclusively in the superconducting transition. Due to the fragility of the samples to heat cycling, arguments are

Figure 5.13: MR for three In-SnTe nanowires and MR and Hall resistance for a In-SnTe nanoplate. The magnetic field orientation is out of the plane of the sample. a) Thickness = 0.2 μm, width = 0.7 μm, length = 7.2 μm. x_{est} = 20.1%. Inset shows normal state MR in more detail. b) Thickness = 0.1 μm, width = 0.61 μm, length = 2.1 μm. x_{est} = 25.5%. c) Thickness = 0.1 μm, width = 0.47 μm, length = 40 μm. x_{est} = 28.3%. Inset shows normal state MR in more detail. d) MR and e) Hall resistance for a sample with thickness = 0.15 μm, width = 10.2 μm, length = 5.91 μm. x_{est} = 26.0%. Inset of (d) shows normal state MR in more detail. The carrier density $n = -(11 \pm 6) \times 10^{22} cm^{-3}$ is calculated from the gradient of the Hall resistance.

constructed using measurements from several samples. The study has been limited by the stochastic nature of the growing procedure, and the varied dopant level between growths. Sample size, shape and dopant level can not be tightly controlled. Nevertheless, an attempt to find order in the chaos is made through comparison across the range of samples. Comparisons are also made with the OMR observations in Nb nanowires, studied in the previous chapter. For further detail into the analysis and parameter definitions see Section 4.3.1.

5.3.1 Oscillatory Magnetoresistance

Example observations and analysis are shown in Fig. 5.14 for a selection of four nanowires. Similarly to the Nb nanowires, the OMR signal can be fitted easily to a series of Gaussian peaks, signifying that the resistance is well described by a series of resistive events at specific magnetic fields. This gives a great starting point to begin comparison with the OMR observed in Nb nanowires. The OMR in these In-SnTe nanowires begins at a much lower field than the OMR in Nb nanowires, for the same in plane magnetic field orientation. In the periodic vortex motion model, this signifies that the vortex entry and exit barriers, and the pinning of the vortex lattice must be lower in the VTG crystals that the sputter grown Nb. It is expected that highly ordered VTG crystals should have a much lower density of pinning sites than sputtered material. The magnitude of the OMR effect, ρ_{Peak}, is comparable to that observed in typical Nb nanowires. This could be a coincidence, or it could signify that the intrinsic OMR magnitude is partially independent of the superconducting material properties. Observations of OMR in literature do not quote the OMR magnitude in terms of the resistivity, and so comparisons with other work is not practical. Fig. 5.14 (c) shows an OMR effect with a maximum at zero field. A negative OMR effect has already been observed in Nb nanowires. The zero magnetic field OMR maximum could result from the same mechanism as the negative OMR, reversing the effect of a residual resistance, at the base temperature of the system. The OMR maximum is reproduced in both positive and negative sweep directions, and so cannot be due to an offset from trapped flux in the cryostat superconducting magnets.

As discussed earlier in this chapter, the In-SnTe samples were generally fragile and highly susceptible to damage during measurements. While many samples have been measured, it is rare to have had the opportunity to measure a sample in multiple orientations. One such example is given in Fig. 5.15 for the sample labelled S1 in Fig. 5.14. Unlike the Nb nanowire samples, OMR is observed in all magnetic field orientations. This is likely to be due to the fundamental material differences between the Nb and In-SnTe samples. In-SnTe is expected to have a penetration depth ~ 5 times larger than that of Nb. This has the effect that the vortex influence range is longer, and so collective vortex behaviour should be possible for larger magnetic field facing dimensions. This is the case in the out of plane configuration. In Nb nanowires, the strongest OMR effect is observed for lower thickness values with an in plane magnetic field. In the case of S1, the thickness is a factor of four smaller than the width. This explains why the OMR effect is smaller in the out of plane orientation relative to the rapidly increasing background resistance.

All In-SnTe nanowires that had a high enough doping to observe zero or near zero resistance, at the obtainable temperatures, were accompanied by an OMR effect. What follows is a comparison of a select few nanowires, with a focus on the period or step size of the OMR effect and comparison with the Nb study where possible.
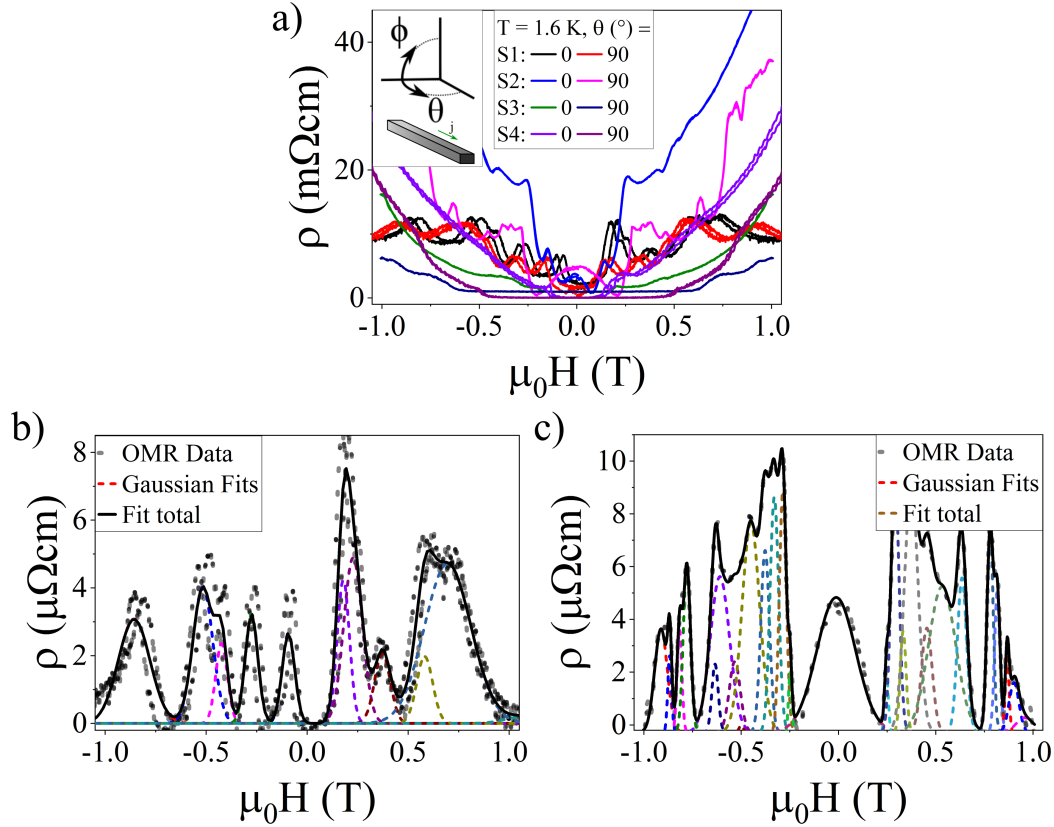
Figure 5.14: Examples of Gaussian Fitting to the OMR signal after a background subtraction a) Magnetoresistance for four samples in the in plane, transverse, $\theta = 0°$, and in plane, longitudinal, $\theta = 90°$, orientations. Temperature = 1.6 K. S1: thickness = 0.1 μm, width = 0.42 μm, length = 0.41 μm, $T_c = (3.6 \pm 0.2)$ K; S2: thickness = 0.1 μm, width = 0.21 μm, length = 7.6 μm, $T_c = (3.3 \pm 0.5)$ K; S3: thickness = 0.1 μm, width = 0.6 μm, length = 4.1 μm, $T_c = (3.1 \pm 0.1)$ K; S4: thickness = 0.3 μm, width = 0.74 μm, length = 8 μm, $T_c = (3.0 \pm 0.2)$ K. Angle θ is defined in the inset of (a), a replica of Fig. 3.11. b) Example Gaussian fitting of the OMR for S1 in (a) at 0° after background subtraction. c) Example Gaussian fitting of the OMR for S2 in (a) at 90° after background subtraction. During analysis the subtracted background resistance was taken as a smooth spline to points of minimum resistance.
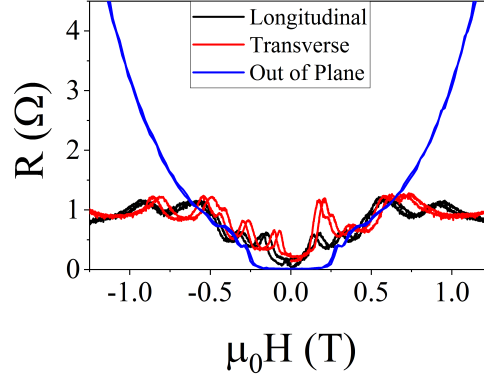
Figure 5.15: MR of sample S1 in three key magnetic field orientations, in plane longitudinal, in plane transverse and out of the plane. Thickness = 0.1 μm, width = 0.42 μm, length = 0.41 μm, T_c = (3.6 ± 0.2) K. OMR is observed in all configurations.

Fig. 5.16 shows the OMR for four samples at a temperature of 1.6 K. Results are shown for the in plane, transverse and longitudinal magnetic field orientation. In each case the OMR data and Gaussian fitting is given, as seen in panels (a), (d), (g), and (h). The extracted centre peak fields are given for the four samples in panels (b), (e) and (i). For samples S1 and S2 the centre peak fields are plotted against the peak order n and an adjusted peak order n'. By assuming that some peaks are missing in the longitudinal configuration ($\theta = 90°$) it is possible to make the step size between peaks approximately constant to extract an average period using a linear fit. The magnetic field step size between peaks for the adjusted peak number n' is given in panels (c) and (f). The step size is roughly constant for S1, and within the error appears to be unchanged between transverse and longitudinal orientations. The shifting of n to n' for S1 is shown in the inset of panel (c), peaks at $n' = 5, 7, 9, 10$ and 11 are assumed missing and there is an extra peak fitted at $n' = 3$. This extra peak field is highlighted in blue. For S2, the period can be made constant by the omission of certain peak orders in the longitudinal configuration, at $n' = 10, 14, 17$ and 18. The reason why the OMR might miss events in these nanowires is unclear. In the periodic vortex motion model, it could be related to the stability of the vortex lattice. If for particular arrangements of vortex rows there is a particular stability, the rearrangement and subsequent period of high resistance may not occur. Interestingly, for both S1 and S2 the OMR in the transverse configuration does not require this treatment to give a constant magnetic field step size between peaks. Unlike S1, the transverse configuration in S2 has a magnetic field step size, and average period three times greater than the longitudinal orientation. This difference here could be due to the different length to width ratios of the two samples. S1 has a contact separation length to sample width ratio ~ 1, while for S1 this ratio is ~ 36, this difference could cause a difference in the period under rotation, although this will be investigated further later in this section. S3 and S4 are included as examples of nanowires which show OMR, but have only a few peaks. S1 and S2 have 8 and 14 peaks in the longitudinal configuration, while S3 and S4 have 2 and 3, respectively. As observed in Nb nanowires, the OMR is generally clearer in samples with a smaller thickness and width. Both S3 and S4 have a wide range of magnetic fields for which the resistance is non-zero. The width of the transition to superconductivity

is small, and so few peaks are observed. The superconductivity can persist to higher applied magnetic fields due to the larger width and thickness of these samples.

The gradient of the OMR peaks versus peak order, n, gives an average measure of the periodicity. The values measured are similar to those observed in Nb nanowires. Figs. 4.9, 4.10, and 4.11 all showing an average periodicity of up to 0.7 T for Nb. In this case, the In-SnTe has a periodicity in the range 0.04 T to 0.2 T. In the Little-Parks and SQUID based OMR explanations, these periods equate to an area of $1-5 \times 10^{-14} m^2$, which is equivalent to a circle of radius $60-130 nm$. It is unreasonable to suggest that these samples are capable of supporting this size of normal core required for a SQUID or Little-Parks type effect. The random nature of the In-SnTe nanowire growths provided a range of thicknesses and widths to study. Fig. 5.17 shows the average period, $d\mu_0 H_{Peak}/dn$ may have some dependency on sample width. From the period vortex motion toy model the period was expected to decrease with width. Pinning should be lesser for the crystals and so if there was some dependency on the sample dimensions it should be clearest in single crystal samples. The discrepancy between the toy model and the observations could be from either the simplicity of the model or this data could be a fluke. Four samples is not enough to make a generalisation in this case. The thickness may also be important, however the range of thicknesses available is small and the exact values difficult to determine for samples that become damaged during measurements.

Following from the analysis presented in the study of Nb nanowires, the effect of temperature on the periodicity and resistivity of the OMR signal is shown in Fig. 5.18. For comparison, the Nb study is shown in Fig. 4.9. Panels (a) and (b) show the MR in the in plane, transverse and longitudinal configurations. The MR does not change significantly under rotation for this sample and so only the results from the OMR in the transverse configuration are presented. As for Nb nanowires, the centre peak field, $\mu_0 H_{Peak}$, appears approximately linear versus peak order. However, as discussed for the samples S1 and S2, the higher order peaks appear to deviate from this trend. Rather than shift the peaks to ensure a linear fit, the high order peaks are omitted from the linear fit to remove subjective bias. Fitting is shown in panel (c). The step size for the low order peaks appears unchanged with temperature, as seen in panel (d), although the high order step sizes appear to be anomalously large. Panel (e) shows the gradient of $\mu_0 H_{Peak}$ vs n, which is an average measure of the periodicity. While the variation of this measure is small, it does show a slight increase in period with temperature. A similar trend is observed in Nb nanowires, although the origin is not clear. In the SQUID and Little-Parks models, an increase in temperature could only increase the size of the normal core. An increase in SQUID loop area or Little-Parks cylinder circular area should decrease the period. This is not observed, and so these explanations are not appropriate. Panel (f) shows that the peak resistivity appears to vary randomly, however the total peak area integral, $\int \rho dH$, has a general decrease with temperature. This is not observed for Nb nanowires. An apparent reduction in OMR power loss at higher temperature could be caused by an increase in background resistance effects, which could reduce the observable OMR. Thermal energy could cause an increase in vortex motion, as the energy of the vortices increase a greater population will overcome the energy barriers. Although, if the vortices are not constrained at the lowest temperatures, and motion is already viable, then the addition of thermal energy will cause an increase in the monotonically increasing background resistance at the expense of the periodic OMR. It is possible that the increase in average periodicity is an artefact from the
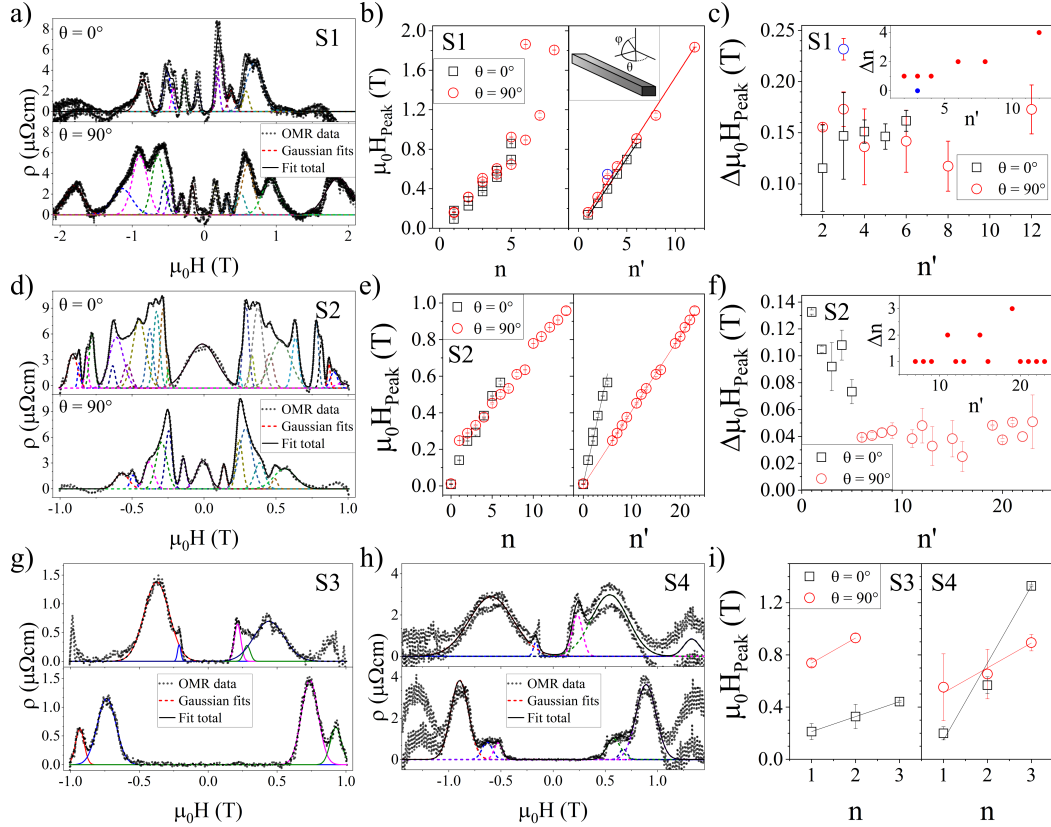
Figure 5.16: OMR peak field analysis for four In-SnTe samples, in the in plane, transverse, $\theta = 0°$ orientation and the in plane, longitudinal, $\theta = 90°$ orientation. a-c) S1, d-f) S2, g) and i) S3, h) and i) S4. Sample information in Fig. 5.14. a), d), g), and h) show the OMR data after subtraction of a smooth background with individual Gaussian fits and the total sum of the Gaussian fit. b), e), and i) show the peak centre magnetic field vs peak order, n, for the four samples. b) and e) also show an adjusted peak order n', which misses peaks in order to create a straight line. Linear fits are included to discuss the average period by using the gradient. c) and f) show the field step size between peaks vs the adjusted peak order. Insets in c) and f) show the peak order step size between peaks vs the adjusted peak order for S1 and S2. A single point in the inset of (c) is highlighted blue as it is an extra peak at $n' = 3$. Angle θ is defined in the inset of b), a replica of Fig. 3.11. During analysis the subtracted background resistance was taken as a smooth spline to points of minimum resistance.
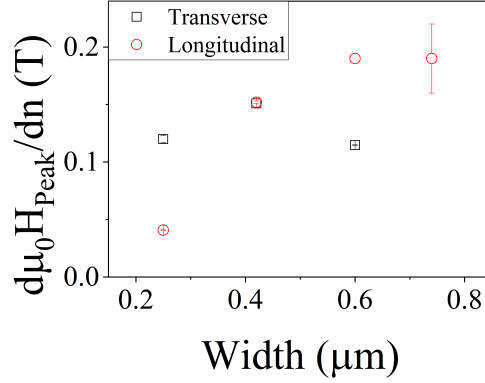
Figure 5.17: The gradient of the peak field vs n, for the four samples shown in Fig. 5.16, vs the sample width.

fitting procedure. The OMR effect studied here has many overlapping peaks and there could be missing peaks, that were dominated by neighbouring peaks in the fitting procedure.

Sample S1 does not have a strong angular dependence in the OMR effect, as shown in Fig. 5.14 (a-c). Sample S2, on the hand, has a different periodicity in the two orientations, as shown in Fig. 5.14 (d-f). Fig. 5.19 (a) and (b) show the MR for sample S2 in the in plane, transverse and longitudinal configuration, for a series of temperatures. The OMR in the two configurations is clearly different, with a lower onset magnetic field in the longitudinal configuration. Consequently, is pertinent to examine the temperature dependencies of the OMR effect in the two configurations. The extracted centre peak fields are shown in panel (c). As previously observed, the high order peaks deviate upwards from the otherwise approximate constant periodicity. These anomalously high peak fields are omitted from the linear fit used to define the average periodicity. The gradient of the peak field versus peak order are shown in panel (d). The difference between the two perpendicular orientations is apparent here. At the base temperature, the periodicity is the same. As the temperature is increased, the OMR in the transverse orientation has a smaller periodicity, and in the longitudinal orientation gains a larger periodicity. The average of the two orientations is also shown, and remains constant within the error. The reasons for this deviation are not clear. Again the deviation from a constant period with respect to temperature could be an artefact of the fitting. The high density of peaks in the OMR means that there could be peaks missing from the analysis. From panels (e) and (f) it is shown that the peak resistivity and total OMR integral support the temperature dependence observed in S1. As for S1, the individual peak resistances are scattered, but the total OMR integral has a reduction with increasing temperature.

In Nb nanowires, it was observed that the peak field decreases with an increasing applied AC amplitude. Fig. 5.20 shows a similar investigation with In-SnTe nanowires. The peak field is effectively unchanged over the range studied, until the background OMR dominates at 30 μA. The peak field was reduced in Nb, as the upper critical field was also reduced, pushing the thermodynamic mechanisms to lower magnetic fields. In the case of In-SnTe nanowires, the transition width is very broad. The upper critical field is not suppressed until the OMR effect is removed. This can be seen from the MR data at 20 μA and 30 μA, where the upper critical field suppression is accompanied by the disappearance of the OMR. This shows that while the
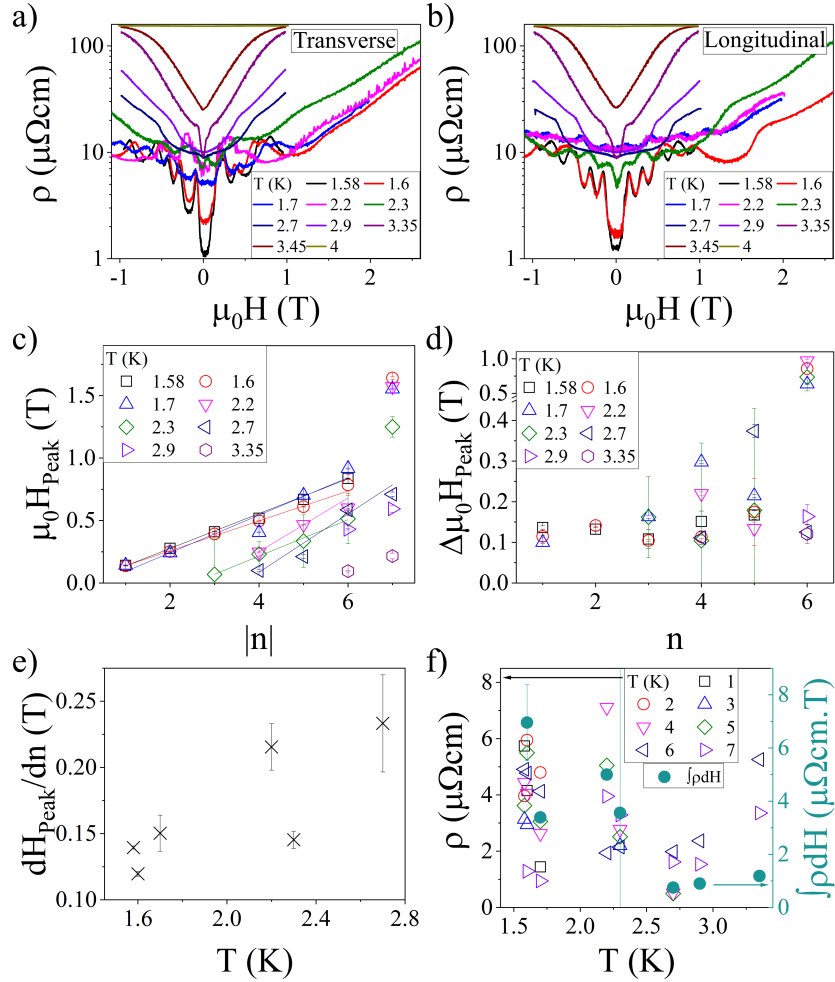
Figure 5.18: Temperature dependence of the MR and OMR fit parameters for sample S1. Thickness = 0.1 μm, width = 0.42 μm, length = 0.41 μm, T_c = (3.6±0.2) K. AC frequency = 773.7 Hz. AC amplitude = 1 μA. a) MR in the in plane, transverse configuration with temperatures of the range 1.58 K to 4 K. b) MR in the in plane, longitudinal orientation with temperatures of the range 1.58 K to 4 K. c) The extracted peak centres in the transverse orientation, (a), vs the peak order. Linear fits are included to discuss the average period by using the gradient. d) The step size between adjacent centre peak fields vs the peak order, in the transverse orientation. e) The gradient of the linear fits from (c) vs temperature. f) The maximum resistance (open symbols, left y-axis) in each Gaussian event vs temperature, right hand axis shows the total integrated OMR (solid circles). During analysis the subtracted background resistance was taken as a smooth spline to points of minimum resistance.
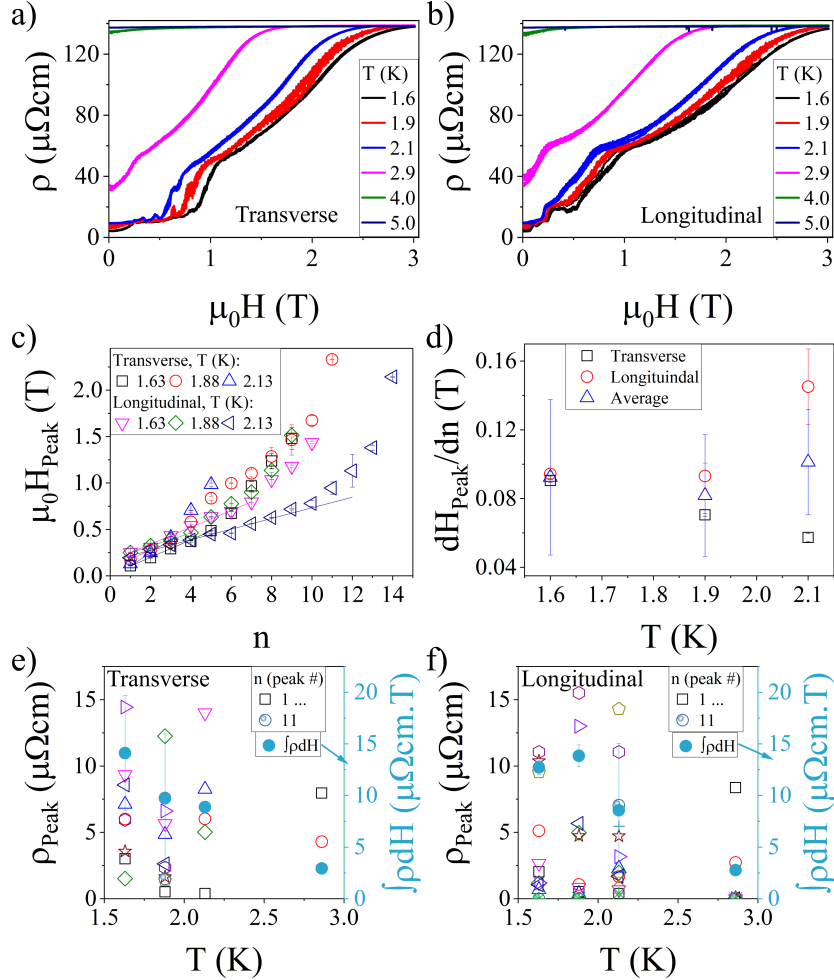
Figure 5.19: Temperature dependence of the MR and OMR fit parameters for sample S2. Thickness = 0.1 μm, width = 0.21 μm, length = 7.6 μm, T_c = (3.3 ± 0.5) K. AC frequency = 773.7 Hz. AC amplitude = 1 μA. a) MR in the in plane, transverse configuration with temperatures of the range 1.6 K to 5 K. b) MR in the in plane, longitudinal orientation with temperatures of the range 1.6 K to 5 K. c) The extracted peak centres in the transverse orientation, (a), and longitudinal orientation, (b) vs the peak order. Lines show the linear fits at low peak order. d) The gradient of the linear fits from (c) vs temperature. The average of the two orientations is also included. e) and f) The maximum resistance (open symbols, left y-axis) in each Gaussian event vs temperature, right hand axis shows the total integrated OMR (solid circles). e) In the transverse orientation and f) in the longitudinal orientation. During analysis the subtracted background resistance was taken as a smooth spline to points of minimum resistance.

applied current amplitude is a key parameter in the control of the OMR peak field values, it can have a greater influence over the general superconducting properties which dominate the MR signal. In the case of Nb, this influences the measured OMR peak fields through the general suppression of superconductivity, rather than directly through mechanisms such as the increase in Lorentz force or modulation of the vortex edge boundaries. Fig. 5.20 (c) and (d) show that the OMR magnitude follows a similar pattern in peak order for the measured range of currents that demonstrated an OMR effect. The general trend is that the OMR is reduced, this reduction is best described using the OMR peak integral. In Nb nanowires, the peak resistivity and total OMR integral are observed to increase with applied current. However, a cross comparison is not so straightforward. In the analysis of the Nb OMR, the subtracted background was taken as the MR for the lowest current. This provided successful fitting and was justified as the OMR became negligible at the lowest current value. In the analysis of the In-SnTe current dependence, the OMR does not persist throughout the entire magnetic field induced transition, and so it cannot be assumed that all of the MR is due to the OMR effect. As can be seen in the MR data, panel (a), the resistivity of the peaks does increase with current, but the smooth background also clearly increases. Simulations must be performed to assist with the modelling of OMR to include a background resistance. Simulations such as these are beyond the scope of this thesis.

In Nb samples, the AC frequency dependence of the OMR characteristics was observed to have a cut off frequency where the OMR magnitude was diminished and the magnetic field required to cause an OMR event increased toward $\mu_0 H_{c2}$. The range of frequencies studied for In-SnTe is smaller, however there are some differences between the behaviour. Fig. 5.21 shows the MR data and frequency dependent analysis for two samples. From the MR data in panels (a) and (d), as the frequency increases the background resistance increases. In sample S3, this has the effect of reducing the field at which the OMR event occurs, as shown in the extracted value $\mu_0 H_{Peak}$ in panel (b). Interestingly, the extracted peak area appears to remain roughly constant in the range of frequencies. In sample S2, the OMR appears to change in both peak field and peak area. These changes are not explained by the periodic vortex motion mechanism. In this system, the background resistance clearly changes considerably over the frequency range. It is likely that there is some other resistive factor that the OMR dominating the changes.

5.3.1.1 In Plane Magnetic Field Orientation

As for the Nb nanowires, an in plane rotation should be able to provide clear evidence that the OMR effect is not due to some SQUID or Little-Parks type effect. Fig. 5.22 shows the MR and analysis for two samples that have been measured at a series of in plane angles. S4, shown in panels (a-c), has a small oscillatory modulation in both the values of peak field and the peak area. For both the SQUID and Little-Parks effects, the flux through any loops, that would contribute to an OMR, should tend to zero when the magnetic field is applied longitudinally, $\theta = 90°$. While the magnetic field required to cause an OMR event is larger, approximately 1.5 times, in the longitudinal configuration, this small change does not agree with these quantum interference models. For S1, the in plane angular dependence is less clear, with some resemblance to the oscillatory modulation of S4, but with a greater scatter of values occurring in both the peak field, panel (e), and the peak area, panel (f). The complex
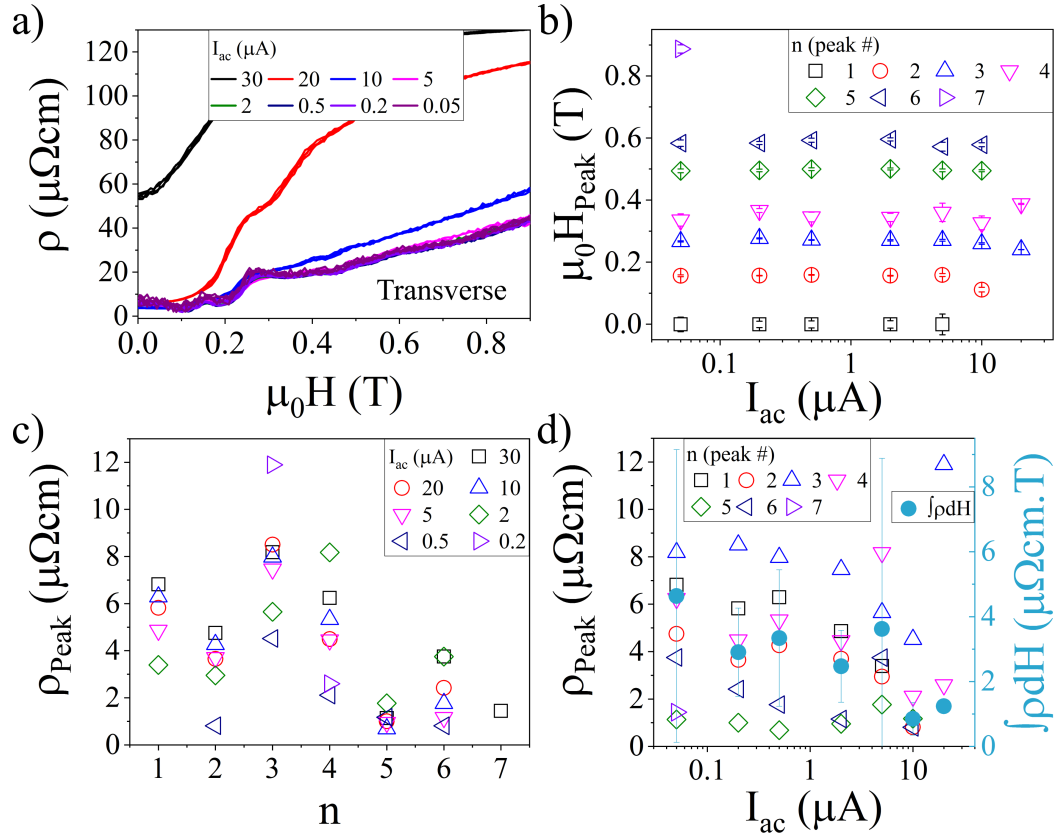
Figure 5.20: Applied current amplitude dependence of the MR and OMR fit parameters for sample S2. Thickness = 0.1 μm, width = 0.21 μm, length = 7.6 μm, T_c = (3.3 ± 0.5) K. Temperature = 1.6 K. AC frequency = 773.7 Hz. a) MR in the in plane, transverse configuration with currents of the range 0.05 μA to 30 μA. This equates to current densities of the range 2.4 MAm^{-2} to 1.4 GAm^{-2}. b) The extracted peak centres in the transverse orientation vs the applied current amplitude. c) The peak resistivity vs peak order. d) The peak resistivity and total OMR integral vs applied current amplitude). During analysis the subtracted background resistance was taken as a smooth spline to points of minimum resistance.
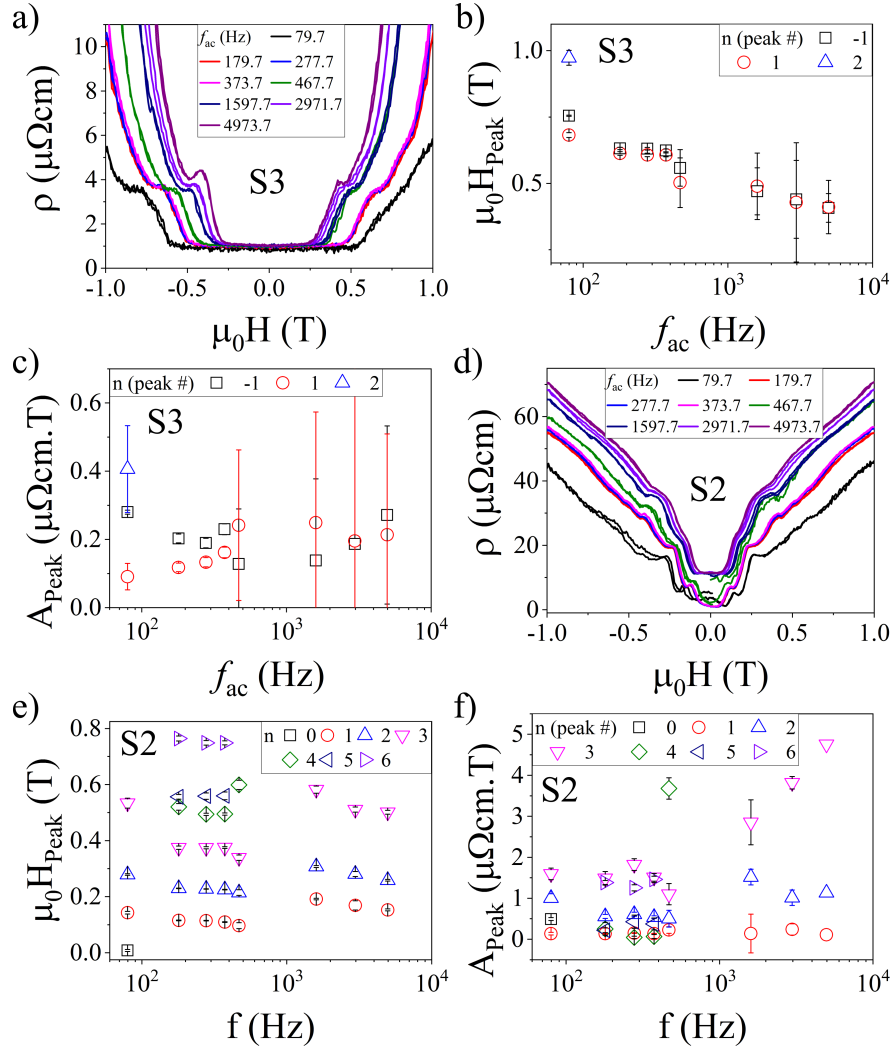
Figure 5.21: Applied alternating current frequency dependence of the MR and OMR fit parameters for S3 and S2. a-c) S3, thickness = 0.1 μm, width = 0.6 μm, length = 4.1 μm, T_c = (3.1 $\pm$ 0.1) K. d-f) S2, thickness = 0.1 μm, width = 0.21 μm, length = 7.6 μm, T_c = (3.3 $\pm$ 0.5) K. Temperature = 1.6 K. AC amplitude = 1 μA. a) MR for S3 in the transverse configuration for a range of 80 Hz to 5000 Hz. b) The extracted peak centres in the transverse orientation vs AC frequency, extracted from (a). c) The peak area vs AC frequency, extracted from (a). d) MR for S2 in the transverse configuration for a range of 80 Hz to 5000 Hz. e) The extracted peak centres in the transverse orientation vs AC frequency, extracted from (d). f) The peak area vs AC frequency, extracted from (d). During analysis the subtracted background resistance was taken as a smooth spline to points of minimum resistance.
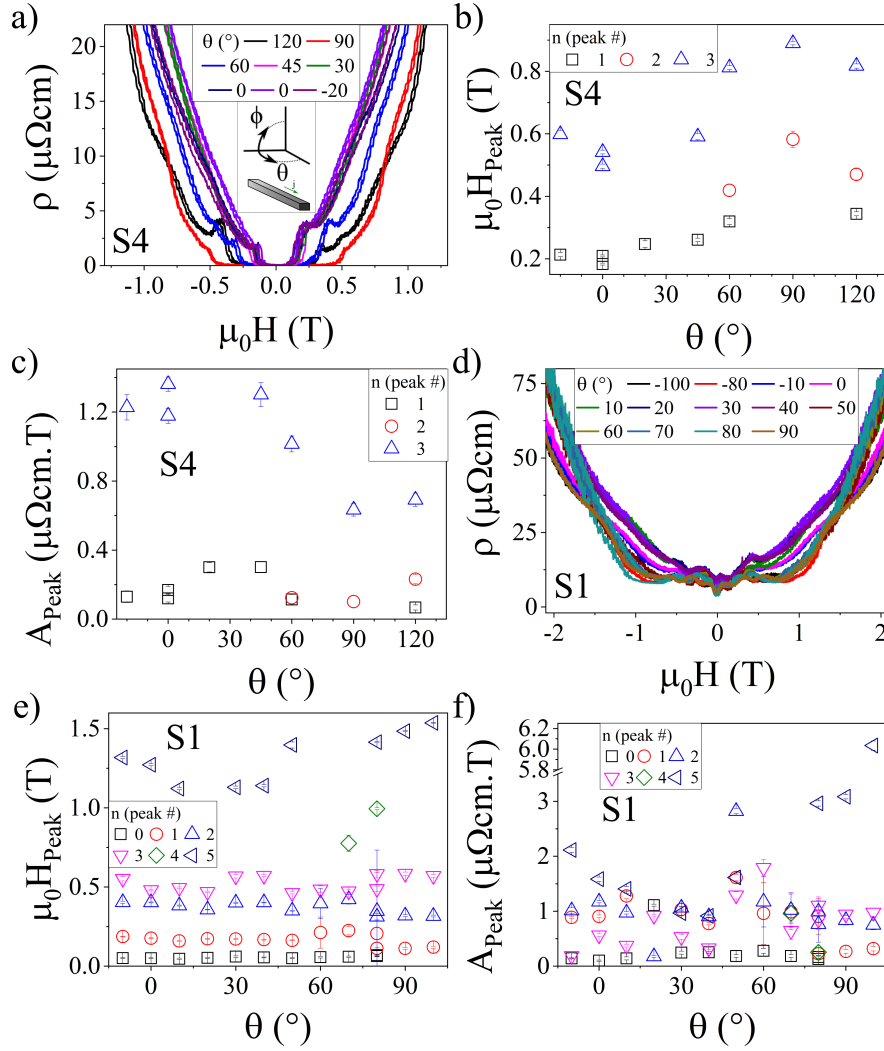
Figure 5.22: In plane magnetic field orientation dependence of the MR and OMR fit parameters for S4 and S1. a-c) S4, thickness = 0.3 μm, width = 0.74 μm, length = 8 μm, $T_c = (3.0 \pm 0.2)$ K. Temperature = 1.6 K. AC amplitude = 1 μA, AC frequency = 773.7 Hz. a) MR for S4 in an in plane configuration, rotated through θ. b) The centre peak fields vs θ, extracted from (a). c) The peak area vs θ, extracted from (a). d-f) S1, thickness = 0.1 μm, width = 0.42 μm, length = 0.41 μm, $T_c = (3.6 \pm 0.2)$ K. Temperature = 2.3 K, I_{ac} = 1 μA, f_{ac} = 773.7 Hz. d) MR for S1 in an in plane configuration, rotated through θ. e) The centre peak fields vs θ, extracted from (d). f) The peak area vs θ, extracted from (d). Angle θ is defined in the inset of b), a replica of Fig. 3.11. During analysis the subtracted background resistance was taken as a smooth spline to points of minimum resistance.

behaviour may simply appear due to the fact that there is a higher density of OMR peaks, overlap in which can cause additional errors to the Gaussian fitting. This is another example of the problems encountered when analysing OMR data and could be one of the reasons why discussions in literature are so varied.

The angular dependence for sample S4, taken to be representative due the simplicity of fitting, is the opposite to the trend shown in Nb nanowires, which have a maximum in the transverse orientation, and a minimum in the longitudinal orientation. As discussed, in that scenario the most likely cause of modulation is through a varying out of plane magnetic field component, which is largest for these samples near to the longitudinal configuration.

5.3.2 Pulsed IVs

No investigation of a superconducting material would be complete without measurements of the critical current density. In Nb nanowires, pulsed IVs in the in plane transverse configuration showed a stepping and jumping between voltages. This is interpreted as instabilities on the time-scale of the pulse probe. Pulsed IVs of In-SnTe nanowires do not show the same effect, as shown in Fig. 5.23. In the longitudinal configuration there are one or two jumps, but as they do not align with the magnetic fields at which OMR is observed, they are unlikely to be an associated feature. There is thus only one critical current, which monotonically decreases with applied magnetic field. The reason why the jumps were observed in only Nb, and not In-SnTe could be due to the fact that the Nb measured was much thinner, and so vortex motion has a stronger impact on the pulsed IV characteristics.

5.3.3 Oscillatory Magnetoresistance Summary

The OMR observed in In-SnTe grown by VTG has many characteristics that agree with the periodic vortex motion model, as simulated by Berdiyorov *et al*. [19]. Some of the characteristics agree with the observations from Nb nanowires, as covered in Chapter 4. The OMR effect is best described by a series of Gaussian fits to the signal, after the subtraction of a smooth monotonic background resistance. Interestingly, some of the characteristics are different to those observed in Nb nanowires. The periodicity of the OMR effect is observed to be non-linear at high fields, with a potential explanation from a particularly stable arrangement of vortices. The low magnetic field periodicity does not deviate greatly as the temperature or AC amplitude are varied. The magnitude of the OMR decreases with temperature and AC amplitude over the ranges probed. This fits into the periodic vortex motion model. At the lower AC amplitude and temperature range, the vortices can be liberated and forced into motion with the application of a small magnetic field. As the temperature and current amplitude are increased, the vortex motion increases and has fewer periods of reduced motion. This develops into a monotonic resistance. The result is a reduction in the OMR that can be isolated from a background resistance. As $I \sim I_{crit}$ and $T \sim T_c$, the OMR becomes dominated by the monotonic background resistance, which becomes the normal state resistance. The AC frequency dependence varies between the two samples studied, with the background resistance dominating any changes observed. Quantum interference OMR mechanisms are disproved by the weak dependency of the OMR effect on the orientation of the magnetic field applied. The pulsed IV measurements show that the
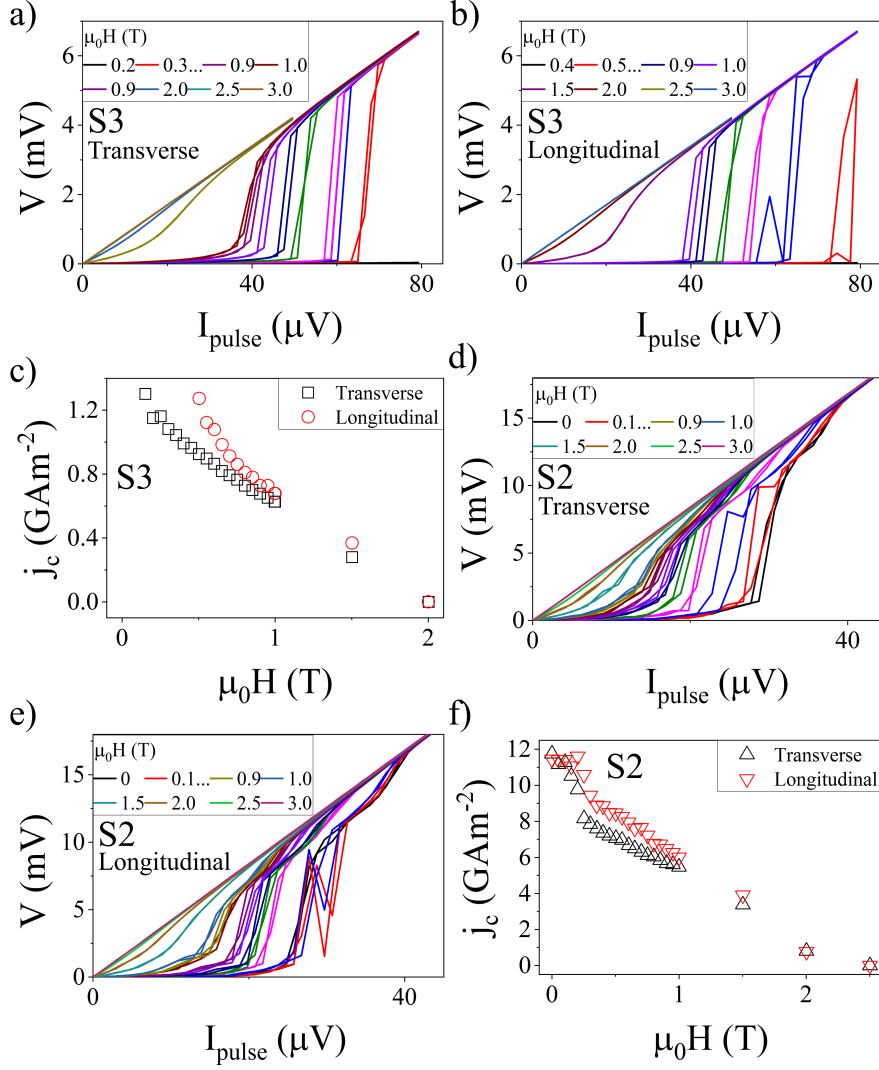
Figure 5.23: Pulsed IVs with varied magnetic field for samples S3 and S2. Sample information given in Fig 5.21. Temperature = 1.6 K. a-c) S3, thickness = 0.1 μm, width = 0.6 μm, length = 4.1 μm, T_c = (3.1 ± 0.1) K. a) Pulsed IV data in the in plane, transverse configuration. b) Pulsed IV data in the in plane longitudinal configuration. c) Critical current densities extracted from (a) and (b). d-f) S2, thickness = 0.1 μm, width = 0.21 μm, length = 7.6 μm, T_c = (3.3 ± 0.5) K. d) Pulsed IV data in the in plane, transverse configuration. e) Pulsed IV data in the in plane longitudinal configuration. f) Critical current densities extracted from (d) and (e). IV measurements involved a positive and negative amplitude ramp rate, both directions are plotted to show the small hysteresis in most cases. Critical current values are taken as the point at which V/I_{pulse} is equal to half the normal state resistance.
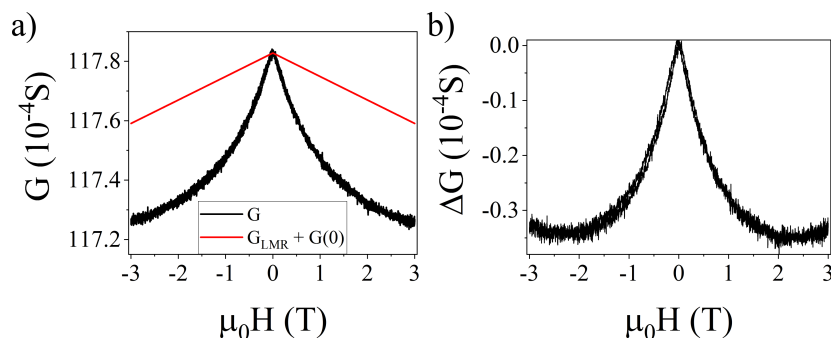
Figure 5.24: Isolation of the WAL component of the magnetoconductance. a) The measured magnetoconductance, G and the background subtracted, the summation of a resistance offset, $G(0)$, and the linear MR, G_{LMR}. b) The WAL conductance, resulting from the difference between the data and background.

OMR effect in these samples is not associated with a Weber blockade. The IVs show a sharp transition between the superconducting state and an Ohmic state.

The OMR observed in In-SnTe shows that the study of OMR is not always as it appears in Chapter 4. In the study of the In-SnTe, small differences in the sample properties give differences in the extracted OMR characteristics. This study is a prime example of the general issues facing the study of this effect. No two samples are the same and clearly the choice of material or growth method determines how the OMR will behave. As outlined by Berdiyorov *et al.* [19], pinning plays a large role in the exact periodicity and form of the OMR signal. The result of this is that the OMR can probe the pinning landscape, but as of yet the output information only provides puzzle pieces to the underlying mechanisms.

5.4 Weak Anti-localisation

Above T_c, and below 15 K, there is a distinct feature in the MR. A $\leq 1\%\rho_N$ dip in resistivity is observed with magnetic field up to $1 \sim 2T$. This resistivity suppression cannot be attributed to superconductivity, as it appears at temperatures of up to $5{\times}T_c$. The model by Hikami, Larkin, and Nagaoka (HLN) describes WL and WAL in 2D systems [57]. This model is also used in 3D TIs as it should be able to describe the WAL effect from the surface states. Due to the large bulk conductivity of the highly doped material, the WAL effect is small relative to the background conductivity. It is also superimposed onto other magnetoresistance effects. As shown in Fig. 5.13, the only other MR observed is a small, linear magnetoresistance. Although small in this case, any background MR effects could distort the values of α extracted from a HLN fit. In order to remove the linear MR, a linear fit above the WAL regime is subtracted from the measured resistance.

The Hall conductance, G_{xy}, should be included in the calculation of the linear conductance, G_{xx}. Due to the fact that the samples are nanowires, the Hall resistance is impossible to measure. Contacts cannot be fabricated that are capable of measuring a transverse voltage, due to the resolution of the lithography. Using a nanoplate, a measurement

was made possible and shows that the carrier density is $\sim -(11 \pm 6) \times 10^{22} cm^{-3}$. Assuming that the nanowires in this study will a similar carrier density, the Hall resistance of these samples will be an order of magnitude smaller than the linear resistance. This means that the conductance can be approximated to $\approx G = \frac{1}{R}$, and we can define the WAL conductance $\Delta G = G(\mu_0 H) - G(0) - G_{LMR}$. Where G_{LMR} is the conductance associated with the linear MR. G_{LMR} is taken to be the same for the range of temperatures measured, and $G(0)$ is the zero field conductance. The isolation of the low magnetic field WAL signal is shown for example data in Fig. 5.24. The WAL conductance, ΔG, is then fitted to the HLN formula:

$$\Delta G = \alpha c_1 \left[\psi \left(\frac{1}{2} + \frac{c_2}{\mu_0 H l_\phi^2} \right) - \ln \left(\frac{c_2}{\mu_0 H l_\phi^2} \right) \right], \tag{5.1}$$

where the constants are defined, $c_1 = \frac{e^2}{2\pi^2 \hbar}$ and $c_2 = \frac{\hbar}{4e}$. l_ϕ is the phase coherence length. This characteristic length scale is the typical length scale travelled by carriers before they lose coherence. A larger phase coherence length typically requires a larger external magnetic field to remove the WAL effect.

All other MR effects cannot be encompassed in the linear subtraction. In addition the MR may be temperature dependent or have some non-trivial low-field dependence. Such effects would not be discernible as they cannot be isolated from the WAL. In our case we must also be particularly cautious due to the superconductivity. One possible route to testing the validity of the fit is to change the range over which the data is tested. For a fit including data beyond the WAL effect, a systematic error in parameters will be introduced and the fitting poor. When the range chosen is smaller than the full range where WAL dominates the error in parameters will be unnecessarily large. A demonstration of this is given in Fig. 5.25. The critical temperature of the nanowire is (3.6 ± 0.1) K. If the measurement temperature is too close to T_c, then the fitted values of l_ϕ and α will be inflated or spurious, and the data will not fit well to the HLN model. This is shown in both figures in panels (a-c). At 4 K the model does not describe the data well and the parameters l_ϕ and α depend heavily on the range chosen, see panel (h). This indicates that the samples are partially superconducting at low field giving an additional increase in conductivity. At 5 K, the model describes the data very well for both samples as shown in panels (d-f). Fig. 5.26 shows the fitting for different field fit upper limits. The smaller range of alpha at 5 K shows that the fitting does not depend strongly on the fitting range, indicating that there are no other MR contributions. The optimum fitting field range is 1 T. Below this fitting range the error is large, and as the fitting range is increased the value deviates due to the influence of the background MR. A field fitting range of 1 T was chosen for the following HLN fits.

Fig. 5.27 (a) and (b) demonstrate that the WAL is not dependent upon the orientation of the magnetic field. Panel (a) shows the temperature dependence of the WAL fitting parameters for measurements at three angles from in plane, transverse to out of plane, transverse. The values for the three angles match well. Panel (b) show the angular dependence of the WAL fitting parameters for two samples. In panel (b) the parameters are normalised to demonstrate that the deviation from the normalisation value is $\leq 4\%$. The WAL in 3D topological insulators is expected to be independent of the magnetic field orientation, as the surfaces can contribute to the WAL effect regardless of magnetic field orientation. WAL has also been observed to have no angular dependence in SnTe nanoplates [77].
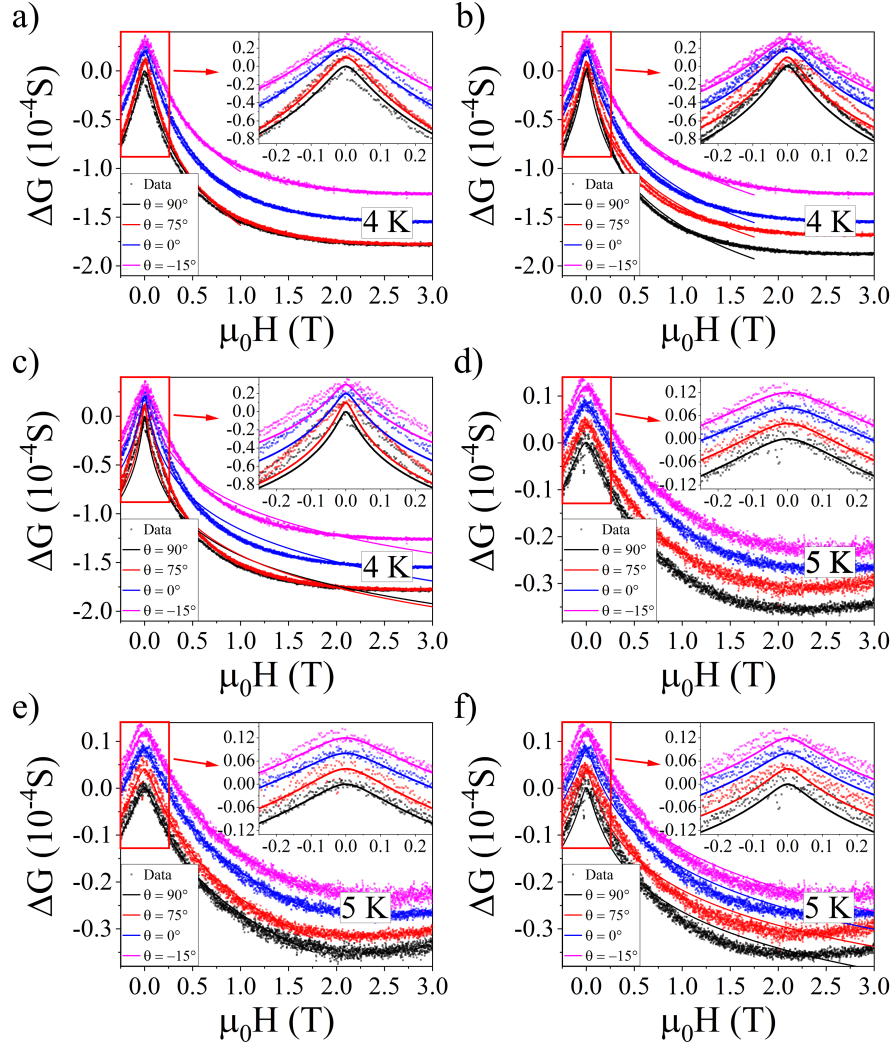
Figure 5.25: Demonstration and justification for the choice of fitting field range for the HLN fit. The sample is an In-SnTe nanowire with $T_c = (3.6 \pm 0.1)$ K, thickness = 0.1 μm, width = 0.6 μm, length = 4.1 μm, and x_{source} = 20 %. It is important to note the different scales used for the two different temperatures. Conductivity enhancement is a factor of ~ 6 larger for the 4 K data than the 5 K. a)-f) Measurements are shown at two temperatures, for four in plane angles, θ, which is defined in Fig. 3.11. The insets show the low field fit, a magnification of the red boxes. a)-c) Three ranges of fitting to MR data taken at 4 K, ΔG is offset by 0.1 10^{-4} S for the four angles. Ranges a) 1 T, b) 1.75 T, and c) 3 T. d)-f) Three ranges of fitting to MR data taken at 5 K, ΔG is offset by 0.04 10^{-4} S for the four angles. The insets show the low field fit, a magnification of the red boxes.
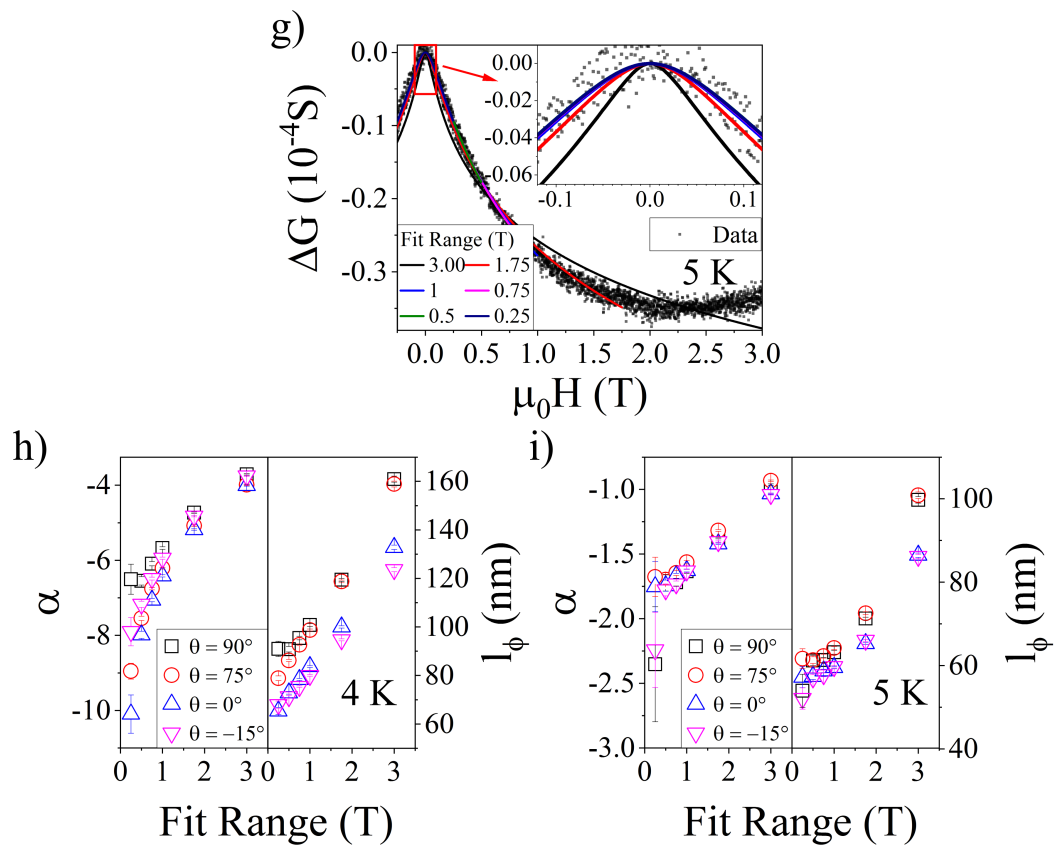
Figure 5.26: Demonstration and justification for the choice of fitting field range for the HLN fit and the risk of false readings near to the superconducting critical temperature. a) Fitting a data set with different fitting ranges from 0.25 to 3 T, the inset is a magnified view of the low field data. b) and c) Fit results α and l_ϕ vs the fitting range, for b) 4 K and c) 5 K.
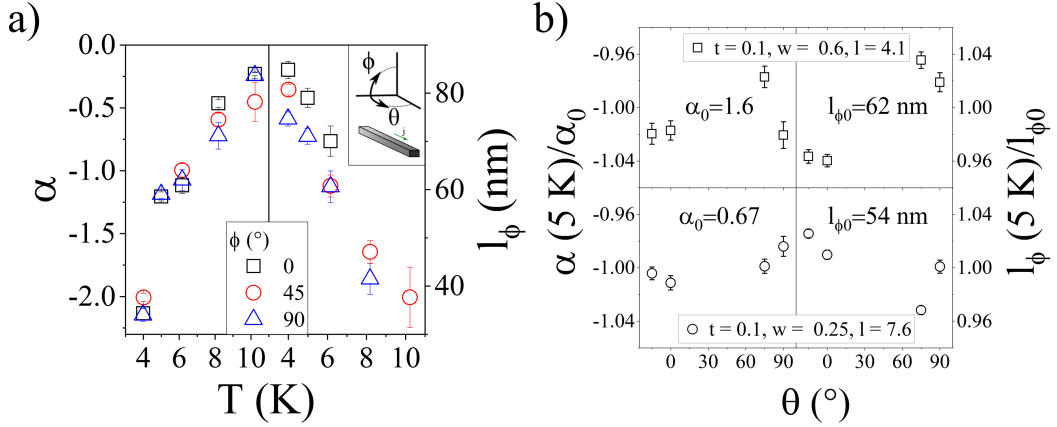
Figure 5.27: Testing the angular dependency of the HLN fitting parameters α and l_ϕ in In-SnTe nanowires. HLN fitting range of 1 T. a) A transverse, in plane to out of plane rotation, defined by angle ϕ. b) An in plane, transverse to longitudinal rotation in θ, for two samples at 5 K. α and l_ϕ are normalised to α_0 and $l_{\phi 0}$ respectively to show the small deviation under in plane rotation. Both angles ϕ and θ are defined in the inset of (a), a replica of Fig. 3.11.

The results of many In-SnTe nanowires are summarised in Fig. 5.28. The inset shows the thickness, width and length of the samples studied. The temperature dependence of the values of α is expected for WAL. The temperature disrupts the anti-localised surface channels, causing a reduction in the contribution to conductivity. Care is taken at this point to note that this material is superconducting, and many of the critical temperatures are around 3 K. There is potential, as shown in Fig. 5.25, that superconductivity could be present at 4 K. This temperature range is highlighted using a blue shaded area. In this area the presence of superconductivity results in non-physical values of α. For SnTe based topological crystalline insulators $-2 < \alpha < 0$, this limit is due to the maximum of 4 surface channels. Discounting the shaded region, the values of alpha are all physically reasonable. However, there is clearly a large range of values in that acceptable range. To further examine this, panel (b) shows the values of α at 5 K versus the normal state resistance, R. Interestingly the normal state resistance appears to be correlated with the extracted value of α. On the other hand, the sample resistivity has no such relation with α. Error bars are large on the sample resistivity due to the large error in determining the exact sample thickness. As the zero field conductance is subtracted from the measured conductance, the magnitude of the WAL conductance should not be reduced by this analysis to create an artificial correlation. It is expected that α should indicate the number of quantised channels available to give the WAL conductance. This number of surface channels can be limited by the sample dimensions, if the space is limited then the channels interact strongly and scattering increases, destroying the phase coherence. The normal state resistance is a good parameter to compare with α as it is also strongly affected by the dimensions. The normal scattering mean free path decrease as the increased proximity to surfaces increases the scattering processes. To gain further insight into the mechanism that suppresses the WAL contribution to conductance, information on the carrier density and mobility is required. Hall
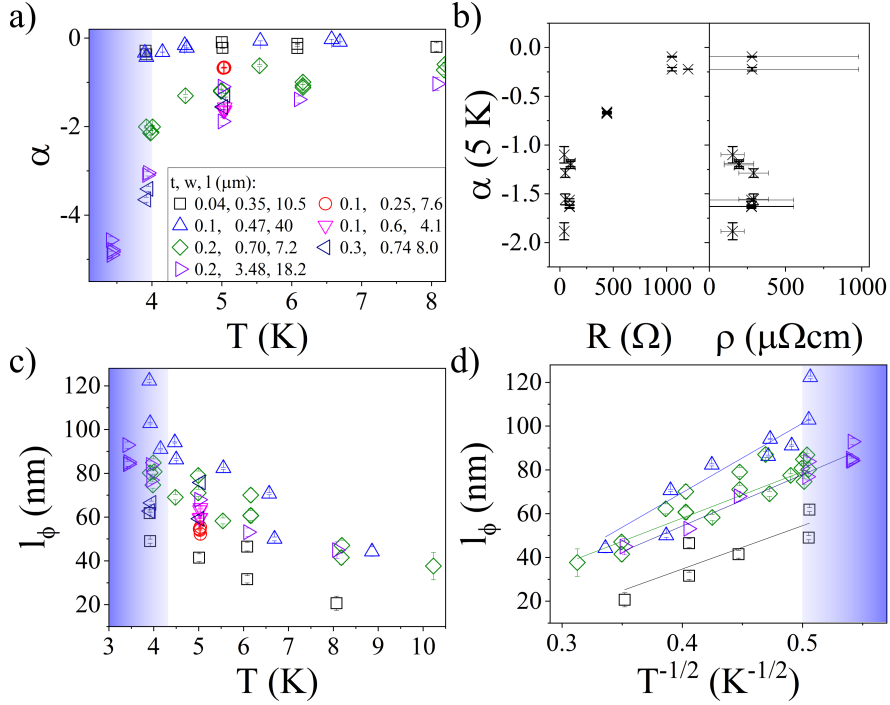
Figure 5.28: Fitting paramters obtained by fitting the WAL data with the HLN model. a) α vs temperature for seven samples, with the thickness, t, width, w, and length, l, listed in the legend. b) α at 5 K for the range of sample studied vs the normal state resistance and resistivity. c) l_ϕ vs temperature. d) l_ϕ vs temperature$^{-0.5}$ including linear fits. The legend of (a) applies to (c) and (d). Blue shading represents the area where superconductivity may distort the WAL effect, exaggerating the values of α. The HLN fitting range is 1 T.

measurements of these nanowires is currently not viable and so these parameters cannot be measured.

The values of l_{phi} measured match those expected from theories and previous experiments and reduces with increasing temperature, shown in Fig. 5.28 (c). The temperature dependence should follow $l_{phi} \propto T^{-0.5}$ if the dephasing mechanism is through 2-dimensional Nyquist electron-electron scattering processes [151–154]. Fig. 5.28 (d) shows the fitting of l_ϕ versus $T^{-0.5}$. This fits remarkably well, signifying that the WAL follows this standard mechanism.

5.4.1 Weak Anti-Localisation Summary

Weak anti-localisation has been observed in In-SnTe nanowires. The samples are superconducting, and so care has been taken to ensure superconductivity has not interfered with the WAL. Superconductivity can distort the WAL, making the fitted values appear to be physically impossible. The WAL observed fits well to the model for a 2D WAL effect by Hikami, Larkin, and Nagaoka. The values of α extracted from fitting the WAL indicated that

the samples have a maximum of four surface conductance channels contributing to the WAL. The values of l_ϕ are typical for a topological insulator, and the temperature dependence follows that expected for a 2-dimensional Nyquist electron-electron scattering process. There is a negligible angular dependence to the WAL, which appears to signify that the surface states contribute to the WAL equally regardless of the magnetic field orientation. A relationship between the normal state resistance of the samples and the WAL fitting parameter α appears to be connected by the reduced dimensions of the samples. The nanowires with the largest thicknesses and widths have a low resistance and α values between -1 and -2. At the opposite end of the scale, the samples with the smallest thicknesses and widths have α values an order of magnitude smaller. Reduced α values indicates that the surface channels are in too close proximity to have the full $\alpha = -0.5$ conductance. This is due to the increased scattering between channels confined by the spatial dimensions.

CHAPTER 6

Conclusions and Outlook

6.1 Conclusions

The main aim of this thesis was to investigate the characteristics of oscillatory magnetoresistance in superconducting nanowires, to explore the origin of the poorly understood phenomenon. To meet this aim, lithographically defined Nb nanowires were grown by DC sputter deposition, and characterised using magnetotransport techniques. Experimental and environmental parameters were systematically varied to explore the physical limits of the OMR mechanism.

The secondary aim of this thesis was to develop a clean method to grow In-SnTe superconducting nanowires, with the aim to investigate the transport properties of this candidate topological superconductor. To meet this aim, a systematic development of a vapour transport growth procedure was performed. During this process development, Au nanoparticles were used to enhance nanowire growth. Unexpectedly, the Au did not act as a catalyst and instead contaminated the Au, as published in Ref. [3]. This observation raises questions as to how appropriate the Au catalysts are, and future studies should take care to avoid contamination. Using statistical process development, a clean growth process was found. This resulted in In-SnTe nanowires with a radius comparable to the Bohr radius for SnTe. Electrical contacts were fabricated using an angled thermal evaporation. The superconducting properties were investigated and, for the first time, oscillatory magnetoresistance was observed in this material. In addition to this investigation, a weak anti-localisation effect was observed in the normal state magnetotransport.

Magnetoresistance of the Nb nanowires was measured over the available experimental range of AC amplitude and AC frequency. The first profound observation being that the observed OMR is poorly described by oscillatory functions, after which it is named. It is better represented by a series of normal distribution functions centred on semi-periodic magnetic fields. A novel approach to analyse the OMR signal has been presented in this thesis. Increasing the sample temperature was found to thermally assist the OMR effect. Thermal energy enhances the resistive power of the effect, until the resistance becomes dominated by the normal state. The amplitude of the AC current also acts to enhance the OMR effect, with a higher resistance for a higher current. Both a higher thermal energy and a higher applied current density act to reduce the magnetic field required to cause the OMR events. This suggests that the events are probabilistic, and that increasing the current and temperature reduce the effective energy barrier to an event. The behaviour of the OMR effect with AC frequency was unexpected. A high frequency cut off was observed, where the OMR resistive power loss tends to zero in the MHz range. In all cases, the periodicity of the OMR effect is poorly defined, with a large variation in the magnetic field step size between adjacent events.

The observations from these standard AC transport probes suggests that the OMR effect is a result of the periodic motion of vortices. The arguments in this thesis are generally based around the model simulated by Berdiyorov *et al.* [19]. In this picture, the vortex motion is impeded by surface barriers, which are essentially caused by the increase in local current density required for a vortex to enter or exit the system. The periodic nature appears due to the periodic packing of vortices into rows, which become stressed, before rearranging to allow further vortex penetration. Vortices can gain energy from the temperature, through thermal energy, and transport current, through the Lorentz force. The energy gained assists the

vortices in overcoming barriers to vortex motion. The imperfect periodicity agrees with model by Berdiyorov *et al.* [19]. Pinning, which is expected to be high in polycrystalline Nb, alters the paths of the vortices, providing some trajectories for which vortex motion is more difficult and some for which vortices can travel more readily. This results in a disruption to the perfect periodicity expected in an ideal sample. The frequency dependence of the OMR effect has not been explored in literature. When a simple harmonic oscillator is driven at a frequency much higher than the fundamental frequency, the system is not displaced far from equilibrium. This study, and others [137, 139] have found that there appears to be a collective vortex lattice relaxation time-scale of ~1 s. Following from this, it is reasonable to assume that the reduction in OMR at high AC frequencies is result of the large difference between the driving frequency and the fundamental frequency of the system. The Lorentz force oscillates too rapidly to displace the vortices from the stable lattice sites. The presence of pinning would enhance this effect. Pinning sites act as potential wells for vortices, in which they can be trapped.

The knowledge that the OMR effect can be reduced using high frequencies and low applied currents could be useful in the design of technologies that plan to use superconducting nanowires for lossless information or energy transfer. In technologies that plan to use vortex motion to manipulate encoded information, these limits could be used to turn vortex motion on and off.

The angular dependence of the OMR effect dismisses other known candidates for the underlying mechanism, such as a SQUID or Little-Parks effect. Otherwise, the dependency of the OMR characteristics on the angles in both in plane and out of plane orientations is not significant. The changes that do occur require further investigation. Tentative investigations into the sample size dependence do not show any definitive limit to the size required to observe OMR. As a rough guide, this study finds that the smallest dimension should be on the order of the superconducting coherence length or the penetration depth. This could be expected as this is the maximum effective size of a vortex.

Both DC and phase resolved AC magnetoresistance measurements provide evidence that the OMR effect does not only occur in parallel with the transport current flow, but can have some voltage component transverse and antiparallel to the transport current direction. For most resistive mechanisms this is impossible. In the case of periodic vortex motion, the vortices follow random paths across the superconductor. It is possible that the rearrangement of the vortex lattice can cause motion that is not aligned with the current, and so voltages that are not parallel to the current can be generated. An out of phase AC component can be observed if the driving frequency of the system is much faster than the relaxation frequency. This is supported by phase sensitive, frequency dependent measurements.

Pulsed IV measurements show the OMR in these Nb nanowires relates to voltage instabilities in the voltage-current relationship. Steps and jumps in the IV curves show that the resistance is unstable. This instability matches with the vortex motion description, as the events should be probabilistic. In AC measurements, these probabilistic events are averaged to a fixed value. The time scale of the pulsed IV measurements matches with the time scale expected for vortex lattice relation, from the AC frequency dependent measurements.

While some parallels can be drawn between the OMR observed in Nb and that observed in In-SnTe, there are a few fundamental differences. These differences are most likely to be due to the differences in material properties and sample deposition techniques. In-SnTe and Nb

have similar superconducting coherence lengths. However, the penetration depth of In-SnTe is expected to be ~ 5 times larger. This has consequences for the vortex lattice interactions with the pinning landscape and the edge boundaries. The pinning density is also expected to be different for the two sample sets, this is expected to greatly influence the collective motion of the vortex lattice. Samples grown by DC sputter deposition are polycrystalline, while those grown by vapour transport should be single crystals, or at least highly crystalline. The use of doping in In-SnTe causes a degree of disorder, shown in the reduction of the RRR parameter with high doping. This study is great example of why observations of OMR in previous works struggle to understand the underlying mechanism. The mechanism can be dominated by something as arbitrary as the pinning landscape.

The observation of weak anti-localisation in In-SnTe nanowires provides a piece of evidence that the topological crystalline surface states may be robust against high dopant levels. The weak anti-localisation fits well to the 2D WAL effect described by Hikami, Larkin, and Nagaoka [57]. The number of surface conduction channels was found to be a maximum of four, which agrees with the accepted maximum for SnTe. An unusual correspondence was observed between the nanowire resistance and α. α equal to half the number of independent surface conductance channels. The suggestion here is that a reduction in the thickness or width of a nanowire results in a high resistance, and also results in an increased scattering rate for the surface channels. This gives a reduced value of α for samples with a high resistance.

In summary, the investigation using Nb nanowires grown by DC sputter deposition points to periodic vortex motion as the most likely candidate to explain OMR. Both OMR and WAL have been observed in In-SnTe nanowires, grown without the use of Au nanoparticles. This study has shown that, while the control of vortices is far from possible, there is scope to use the OMR effect as a probe of vortex motion.

6.2   Outlook

New information has been uncovered into the mechanism that underlies the OMR effect. However, care should be taken in generalising the observations to all superconducting systems. The study of In-SnTe has shown that both the material properties and growth method can change the OMR properties. An investigation into a variety of materials, studied under the same conditions, is required to understand which factors are most important for controlling the OMR effect. Other type II, elemental superconductors, such as vanadium, could be directly compared with this study of niobium. To introduce disorder, alloys of Nb, such as NbTi, NbN and NbTiN could be used to test the validity of the conclusions found in this thesis. Future work should take great care to test the experimental parameters because, as we have shown, the choice of measurement is not arbitrary and can change the OMR effect completely.

Higher frequency studies could push the dependence observed in this thesis beyond the limit of the lock-in amplifiers used, to test if the OMR effect is removed at high frequency. A comprehensive systemic study of sample thickness, width and length is required to determine the limits of the OMR effect. This will assist in the study of the effect and provide dimensional limits for the size of superconducting nanowires used in technologies.

Further simulations of vortex motion are required to formulate a background resistance. If this becomes possible, the OMR effect could be effectively isolated from other resistive processes. Simulations and experiments must be paired well if the OMR effect is to prove useful. As there is a large variation in OMR between nominally similar samples, this adds complications to these simulations.

A useful experiment would be to image the vortices during transport measurements, using a scanning Hall probe to measure the stray magnetic field. If vortex behaviour could be matched with transport measurements, then this would provide clear proof that the origin of the OMR is periodic vortex motion.

Nanowires of In-SnTe have scope to be used in topological superconductor devices. Through etching, it is hoped that the vapour transport grown nanowires presented in this thesis could be transformed into Josephson junctions or SQUIDs. If topological superconductivity can be confirmed, then topological quantum computing devices that make use of the Majorana fermion braiding properties could be made using this material.

Further work is required to understand the weak anti-localisation that is observed in three-dimensional topological insulators and topological crystalline insulators. The study here is limited by the lack of information about the carrier density and mobility. Studies must be performed using nanoplates or lithographically defined Hall bars grown by molecular beam epitaxy, where the carrier density of the material can be determined.

6. CONCLUSIONS AND OUTLOOK

REFERENCES

[1] H. Kamerlingh-Onnes, Further Experiments With Liquid Helium, *Leiden Comm.* **120b, 122b, 124c** (1911) 2

[2] W. Meissner and R. Ochsenfeld, Kurze Originalmitteilungen, *Naturwissenschaften* **21**, 787 (1933) 2

[3] S. Atherton, B. Steele and S. Sasaki, Unexpected Au Alloying in Tailoring In-Doped SnTe Nanostructures with Gold Nanoparticles, *Crystals* **7**, 78 (2017) 3, 32, 93, 128

[4] J. F. Annett, *Superconductivity, Superfluids and Condensates*, Oxford Universty Press, Oxford (2004) 6

[5] M. Tinkham, *Introduction to Superconductivity (2nd Edition)*, T. Dover Publications (1996) 6, 13

[6] A. B. Pippard, An experimental and theoretical study of the relation between magnetic field and current in a superconductor, *Proc. Roy. Soc. (London)* **A216**, 547 (1953) 7

[7] V. L. Ginzburg and L. D. Landau, On the Theory of superconductivity, *Zh. Eksp. Teor. Fiz.* **20**, 1064 (1950) 7

[8] L. Gor'kov, Microscopic Derivation of the Ginzburg-Landau Equations in the Theory of Superconductivity, *Sov. Phys. JETP* **10**, 998 (1960) 7

[9] J. Bardeen, L. N. Cooper and J. R. Schrieffer, Microscopic Theory of Superconductivity, *Phys. Rev.* **106**, 162 (1957) 10

[10] J. Bardeen, L. N. Cooper and J. R. Schrieffer, Theory of Superconductivity, *Phys. Rev.* **108**, 1175 (1957) 10

[11] E. Maxwell, Isotope Effect in the Superconductivity of Mercury, *Phys. Rev.* **78**, 477 (1950) 10

[12] C. A. Reynolds, B. Serin, W. H. Wright and L. B. Nesbitt, Superconductivity of Isotopes of Mercury, *Phys. Rev.* **78**, 813 (1950) 10

[13] J. Pearl, Current distribution in superconducting films carrying quantized fluxoids, *Appl. Phys. Lett.* **5**, 65 (1964) 15

REFERENCES

[14] P. Ao and D. J. Thouless, Berry's phase and the Magnus force for a vortex line in a superconductor, *Phys. Rev. Lett.* **70**, 2158 (1993) 15

[15] C. P. Bean and J. D. Livingston, Surface Barrier in Type-II Superconductors, *Phys. Rev. Lett.* **12**, 14 (1964) 16

[16] G. Carneiro, Equilibrium vortex-line configurations and critical currents in thin films under a parallel field, *Phys. Rev. B* **57**, 6077 (1998) 16

[17] S. H. Brongersma, E. Verweij, N. J. Koeman, D. G. de Groot, R. Griessen et al., Series of maxima in the field dependent magnetic moment of layered superconductors, *Phys. Rev. Lett.* **71**, 2319 (1993) 16, 17

[18] Y.-L. Wang, A. Glatz, G. J. Kimmel, I. S. Aranson, L. R. Thoutam et al., Parallel magnetic field suppresses dissipation in superconducting nanostrips, *Proc Natl Acad Sci U S A* **114**, E10274 (2017) 16

[19] G. R. Berdiyorov, X. H. Chao, F. M. Peeters, H. B. Wang, V. V. Moshchalkov et al., Magnetoresistance oscillations in superconducting strips: A Ginzburg-Landau study, *Phys. Rev. B* **86**, 224504 (2012) 17, 20, 21, 22, 23, 26, 60, 69, 77, 118, 120, 128, 129

[20] S. A. Mills, J. J. Wisser, C. Shen, Z. Xu and Y. Liu, Vortex crossing, trapping, and pinning in superconducting nanowires of a NbSe2 two-dimensional crystal, *Phys. Rev. B* **93**, 224504 (2016) 22

[21] L. He and J. Wang, Periodic magnetoresistance oscillations induced by superconducting vortices in single crystal Au nanowires, *Nanotechnology* **22**, 445704 (2011) 22, 25

[22] D. Pekker, G. Refael and P. M. Goldbart, Weber Blockade Theory of Magnetoresistance Oscillations in Superconducting Strips, *Phys. Rev. Lett.* **107**, 017002 (2011) 23

[23] D. Zhang, J. Wang, A. M. DaSilva, J. S. Lee, H. R. Gutierrez et al., Superconducting proximity effect and possible evidence for Pearl vortices in a candidate topological insulator, *Phys. Rev. B* **84**, 165120 (2011) 23

[24] T. Morgan-Wall, B. Leith, N. Hartman, A. Rahman and N. Marković, Measurement of Critical Currents of Superconducting Aluminum Nanowires in External Magnetic Fields: Evidence for a Weber Blockade, *Phys. Rev. Lett.* **114**, 077002 (2015) 23

[25] B. S. Deaver and W. M. Fairbank, Experimental Evidence for Quantized Flux in Superconducting Cylinders, *Phys. Rev. Lett.* **7**, 43 (1961) 23

[26] R. Doll and M. Näbauer, Experimental Proof of Magnetic Flux Quantization in a Superconducting Ring, *Phys. Rev. Lett.* **7**, 51 (1961) 23

[27] W. A. Little and R. D. Parks, Observation of Quantum Periodicity in the Transition Temperature of a Superconducting Cylinder, *Phys. Rev. Lett.* **9**, 9 (1962) 23

[28] B. D. Josephson, Possible new effects in superconductive tunnelling, *Physics Letters* **1**, 251 (1962) 24

[29] B. D. Josephson, Supercurrents through barriers, *Advances in Physics* **14**, 419 (1965) 24

[30] A. V. Herzog, P. Xiong and R. C. Dynes, Magnetoresistance oscillations in granular Sn wires near the superconductor-insulator transition, *Phys. Rev. B* **58**, 14199 (1998) 25

[31] A. Johansson, G. Sambandamurthy, D. Shahar, N. Jacobson and R. Tenne, Nanowire Acting as a Superconducting Quantum Interference Device, *Phys. Rev. Lett.* **95**, 116805 (2005) 26

[32] U. Patel, Z. L. Xiao, A. Gurevich, S. Avci, J. Hua et al., Magnetoresistance oscillations in superconducting granular niobium nitride nanowires, *Phys. Rev. B* **80**, 012504 (2009) 25

[33] J. Wang, X. Ma, S. Ji, Y. Qi, Y. Fu et al., Magnetoresistance oscillations of ultrathin Pb bridges, *Nano Res.* **2**, 671 (2009) 70

[34] M. N. Kunchur, C. L. Dean and B. I. Ivlev, Anomalous oscillatory magnetoresistance in superconductors, *Phys. Rev. B* **94**, 054504 (2016) 25, 26

[35] T. F. Stromberg, *The Superconducting Properties of High Purity Niobium*, PhD Thesis, Iowa State University (1965) 26, 58

[36] L. P. He, Z. Zhang, J. Pan, X. C. Hong, S. Y. Zhou et al., Full superconducting gap in the doped topological crystalline insulator Sn0.6In0.4Te, *Phys. Rev. B* **88**, 014523 (2013) 26

[37] V. K. Maurya, Shruti, P. Srivastava and S. Patnaik, Superconducting properties of indium-doped topological crystalline insulator SnTe, *EPL* **108**, 37010 (2014) 26, 31

[38] D. Haviland, Superconducting circuits: Quantum phase slips, *Nat Phys* **6**, 565 (2010) 26

[39] K. von Klitzing, G. Dorda and M. Pepper, New Method for High-Accuracy Determination of the Fine-Structure Constant Based on Quantised Hall Resistance, *Phys. Rev. Lett.* **45**, 494 (1980) 27

[40] J. E. Avron, D. Osadchy and R. Seiler, A topological look at the Quantum Hall effect, *Physics Today* **56**, 38 (2003) 27

[41] B. A. Bernevig, T. L. Hughes and S.-C. Zhang, Quantum Spin Hall Effect and Topological Phase Transition in HgTe Quantum Wells, *Science* **314**, 1757 (2006) 27

[42] M. Konig, S. Wiedmann, C. Brune, A. Roth, H. Buhmann et al., Quantum spin hall insulator state in HgTe quantum wells, *Science* **318**, 766 (2007) 27

[43] L. Fu, C. L. Kane and E. J. Mele, Topological Insulators in Three Dimensions, *Phys. Rev. Lett.* **98**, 106803 (2007) 27

[44] L. Fu and C. L. Kane, Topological Insulators with Inversion Symmetry, *Physical Review B* **76** (2007) 27

REFERENCES

[45] R. Roy, Topological phases and the quantum spin Hall effect in three dimensions, *Phys. Rev. B* **79**, 195322 (2009)

[46] J. E. Moore and L. Balents, Topological invariants of time-reversal-invariant band structures, *Phys. Rev. B* **75**, 121306 (2007) 27

[47] D. Hsieh, D. Qian, L. Wray, Y. Xia, Y. S. Hor et al., A topological Dirac insulator in a quantum spin Hall phase, *Nature* **452**, 970 (2008) 27

[48] A. Damascelli, Probing the Electronic Structure of Complex Systems by ARPES, *Physica Scripta* **T109**, 61 (2004) 27

[49] M. Z. Hasan and C. L. Kane, Topological Insulators, *Reviews of Modern Physics* **82**, 3045 (2010) 28

[50] H. Peng, K. Lai, D. Kong, S. Meister, Y. Chen et al., Aharonov-Bohm interference in topological insulator nanoribbons, *Nat Mater* **9**, 225 (2010) 28

[51] F. Xiu, L. He, Y. Wang, L. Cheng, L.-T. Chang et al., Manipulating surface states in topological insulator nanoribbons, *Nat Nano* **6**, 216 (2011)

[52] M. Tian, W. Ning, Z. Qu, H. Du, J. Wang et al., Dual evidence of surface Dirac states in thin cylindrical topological insulator Bi2Te3 nanowires, *Scientific Reports* **3**, 1212 (2013)

[53] B. Hamdou, J. Gooth, A. Dorn, E. Pippel and K. Nielsch, Aharonov-Bohm oscillations and weak antilocalization in topological insulator Sb2Te3 nanowires, *Appl. Phys. Lett.* **102**, 223110 (2013) 29

[54] R. Du, H.-C. Hsu, A. C. Balram, Y. Yin, S. Dong et al., Robustness of topological surface states against strong disorder observed in Bi2Te3 nanotubes, *Phys. Rev. B* **93**, 195402 (2016) 28

[55] B. Bhattacharyya, A. Sharma, V. P. S. Awana, A. K. Srivastava, T. D. Senguttuvan et al., Observation of quantum oscillations in FIB fabricated nanowires of topological insulator Bi2Te3, *J. Phys.: Condens. Matter* **29**, 115602 (2017) 28

[56] M. Safdar, Q. Wang, M. Mirza, Z. Wang, K. Xu et al., Topological Surface Transport Properties of Single-Crystalline SnTe Nanowire, *Nano Lett.* **13**, 5344 (2013) 28, 32, 93, 104

[57] S. Hikami, A. I. Larkin and Y. Nagaoka, Spin-Orbit Interaction and Magnetoresistance in the Two Dimensional Random System, *Prog Theor Phys* **63**, 707 (1980) 29, 120, 130

[58] Y. Kawaguchi, H. Kitahara and S. Kawaji, Negative magnetoresistance in a two-dimensional impurity band in cesiated p-Si(111) surface inversion layers, *Surface Science* **73**, 520 (1978)

[59] Y. Kawaguchi and S. Kawaji, Negative Magnetoresistance in Silicon (100) MOS Inversion Layers, *J. Phys. Soc. Jpn.* **48**, 699 (1980) 29

[60] K. Nomura, M. Koshino and S. Ryu, Topological Delocalization of Two-Dimensional Massless Dirac Fermions, *Phys. Rev. Lett.* **99**, 146806 (2007) 29

[61] Z. Wang, L. Yang, X. Zhao, Z. Zhang and X. P. A. Gao, Linear magnetoresistance versus weak antilocalization effects in Bi2Te3, *Nano Res.* **8**, 2963 (2015) 29, 30

[62] H.-T. He, G. Wang, T. Zhang, I.-K. Sou, G. K. L. Wong et al., Impurity Effect on Weak Antilocalization in the Topological Insulator Bi2Te3, *Phys. Rev. Lett.* **106**, 166805 (2011) 29, 30

[63] B. A. Assaf, F. Katmis, P. Wei, B. Satpati, Z. Zhang et al., Quantum coherent transport in SnTe topological crystalline insulator thin films, *Appl. Phys. Lett.* **105**, 102108 (2014) 30

[64] M. Safdar, Q. Wang, Z. Wang, X. Zhan, K. Xu et al., Weak Antilocalization Effect of Topological Crystalline Insulator Pb1–xSnxTe Nanowires with Tunable Composition and Distinct {100} Facets, *Nano Lett.* **15**, 2485 (2015) 30

[65] L. Fu, Topological Crystalline Insulators, *Phys. Rev. Lett.* **106**, 106802 (2011) 30

[66] T. H. Hsieh, H. Lin, J. Liu, W. Duan, A. Bansil et al., Topological crystalline insulators in the SnTe material class, *Nat Commun* **3**, 982 (2012) 30, 31

[67] Y. Tanaka, Z. Ren, T. Sato, K. Nakayama, S. Souma et al., Experimental realization of a topological crystalline insulator in SnTe, *Nat Phys* **8**, 800 (2012) 30

[68] K. Dybko, M. Szot, A. Szczerbakow, M. U. Gutowska, T. Zajarniuk et al., Experimental evidence for topological surface states wrapping around a bulk SnTe crystal, *Phys. Rev. B* **96**, 205129 (2017) 30

[69] R. A. Hein and P. H. E. Meijer, Critical Magnetic Fields of Superconducting SnTe, *Phys. Rev.* **179**, 497 (1969) 31

[70] R. D. Zhong, J. A. Schneeloch, T. S. Liu, F. E. Camino, J. M. Tranquada et al., Superconductivity induced by In substitution into the topological crystalline insulator Pb0.5Sn0.5Te, *Phys. Rev. B* **90**, 020505 (2014) 31

[71] G. S. Bushmarina, I. A. Drabkin, D. V. Mashovets, R. V. Parfeniev, D. V. Shamshur et al., Superconducting properties of the SnTe-PbTe system doped with indium, *Physica B: Condensed Matter* **169**, 687 (1991) 31

[72] C. M. Polley, V. Jovic, T.-Y. Su, M. Saghir, D. Newby et al., Observation of surface states on heavily indium-doped SnTe(111), a superconducting topological crystalline insulator, *Phys. Rev. B* **93**, 075132 (2016) 31

[73] S. Sasaki, Z. Ren, A. A. Taskin, K. Segawa, L. Fu et al., Odd-Parity Pairing and Topological Superconductivity in a Strongly Spin-Orbit Coupled Semiconductor, *Phys. Rev. Lett.* **109**, 217004 (2012) 31, 34

REFERENCES

[74] S. Maeda, R. Hirose, K. Matano, M. Novak, Y. Ando et al., Spin-singlet superconductivity in the doped topological crystalline insulator Sn0.96In0.04Te, *Phys. Rev. B* **96**, 104502 (2017) 31

[75] M. Iizumi, Y. Hamaguchi, K. F. Komatsubara and Y. Kato, Phase Transition in SnTe with Low Carrier Concentration, *J. Phys. Soc. Jpn.* **38**, 443 (1975) 31

[76] Y. Ando and L. Fu, Topological Crystalline Insulators and Topological Superconductors: From Concepts to Materials, *Annu. Rev. Condens. Matter Phys.* **6**, 361 (2015) 31

[77] J. Shen, Y. Xie and J. J. Cha, Revealing Surface States in In-Doped SnTe Nanoplates with Low Bulk Mobility, *Nano Lett.* **15**, 3827 (2015) 32, 92, 121

[78] J. Shen, Y. Jung, A. S. Disa, F. J. Walker, C. H. Ahn et al., Synthesis of SnTe Nanoplates with {100} and {111} Surfaces, *Nano Lett.* **14**, 4183 (2014) 32, 41

[79] Z. Li, S. Shao, N. Li, K. McCall, J. Wang et al., Single Crystalline Nanostructures of Topological Crystalline Insulator SnTe with Distinct Facets and Morphologies, *Nano Lett.* **13**, 5443 (2013) 32, 93

[80] M. Safdar, Q. Wang, M. Mirza, Z. Wang and J. He, Crystal Shape Engineering of Topological Crystalline Insulator SnTe Microcrystals and Nanowires with Huge Thermal Activation Energy Gap, *Crystal Growth & Design* **14**, 2502 (2014) 32, 41, 93

[81] K. A. Dick, A review of nanowire growth promoted by alloys and non-alloying elements with emphasis on Au-assisted III–V nanowires, *Progress in Crystal Growth and Characterization of Materials* **54**, 138 (2008) 32

[82] H. J. Joyce, Q. Gao, H. H. Tan, C. Jagadish, Y. Kim et al., III-V semiconductor nanowires for optoelectronic device applications, *Prog. Quantum Electron.* **35**, 23 (2011) 32, 43

[83] K. A. Dick, K. Deppert, T. Mårtensson, B. Mandl, L. Samuelson et al., Failure of the Vapor-Liquid-Solid Mechanism in Au-Assisted MOVPE Growth of InAs Nanowires, *Nano Lett.* **5**, 761 (2005) 32

[84] S. Sasaki and Y. Ando, Superconducting Sn1-xInxTe Nanoplates, *Crystal Growth & Design* **15**, 2748 (2015) 32, 33, 41, 92

[85] S. Guo, A. F. Fidler, K. He, D. Su, G. Chen et al., Shape-Controlled Narrow-Gap SnTe Nanostructures: From Nanocubes to Nanorods and Nanowires, *J. Am. Chem. Soc.* **137**, 15074 (2015) 32

[86] P. Kumaravadivel, G. A. Pan, Y. Zhou, Y. Xie, P. Liu et al., Synthesis and superconductivity of In-doped SnTe nanostructures, *APL Materials* **5**, 076110 (2017) 32, 93

[87] X.-L. Qi and S.-C. Zhang, Topological insulators and superconductors, *Rev. Mod. Phys.* **83**, 1057 (2011) 33

[88] Y. Tsutsumi, T. Kawakami, K. Shiozaki, M. Sato and K. Machida, Symmetry-protected vortex bound state in superfluid He-3-B phase, *Phys. Rev. B* **91**, 144504 (2015) 33

[89] L. Fu and E. Berg, Odd-Parity Topological Superconductors: Theory and Application to CuxBi2Se3, *Phys. Rev. Lett.* **105**, 097001 (2010) 33

[90] M. Sato, Topological odd-parity superconductors, *Phys. Rev. B* **81**, 220504 (2010) 33

[91] K. Michaeli and L. Fu, Spin-Orbit Locking as a Protection Mechanism of the Odd-Parity Superconducting State against Disorder, *Phys. Rev. Lett.* **109**, 187003 (2012) 33

[92] T. Mizushima, Y. Tsutsumi, M. Sato and K. Machida, Symmetry protected topological superfluid 3 He-B, *J. Phys.: Condens. Matter* **27**, 113203 (2015) 33

[93] M. Sato, A. Yamakage and T. Mizushima, Mirror Majorana zero modes in spinful superconductors/superfluids Non-Abelian anyons in integer quantum vortices, *Physica E: Low-dimensional Systems and Nanostructures* **55**, 20 (2014) 33

[94] N. Read and D. Green, Paired states of fermions in two dimensions with breaking of parity and time-reversal symmetries and the fractional quantum Hall effect, *Phys. Rev. B* **61**, 10267 (2000) 33

[95] E. Majorana, A symmetric theory of electrons and positrons, *Nuovo Cimento* **14**, 171 (1937) 33

[96] F. Wilczek, Majorana returns, *Nat Phys* **5**, 614 (2009) 33

[97] R. Shindou, A. Furusaki and N. Nagaosa, Quantum impurity spin in Majorana edge fermions, *Phys. Rev. B* **82**, 180505 (2010) 33

[98] M. Sato and S. Fujimoto, Majorana Fermions and Topology in Superconductors, *Journal of the Physical Society of Japan* **85**, 072001 (2016) 34

[99] S. Nadj-Perge, I. K. Drozdov, J. Li, H. Chen, S. Jeon et al., Observation of Majorana fermions in ferromagnetic atomic chains on a superconductor, *Science* **346**, 602 (2014) 34

[100] L. Fu and C. L. Kane, Josephson current and noise at a superconductor/quantum-spin-Hall-insulator/superconductor junction, *Phys. Rev. B* **79**, 161408 (2009) 34

[101] E. Mellars and B. Béri, Signatures of time-reversal-invariant topological superconductivity in the Josephson effect, *Phys. Rev. B* **94**, 174508 (2016) 34

[102] B. Sacépé, J. B. Oostinga, J. Li, A. Ubaldini, N. J. G. Couto et al., Gate-tuned normal and superconducting transport at the surface of a topological insulator, *Nature Communications* **2**, ncomms1586 (2011) 35

[103] L. Maier, J. B. Oostinga, D. Knott, C. Brüne, P. Virtanen et al., Induced Superconductivity in the Three-Dimensional Topological Insulator HgTe, *Phys. Rev. Lett.* **109**, 186806 (2012)

REFERENCES

[104] F. Qu, F. Yang, J. Shen, Y. Ding, J. Chen et al., Strong Superconducting Proximity Effect in Pb-Bi2Te3 Hybrid Structures, *Sci Rep* **2** (2012)

[105] M. Veldhorst, M. Snelder, M. Hoek, T. Gang, X. L. Wang et al., Josephson supercurrent through a topological insulator surface state, *Nature Materials* **11**, 417 (2012)

[106] J. R. Williams, A. J. Bestwick, P. Gallagher, S. S. Hong, Y. Cui et al., Unconventional Josephson Effect in Hybrid Superconductor-Topological Insulator Devices, *Phys. Rev. Lett.* **109**, 056803 (2012)

[107] S. Cho, B. Dellabetta, A. Yang, J. Schneeloch, Z. Xu et al., Symmetry protected Josephson supercurrents in three-dimensional topological insulators, *Nature Communications* **4**, ncomms2701 (2013)

[108] J. B. Oostinga, L. Maier, P. Schüffelgen, D. Knott, C. Ames et al., Josephson Supercurrent through the Topological Surface States of Strained Bulk HgTe, *Phys. Rev. X* **3**, 021007 (2013)

[109] I. Sochnikov, A. J. Bestwick, J. R. Williams, T. M. Lippman, I. R. Fisher et al., Direct Measurement of Current-Phase Relations in Superconductor/Topological Insulator/Superconductor Junctions, *Nano Lett.* **13**, 3086 (2013)

[110] L. Galletti, S. Charpentier, M. Iavarone, P. Lucignano, D. Massarotti et al., Influence of topological edge states on the properties of Al/Bi2Se3/Al hybrid Josephson devices, *Phys. Rev. B* **89**, 134512 (2014)

[111] M. Snelder, C. G. Molenaar, Y. Pan, D. Wu, Y. K. Huang et al., Josephson supercurrent in a topological insulator without a bulk shunt, *Superconductor Science and Technology* **27**, 104001 (2014)

[112] V. Orlyanchik, M. P. Stehno, C. D. Nugroho, P. Ghaemi, M. Brahlek et al., Signature of a topological phase transition in the Josephson supercurrent through a topological insulator, *Physical Review B* **93** (2016)

[113] L. A. Jauregui, M. Kayyalha, A. Kazakov, I. Miotkowski, L. P. Rokhinson et al., Gate-tunable supercurrent and multiple Andreev reflections in a superconductor-topological insulator nanoribbon-superconductor hybrid device, *Appl. Phys. Lett.* **112**, 093105 (2018) 35

[114] R. Klett, J. Schönle, A. Becker, D. Dyck, K. Borisov et al., Proximity-Induced Superconductivity and Quantum Interference in Topological Crystalline Insulator SnTe Thin-Film Devices, *Nano Lett.* **18**, 1264 (2018) 35

[115] J. Wiedenmann, E. Bocquillon, R. S. Deacon, S. Hartinger, O. Herrmann et al., 4π-periodic Josephson supercurrent in HgTe-based topological Josephson junctions, *Nature Communications* **7**, 10303 (2016) 35

[116] W. Yu, W. Pan, D. L. Medlin, M. A. Rodriguez, S. R. Lee et al., π and 4π Josephson Effects Mediated by a Dirac Semimetal, *Phys. Rev. Lett.* **120**, 177704 (2018) 35

[117] C. Li, J. C. de Boer, B. de Ronde, S. V. Ramankutty, E. van Heumen et al., 4π or π-periodic Andreev bound states in a Dirac semimetal, *Nature Materials* **17**, 875 (2018)

[118] A.-Q. Wang, C.-Z. Li, C. Li, Z.-M. Liao, A. Brinkman et al., 4π-Periodic Supercurrent from Surface States in Cd3As2 Nanowire-Based Josephson Junctions, *Phys. Rev. Lett.* **121**, 237701 (2018) 35

[119] A. Yamakage, M. Sato, K. Yada, S. Kashiwaya and Y. Tanaka, Anomalous Josephson current in superconducting topological insulator, *Physical Review B* **87** (2013) 35

[120] N. V. Gnezdilov, M. Diez, M. J. Pacholski and C. W. J. Beenakker, Wiedemann-Franz-type relation between shot noise and thermal conduction of Majorana surface states in a three-dimensional topological superconductor, *Phys. Rev. B* **94**, 115415 (2016) 35

[121] P. J. Kelly and R. D. Arnell, Magnetron sputtering: A review of recent developments and applications, *Vacuum* **56**, 159 (2000) 39

[122] M. Saghir, M. R. Lees, S. J. York and G. Balakrishnan, Synthesis and Characterization of Nanomaterials of the Topological Crystalline Insulator SnTe, *Crystal Growth & Design* **14**, 2009 (2014) 41

[123] R. Colin and J. Drowart, Thermodynamic study of tin selenide and tin telluride using a mass spectrometer, *Trans. Faraday Soc.* **60**, 673 (1964) 42, 102

[124] R. E. Honig and D. A. Kramer, *Vapor Pressure Data for the Solid and Liquid Elements*, RCA Laboratories, David Sarnoff Research Center (1969) 42, 102

[125] J. H. Woodruff, J. B. Ratchford, I. A. Goldthorpe, P. C. McIntyre and Chidsey, Vertically Oriented Germanium Nanowires Grown from Gold Colloids on Silicon Substrates and Subsequent Gold Removal, *Nano Lett.* **7**, 1637 (2007) 43

[126] O. Madelung, U. Rössler and M. Schulz, Tin telluride (SnTe) crystal structure, lattice parameters, in *Non-Tetrahedrally Bonded Elements and Binary Compounds I*, Springer Berlin Heidelberg, Berlin, Heidelberg, Landolt-Börnstein - Group III Condensed Matter, pp. 1–8 (1998) 47

[127] J. T. Batley, *Spin Transport in Lateral Spin Valves*, PhD Thesis, University of Leeds (2015) 50

[128] K. Fuchs, The conductivity of thin metallic films according to the electron theory of metals, *Mathematical Proceedings of the Cambridge Philosophical Society* **34**, 100 (1938) 58

[129] E. H. Sondheimer, The mean free path of electrons in metals, *Advances in Physics* **1**, 1 (1952) 58

[130] L. R. Testardi and L. F. Mattheiss, Electron Lifetime Effects on Properties of A15 and bcc Materials, *Phys. Rev. Lett.* **41**, 1612 (1978) 58

REFERENCES

[131] N. R. Werthamer, E. Helfand and P. C. Hohenberg, Temperature and Purity Dependence of the Superconducting Critical Field, Hc2. III. Electron Spin and Spin-Orbit Effects, *Phys. Rev.* **147**, 295 (1966) 58

[132] K. Maki, Effect of Pauli Paramagnetism on Magnetic Properties of High-Field Superconductors, *Phys. Rev.* **148**, 362 (1966) 58

[133] A. F. Mayadas, R. B. Laibowitz and J. J. Cuomo, Electrical Characteristics of rf-Sputtered Single-Crystal Niobium Films, *Journal of Applied Physics* **43**, 1287 (1972) 59

[134] T. R. Lemberger, I. Hetel, J. W. Knepper and F. Y. Yang, Penetration depth study of very thin superconducting Nb films, *Phys. Rev. B* **76**, 094515 (2007) 59

[135] S. I. Park and T. H. Geballe, Superconducting Tunneling in Ultrathin Nb Films, *Phys. Rev. Lett.* **57**, 901 (1986)

[136] A. I. Gubin, K. S. Il'in, S. A. Vitusevich, M. Siegel and N. Klein, Dependence of magnetic penetration depth on the thickness of superconducting Nb thin films, *Phys. Rev. B* **72**, 064503 (2005) 59

[137] N. Pompeo, E. Silva, S. Sarti, C. Attanasio and C. Cirillo, New aspects of microwave properties of Nb in the mixed state, *Physica C: Superconductivity* **470**, 901 (2010) 69, 129

[138] J. I. Gittleman and B. Rosenblum, Radio-Frequency Resistance in the Mixed State for Subcritical Currents, *Phys. Rev. Lett.* **16**, 734 (1966) 69

[139] S. Okuma, S. Morishima and M. Kamada, Dynamic transition and metastability in the nonlinear I-V regime in a Corbino disk superconductor, *Phys. Rev. B* **76**, 224521 (2007) 69, 129

[140] G. R. Berdiyorov, M. V. Milošević, M. L. Latimer, Z. L. Xiao, W. K. Kwok et al., Large Magnetoresistance Oscillations in Mesoscopic Superconductors due to Current-Excited Moving Vortices, *Phys. Rev. Lett.* **109**, 057004 (2012) 70

[141] A. R. de C. Romaguera, M. M. Doria and F. M. Peters, Tilted vortices in a superconducting mesoscopic cylinder, *Phys. Rev. B* **75**, 184525 (2007) 71, 73, 75

[142] S. J. Hagen, C. J. Lobb, R. L. Greene, M. G. Forrester and J. H. Kang, Anomalous Hall effect in superconductors near their critical temperatures, *Phys. Rev. B* **41**, 11630 (1990) 78

[143] H. E. Hall, W. F. Vinen and D. Shoenberg, The rotation of liquid helium II II. The theory of mutual friction in uniformly rotating helium II, *Proceedings of the Royal Society of London. Series A. Mathematical and Physical Sciences* **238**, 215 (1956) 78

[144] V. Ambegaokar, B. I. Halperin, D. R. Nelson and E. D. Siggia, Dynamics of superfluid films, *Phys. Rev. B* **21**, 1806 (1980) 78

[145] P. Ao, Motion of vacancies in a pinned vortex lattice: Origin of the Hall anomaly, *J. Phys.: Condens. Matter* **10**, L677 (1998) 78

[146] L. Ghenim, J.-Y. Fortin, G. Wen, X. Zhang, C. Baraduc et al., Transport and vortex pinning in micron-size superconducting Nb films, *Phys. Rev. B* **69**, 064513 (2004) 78

[147] P. Liu, J. R. Williams and J. J. Cha, Topological nanomaterials, *Nature Reviews Materials* **4**, 479 (2019) 92

[148] G. Balakrishnan, L. Bawden, S. Cavendish and M. R. Lees, Superconducting properties of the In substituted Topological Crystalline Insulator, SnTe, *Physical Review B* **87** (2013) 102

[149] R. D. Zhong, J. A. Schneeloch, X. Y. Shi, Z. J. Xu, C. Zhang et al., Optimizing the superconducting transition temperature and upper critical field of Sn1-xInxTe, *Phys. Rev. B* **88**, 020505 (2013) 102, 103

[150] C. Zhang, X.-G. He, H. Chi, R. Zhong, W. Ku et al., Electron and hole contributions to normal-state transport in the superconducting system Sn1-xInxTe, *Phys. Rev. B* **98**, 054503 (2018) 104

[151] B. L. Altshuler, A. G. Aronov and D. E. Khmelnitsky, Effects of electron-electron collisions with small energy transfers on quantum localisation, *J. Phys. C: Solid State Phys.* **15**, 7367 (1982) 125

[152] C.-Y. Wu, B.-T. Lin, Y.-J. Zhang, Z.-Q. Li and J.-J. Lin, Electron dephasing in homogeneous and inhomogeneous indium tin oxide thin films, *Phys. Rev. B* **85**, 104204 (2012)

[153] Y. Takagaki, A. Giussani, K. Perumal, R. Calarco and K.-J. Friedland, Robust topological surface states in Sb2Te3 layers as seen from the weak antilocalization effect, *Phys. Rev. B* **86**, 125137 (2012)

[154] D. Backes, D. Huang, R. Mansell, M. Lanius, J. Kampmeier et al., Disentangling surface and bulk transport in topological-insulator p-n junctions, *Phys. Rev. B* **96**, 125125 (2017) 125